UNIVERSITY OF THE WESTERN CAPE

Triaxiality and Rotational Bands in ^{133}Ce

by

Ignasio Wakudyanaye
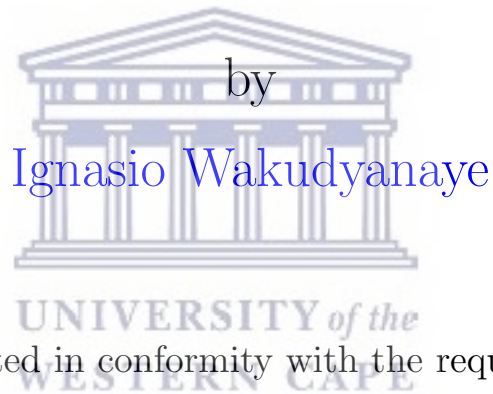
A thesis submitted in conformity with the requirements for the
degree of Magister Scientiae

in the

Faculty of Science

Department of Physics and Astronomy

Supervisor: Dr. Elena A. Lawrie (iThemba LABS)
Co-Supervisor: Prof José N. Orce (UWC)

March 2022

Declaration

I, Ignasio Wakudyanaye, declare that this thesis " Triaxiality and Rotational Bands in ^{133}Ce" is my own work, that it has not been submitted before for any degree or assessment at any other university, and that all the sources I have used or quoted have been indicated and acknowledged by means of complete references.
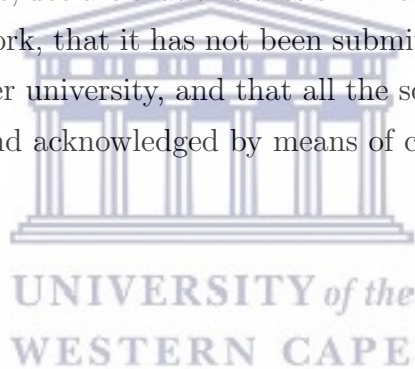
Signature: . . . .   Date: . . . .

"Physics is like sex: sure, it may give some practical results, but that's not why we do it. "

Richard P. Feynman

Abstract

The neutron-deficient nuclei between the $N = 50$ and $N = 82$ shell closures provide rich information on the shape and structure of the nucleus. The isotones of ^{133}Ce and ^{131}Ba ($N = 75$) lie in this region of the nuclear chart. The properties of two recently discovered positive-parity rotational bands based on the $g_{7/2}$ orbital were studied in this work. The rotational bands in both nuclei are based on the $7/2^+$ state. The quasiparticle+triaxial rotor (QTR) model was used to understand the dependence of the excitation energies and the signature splitting in these bands as a function of triaxiality. In addition to triaxiality, the effects of the Coriolis interaction on the excitation energies and the signature splitting was also investigated.

A new negative-parity band was also identified in the ^{133}Ce nuclei. It is built on the $I = 13/2^-$ state. Thirteen new intraband transitions and fifteen new interband transitions linking this exited band to the yrast band are identified in this work. A triaxial one-quasiparticle $\nu(h_{11/2})^{-1}[514]9/2^-$ configuration, with a triaxiality of $\sim 20°$ is proposed for the structure. These new experimental results are compared with two sets of QTR model calculations, (i) with a configuration space of nine negative-parity orbitals close to the Fermi level, which corresponds to a description as a $3D$ tilted precession of the nucleus and (ii) with a configuration space of one negative-parity orbital (the frozen alignment approximation used previously to describe wobbling). The QTR with a configuration space of nine negative-parity orbitals close to the Fermi level describes the experimentally observed band properties better than the frozen alignment case.

Keywords

Acknowledgements

First and foremost, I thank myself, for coming so far!

I would like to thank my family for giving me their unwavering support to further my education. Under their guidance and support, I had come so far up to this point. Further still, I have to go.

I would especially like to express my eternal gratitude to my supervisor Dr Elena Lawrie for her outstanding guidance, inspiration and motivation. Thank you for being so understanding and patient with me. I would also like to thank my co-supervisor Prof José Nicolás Orce for his support and guidance during my studies.

I would also like to thank my co-workers from the nuclear structure group at iThemba LABS and the Nuclear Warriors group from UWC. To the department of physics and astronomy at the University of the Western Cape, iThemba LABS, and the National Research Foundation (NRF) of South Africa, I extend my gratitude for providing financial assistance for my studies through the MANuS/MatSci program.

Indeed, the list of people that have helped me to this point is long, and I'm very lucky and grateful for that! To everyone else who has been part of my journey so far, THANK YOU SO MUCH! especially Prof Robert Lindsay.

Contents

UNIVERSITY *of the*
WESTERN CAPE

List of Figures

List of Tables

Chapter 1

Introduction

1.1 Introduction

When an atomic nucleus is excited without changing its internal configuration, it emits γ rays (high-energy photons) to release the excess energy in the system and to reach the ground state (a state with minimum energy). This quantum mechanical process happens in accordance with various physical laws. There are two types of excitations that a nucleus can undergo, (i) single-particle excitations, which generate irregular sequences of γ-ray transitions and (ii) collective excitations, which involve all nucleons in the system behaving coherently, and produce regular sequences of γ-ray transitions. Collective excitations include vibrational and rotational motions.

Nuclear vibrational motion was considered as a common de-excitation mechanism employed by spherical nuclei as they cannot rotate, however this has recently been questioned (see Ref. [24]). Most nuclei that exist in nature are not spherical, but rather have deformed shapes in their ground states. Deformed nuclei prefer rotational motion as this is a lower-energy excitation mode than vibration, although deformed nuclei can vibrate too. The axially deformed nuclear shape is the simplest deformed nuclear shape, which is a spheroid shape (like an egg or a pancake).

In addition to axially deformed nuclear shapes, it is also possible to have non-axially deformed nuclei. These nuclei are known as triaxially deformed nuclei. Nuclear triaxiality has been observed in the $A = 80$, $A = 100$, $A = 130$ and

1

$A = 190$ mass regions. In addition to rotations and vibrations, triaxial nuclei can access other modes of excitations including wobbling motion and chirality. Therefore, these regions present an exciting opportunity to test nuclear structure theories across the nuclear chart.

Gamma spectroscopy involves the study of the γ rays emitted by nuclei as they de-excite. It provides important information such as the spins and parities of nuclear states and the energy of γ-ray transitions which can be compared with our theories of nuclear processes. Detailed spectroscopy was done in the $N = 75$ isotones (nuclei with the same number of neutrons) of ^{133}Ce and ^{131}Ba within a collaboration consisting of researchers from South Africa, China and France. The ^{133}Ce experiment was conducted at the separated sector cyclotron of iThemba LABS in Cape Town, South Africa, while the ^{131}Ba experiment was carried out at the XTU Tandem accelerator of Laborotori Nazionali di Legnaro, Italy. The data sets that were collected and analyzed revealed one new positive-parity band based on the $g_{7/2}$ neutron orbital with a projection of 7/2 on the long axis in both ^{133}Ce and ^{131}Ba nuclei. In ^{133}Ce a new strongly coupled negative-parity band based on the $h_{11/2}$ neutron orbital with a projection of 9/2 on the long axis was also discovered.

In this work, γ-γ coincidences from the ^{133}Ce data were studied. On the basis of this analysis a partial level scheme of ^{133}Ce was constructed and two new rotational bands were discovered. The spins and parity assignments for the newly discovered bands in ^{133}Ce, as well as the data analysis for the $g_{7/2}$ band in ^{131}Ba was done by our collaborators. Quasiparticle-plus-triaxial rotor (QTR) model calculations were performed as part of this work. The interpretation of the new $g_{7/2}$ bands observed in ^{133}Ce and ^{131}Ba were based on these calculations. The results were recently published in Physical Review C [22]. The results on the $h_{11/2}$ bands of ^{133}Ce are in preparation for publication.

The remainder of the thesis is arranged as follows:

Chapter 2: *Theoretical Framework*: A general overview of the basics of nuclear physics is discussed. Emphasis is placed on nuclear deformations and the Nilsson model which is especially relevant for the understanding of single-particle degrees of freedom in nuclear rotational motion of the axially deformed nuclei.

Chapter 3: *Nuclear Triaxiality*: Rotations of the non-axially deformed nuclear shape is considered. Two models of studying nuclear triaxiality are considered; (i)

Tilted Precession (TiP) and, (ii) Nuclear Wobbling motion. They are discussed together with their respective model predictions.

Chapter 4: *Experimental Techniques*: Some experimental techniques used to produce and study nuclei with high spins are discussed.

Chapter 5: *Results*: The results of two experiments for ^{133}Ce and ^{131}Ba are presented. The first experiment was conducted at the NRF iThemba LABS in Cape Town. In this experiment two new excited band structures are observed. The first band is a positive-parity band built on the $I^{\pi} = 7/2^+$ state. The second band is a negative-parity structure built on a $I = 13/2^-$ state.

A second experiment was conducted at the Laborotori Nazionali di Legnaro in Italy. In this experiment a new band structure was discovered. It is built on the $I = 7/2^+$ state.

Chapter 6: *Discussion*: The results presented in Chapter 5 are interpreted using the QTR model. The two positive-parity structures in the $Z = 75$ isotones, ^{133}Ce and ^{131}Ba are assigned an approximate $\nu g_{7/2}[404]7/2^+$ Nilsson configuration based on the observed band properties. The bands exhibit signature splitting and the QTR model is used to investigate the influence of triaxiality and the Coriolis interaction on the experimentally observed signature splitting.

The quasiparticle-plus-triaxial rotor (QTR) model was used to investigate the yrast and the excited negative-parity bands in ^{133}Ce associated with a a neutron $h_{11/2}$ configuration. Alternative interpretations, in terms of TiP bands and as transverse wobbling bands were considered. The observed band properties including the excitation energy and the signature splitting support an interpretation of the observed bands as TiP bands. Further evidence from the experimentally observed electromagnetic transition properties support this interpretation.

Chapter 7: *Conclusion*: The work done for the $g_{7/2}$ bands in ^{133}Ce and ^{131}Ba and the work done for the $h_{11/2}$ bands in ^{133}Ce is summarized.

Chapter 2

Theoretical Framework

2.1 Introduction

The nucleus is a quantal system, at all times its behaviour is completely determined by the eigenstate Ψ, that solves the time-independent Schrödinger equation:
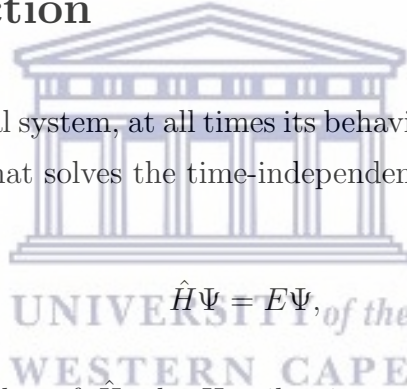
$$\hat{H}\Psi = E\Psi, \tag{2.1}$$

where E is an eigenvalue of $\hat{H}$, the Hamiltonian operator of the system and is defined as the sum of the kinetic and potential energy operators, $\hat{T}$ and $\hat{V}$ respectively, that is:

$$\hat{H} = \hat{T} + \hat{V} = \sum_{i=1}^{A} \frac{\hat{p}_i^2}{2m_i} + \sum_{i \neq j}^{A} V(\vec{r}_{i,j}). \tag{2.2}$$

Here, $\hat{p} = -i\hbar\triangledown$ is the momentum operator, $\hbar$ is the reduced Plank's constant, A is the number of nucleons in the system, m is the nucleon mass and $V(\vec{r}_{i,j})$ is the nucleon-nucleon interaction as a function of the ith and j^{th} nucleons co-ordinates.

Due to the fundamental elusiveness of the true nature of the nuclear potential that governs the interaction of nucleons inside atomic nuclei, nuclear models are employed to understand observables from nuclear experiments.

2.2   Nuclear Potentials and The Shell Model

In the 20th century, experimental evidence showed the existence of magic numbers for protons and neutrons in atomic nuclei. These nuclei were more tightly bound when compared to their immediately neighboring nuclei and they required significantly more energy to remove a nucleon from the nucleus. This indicated shell closures and led early nuclear physicists to postulate the existence of shell structures inside atomic nuclei, in direct analogy to the electronic shell structures observed in atomic physics. The magic numbers for protons and neutrons are:

$$Z, N = 2, 8, 20, 28, 50, 82, (126). \qquad (2.3)$$

The last magic number belongs to neutrons alone. To account for these "magic" numbers the shell model was devised. The shell model approach assumes that each nucleon inside an atomic nucleus is independent and moves in a mean-field central potential that is generated by the other $(A - 1)$ nucleons. This ingenious idea transforms our original intractable A-body problem (equation 2.2) into independent single-particle motion. This leads to A single-particle states and their related energy spectrum. Now the question arises–what is the appropriate mean-field central potential?

A mean central potential of $v(\vec{r}_i)$, which depends only on the coordinates of the ith nucleon can be added and subtracted in equation 2.2. This splits the Hamiltonian into a non-interacting part $\hat{H}_0$ and a residual interaction, W_{Res}, (which accounts for the two-body interactions between the nucleons). The Hamiltonian of the system can be written down as:

$$\hat{H} = [\sum_{i=1}^{A} \frac{\hat{p}_i^2}{2m_i} + v(\vec{r}_i)] + [\sum_{i \neq j}^{A} V(\vec{r}_{i,j}) - v(\vec{r}_i)]$$
$$= \hat{H}_0 + W_{Res}. \qquad (2.4)$$

For the non-interacting shell model, $W_{Res} = 0$. A first-order approximation to the central nuclear potential is the spherically symmetric infinite square well, that is $v(\vec{r}_i) \to v(r_i)$ (see also Figure 2.1):
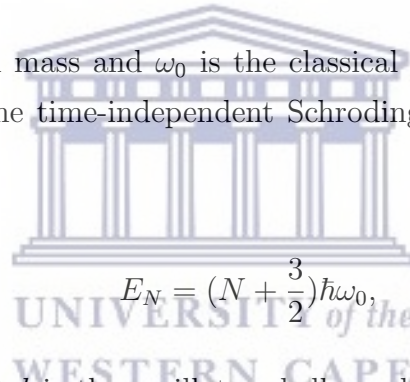
$$v(r) = \begin{cases} -V_0, \text{ if } r \leq R \\ \infty, \text{ if } r > R \end{cases} \tag{2.5}$$

This potential is able to reproduce the first three magic numbers, (2, 8 and 20), see panel (a) of Figure 2.2. Each level can be occupied by a specific number of protons and neutrons, each nucleon type occupies its own potential well in accordance with the Pauli exclusion principle.

As a second approximation, the harmonic oscillator potential (Figure 2.1) is used [61]:

$$v(r_i) = \frac{1}{2}(M\omega_0^2 r_i^2). \tag{2.6}$$

Here M is the nucleon mass and ω_0 is the classical oscillator frequency. Solving for this potential in the time-independent Schrodinger equation (2.1) yields the energy levels:

$$E_N = (N + \frac{3}{2})\hbar\omega_0, \tag{2.7}$$

where $N = 2(n - 1) + l$ is the oscillator shell number, N is defined in terms of the radial quantum number, $n = 1, 2, 3, ...$, and the orbital angular momentum quantum number, $l = 0, 1, 2, 3, ..., (n - 1)$. The oscillator shell number N, assumes the values of $N = 0, 1, 2, 3, ...$ Each N shell has a degenerate group of levels with different l. The selection rule on l is that l is even (odd) when N is even (odd). This potential is able to reproduce the first three magic numbers, see panel (b) of Figure 2.2.

Both the harmonic oscillator (H.O.) and the infinite-square well potentials have the disadvantage that they require an infinite amount of energy to remove a nucleon from a nucleus, because both potentials tend to infinity as r tends to infinity. The W-S potential (see Figure 2.1) is a more realistic nuclear potential:

$$V(r_i) = \frac{-V_0}{1 + \exp[(r_i - R)/a]}, \tag{2.8}$$
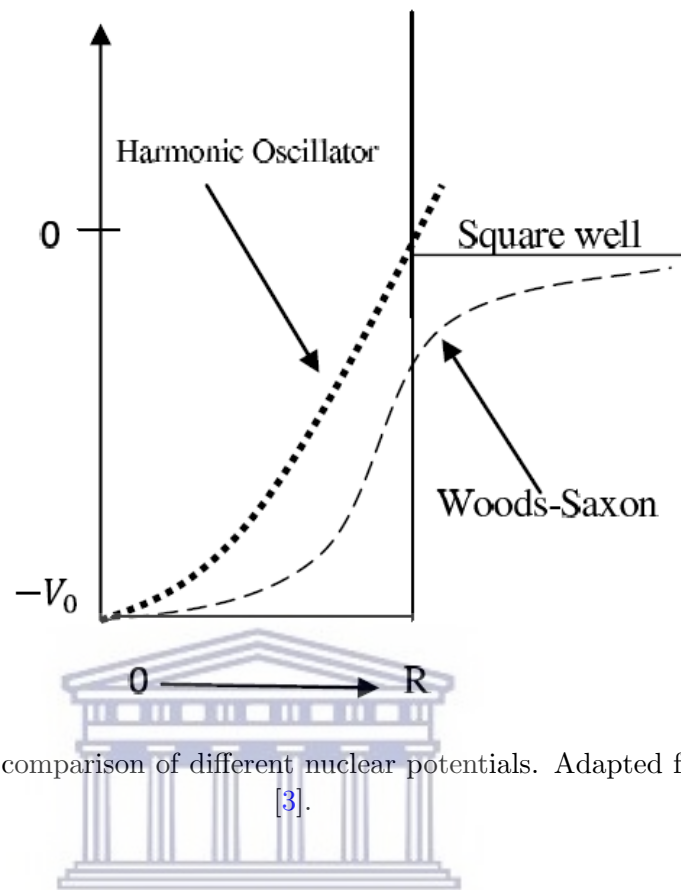
FIGURE 2.1: A comparison of different nuclear potentials. Adapted from Ref.
[3].

where V_0 is the depth of the well, $R = 1.25A^{\frac{1}{3}}$ fm, is the mean nuclear radius
and $a = 0.524$ fm is the skin thickness of the nucleus. This potential has the
flat-bottom characteristic of the square-well potential and the parabolic rise of the
H.O. potential, and it can reproduce the first three magic numbers, see panel (c)
of Figure 2.2.

The addition of a term proportional to l^2 in the harmonic oscillator potential
(equation 2.6) has the effect of interpolating between the square-well and the
H.O. potentials and becomes similar to the W-S potential. With the addition of a
spin-orbit term to either the W-S potential or to the H.O. with l^2 term, the magic
numbers can be successfully reproduced [32, 50]. The Schrodinger equation with
the W-S potential can only be solved numerically. The harmonic oscillator with
l^2 term does admit analytical solutions.

2.2.1   The Spin-Orbit Term

As previously stated, spin-orbit coupling is necessary to reproduce the correct magic numbers [32, 50]. The orbital angular momentum $\vec{l}$ and the intrinsic angular momentum (spin, $\vec{s}$) are coupled to give the total angular momentum of the $\vec{j} = \vec{l} + \vec{s}$. The spin-orbit term has the form:

$$V_{SO} = f_{so}(r)\vec{l} \cdot \vec{s}, \tag{2.9}$$

where $f_{so}(r)$ is the strength of the interaction. This interaction splits the degenerate energy levels into two components with $j = l \pm \frac{1}{2}$. The $j = l + \frac{1}{2}$ lies lower in energy than the $j = l - \frac{1}{2}$ component. Each state of a given j can be filled by a maximum of $2j + 1$ nucleons as shown in panel (d) of Figure 2.2.

With the inclusion of the above modifications, the W-S potential can be written down as:

$$V(r) = \frac{-V_0}{1 + \exp[(r - R)/a]} + f_{(so)}(r)\vec{l} \cdot \vec{s}, \tag{2.10}$$

and the harmonic oscillator potential becomes:

$$v(r) = \frac{1}{2}M\omega_0^2 r^2 + Cl^2 + Df_{so}(r)\vec{l} \cdot \vec{s}, \tag{2.11}$$

where C and D are proportionality constants and are fitted to reproduce the spherical shell model. The Coulomb potential $V_c \propto e(Z - 1)$ has been omitted in the preceding discussion because it only has the effect of reducing the binding energy of the system by making the proton well shallower and does not change the sequence of the magic numbers. It can easily be treated by including it in the potentials of equations 2.10 and 2.11 when the nucleons are protons.

In Figure 2.2 each single particle state is labelled by the major shell number N, followed by the angular momentum quantum number l. In spectroscopic notation, $l = 0$ is labelled by s; $l = 1$ is labelled by p; $l = 2$ is labelled by d; $l = 3$ is labelled by f, thereafter the labels follow the alphabet. The parity of the levels is given by $\pi = (-1)^l$. The shell model is very successful in predicting the ground-state properties of most nuclei that are close to magic numbers [36].
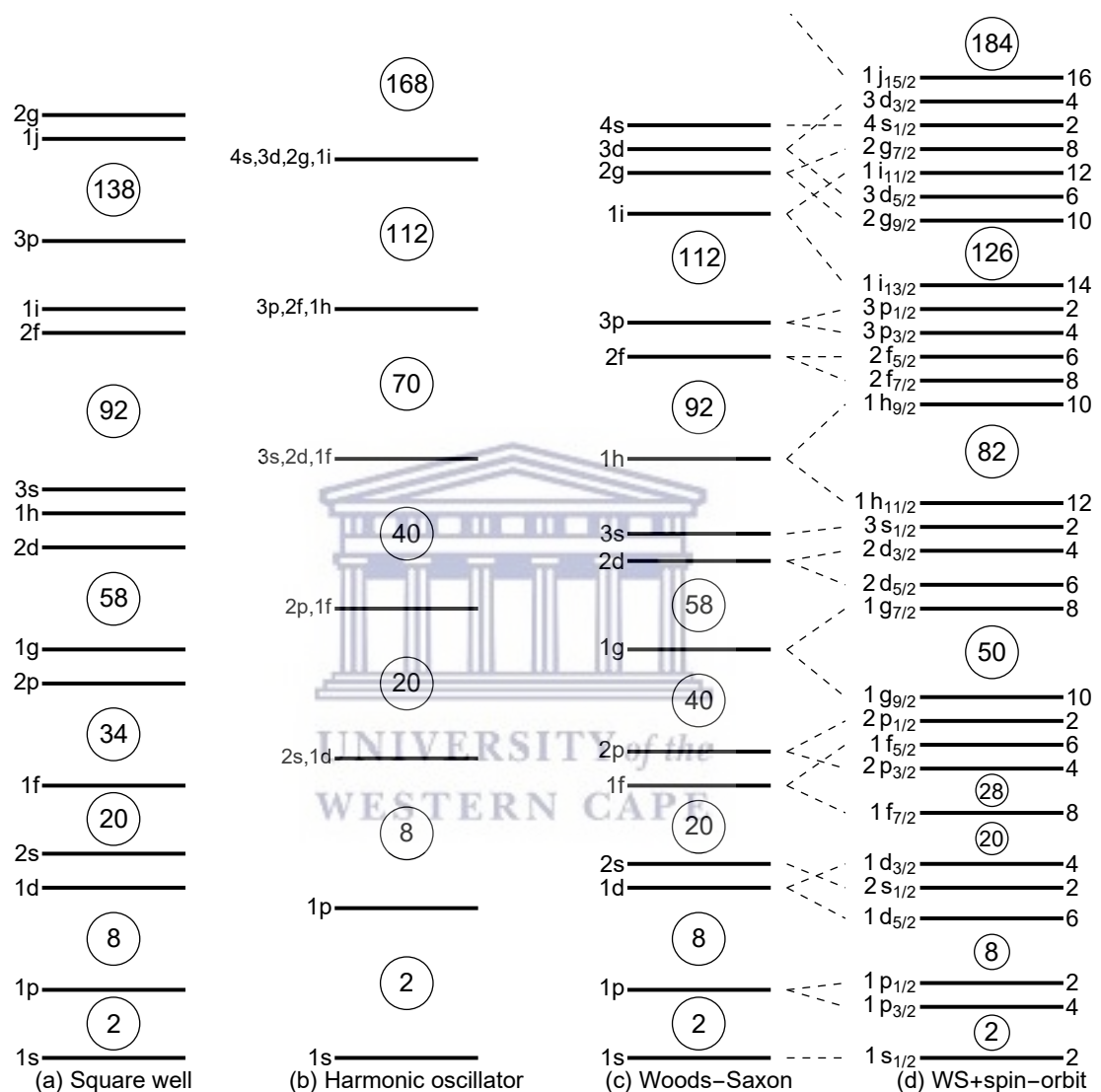
FIGURE 2.2: Nuclear shell structure predicted by (a) infinite square well potential, (b) harmonic oscillator potential, (c) Woods-Saxon potential, and (d) W-S potential with spin-orbit. The circled numbers represent magic numbers, while the numbers on the right in panel (d) represent the occupation numbers for those particular levels. Adapted from Krane [12, 36].

2.3 Nuclear Deformations

With the exception of nuclei at or near closed shells, most nuclei that exist in nature are deformed in their ground states, that is most are not spherical [15]. The experimental evidence for this includes (i) the existence of rotational bands, and (ii) the large measured quadrupole moments. The nuclear surface deformations can be parameterized by an infinite series expansion in spherical harmonics as:

$$R(\theta, \phi) = R_0[1 + \sum_{\lambda=0}^{\infty} \sum_{\mu=-\lambda}^{\lambda} \alpha_{\lambda\mu} Y_\lambda^\mu(\theta, \phi)]. \qquad (2.12)$$

Here $R(\theta, \phi)$ is the length of a radius vector from the origin to a point on the nuclear surface, R_0 is the length of the radius vector of a sphere having the same volume as the nucleus, $Y(\theta, \phi)$ are the spherical harmonics, $\alpha_{\lambda\mu}$ are the expansion coefficients and λ is the multipole order of the expansion.

In equation 2.12, $\lambda = 2$ corresponds to a static quadrupole deformation of the nucleus. In a coordinate frame that coincides with the nuclear axes the five expansion coefficients ($\alpha_{2\mu}$) reduce to two independent coefficients α_{20} and α_{22} due to the reflection symmetry of the quadruple shape; $\alpha_{21} = \alpha_{2-1} = 0$ and $\alpha_{22} = \alpha_{2-2}$. These expansion coefficients can be related to the deformation parameters β_2 and γ by the relations:

$$\alpha_{20} = \beta_2 \cos \gamma, \qquad (2.13)$$

and

$$\alpha_{22} = \frac{1}{\sqrt{2}} \beta_2 \sin \gamma. \qquad (2.14)$$

Now the nuclear shape is parameterized only in terms of the quadrupole deformation β_2, which measures the extent of quadrupole deformation (elongation) and the asymmetry parameter γ, that indicates the deviation from axial symmetry. The parameters β_2 and γ are defined in terms of the ratio $\delta R_i / R_0$ where δR_i is the deviation of the radius vector along i^{th} axis (x, y and z in the nuclear body-fixed coordinate system) with respect to a sphere having the same volume as the nucleus

and R_0 is the magnitude of the radius vector of the sphere. The ratio $\delta R_i/R_0$ is connected to β_2 as:

$$\delta R_x/R_0 = (5/4)^{1/2} \cos{(\gamma - 2\pi/3)},$$
$$\delta R_y/R_0 = (5/4)^{1/2} \cos{(\gamma - 4\pi/3)}, \qquad (2.15)$$
$$\delta R_z/R_0 = (5/4)^{1/2} \cos{(\gamma)}.$$

When $\beta_2 > 0$ and $\gamma = 0°$, the nuclear shape corresponds to an axially deformed prolate shape and when $\gamma = 60°$, the nuclear shape corresponds to an axially deformed oblate shape. The combination of nuclear shape and rotational motion is best denoted using the Lund convention, Figure 2.3. At $\gamma = 0°$ the shape is prolate and the rotational motion is perpendicular to the symmetry axis (collective prolate), while it is collective oblate at $\gamma = -60°$ because the shape is oblate and the rotation is around an axis perpendicular to the symmetry axis. The non-collective nuclear shapes are observed at $\gamma = -120°$ and $\gamma = 60°$ for prolate and oblate shapes respectively, as the rotation occurs around the symmetry axis. A nucleus is triaxial if $\beta_2 > 0$ and $\gamma \neq 0°, \pm 60°, -120°$.

It should be mentioned that parametrizing the nuclear deformation in terms of (β_2, γ) is not unique. Another way to do this is by using the Nilsson deformation parameters, (ε_2, γ) parametrization, where γ is the same as before and ε_2 is the Nilsson elongation parameter and has the same meaning as β_2, albeit having a slightly different value of $\varepsilon_2 \approx 0.95\beta_2$.

In addition to quadruple deformations it is possible for the nucleus to have higher-order deformations, for example when $\lambda = 3$ in equation 2.12 it corresponds to an octupole deformed nuclear shape, and when $\lambda = 4$ it corresponds to a hexadecapole deformed nuclear shape. In general, these higher-order deformations are more rare compared to quadruple deformations.

2.3.1 The Nilsson Model

Most nuclei have stable quadruple deformations in their ground-state. The Nilsson model was developed to account for this. It is based on a modified harmonic oscillator. The potential of equation 2.10 assumed radial symmetry and homogeneity
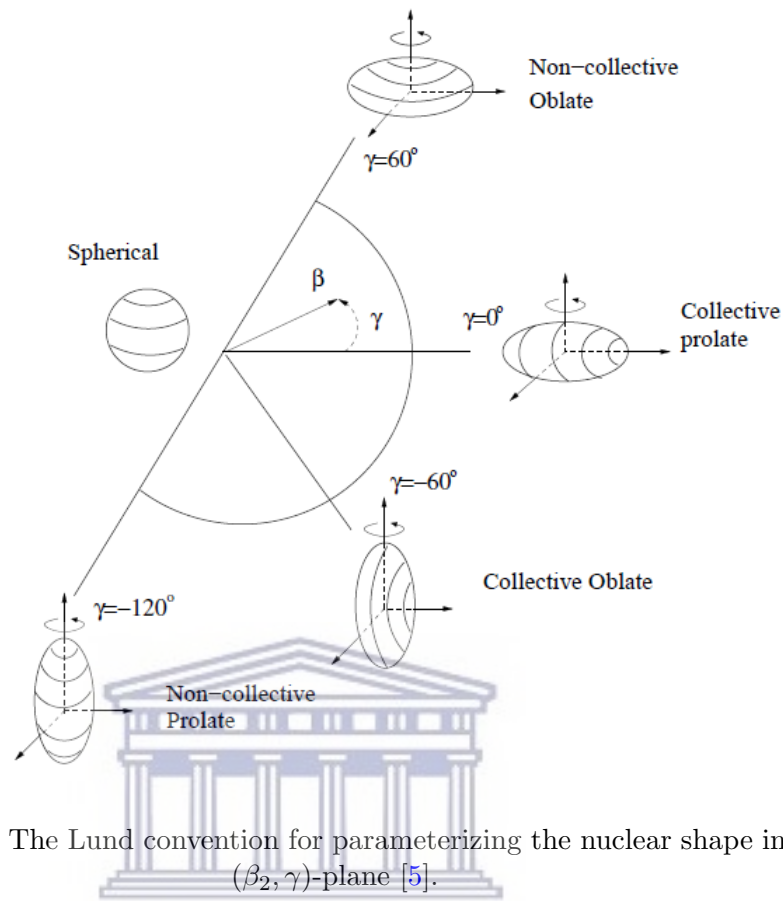
FIGURE 2.3: The Lund convention for parameterizing the nuclear shape in the (β_2, γ)-plane [5].

along all nuclear axes. Within the Nilsson model this needs not be the case. When a nucleus has an axially symmetric quadruple ($\lambda = 2$) deformation, it can either be prolate ($\varepsilon_2 > 0$) or oblate ($\varepsilon_2 < 0$) depending on whether the intrinsic-frame nuclear symmetry (z) axis is long (prolate, $z > x = y$) or short (oblate, $z < x = y$). The nuclear potential follows the nuclear matter distribution and extends further along the z axis if the nucleus is prolate deformed and is shortened with respect to the z axis if the nucleus has an oblate deformation.

For a deformed nuclear system, the Hamiltonian of the modified harmonic oscillator potential equation 2.11 takes the form:

$$\hat{H} = \hat{T} + \frac{1}{2}M(\omega_x^2 x^2 + \omega_y^2 y^2 + \omega_z^2 z^2) + Cl^2 + D(f_{so}(r)\vec{l} \cdot \vec{s}), \qquad (2.16)$$

where $\hat{T}$ is the kinetic energy operator as defined in section 2.1, ω_x, ω_y and ω_z are related to the deformation parameters (ε_2, γ) as in Ref. [39]. For the axially symmetric case, $\omega_x^2 = \omega_y^2 = \omega_\perp^2 \neq \omega_z^2$, with $\omega_\perp$ (ω_z) as the oscillator frequency in a direction orthogonal (parallel) to the body-fixed symmetry (z) axis:

$$\omega_x = \omega_0(1 - \frac{2}{3}\varepsilon_2 \cos{(\gamma + \frac{2}{3}\pi)}), \qquad (2.17)$$

$$\omega_y = \omega_0(1 - \frac{2}{3}\varepsilon_2 \cos{(\gamma - \frac{2}{3}\pi)}), \qquad (2.18)$$

$$\omega_z = \omega_0(1 - \frac{2}{3}\varepsilon_2 \cos{\gamma}). \qquad (2.19)$$

In the axially deformed case the Hamiltonian becomes:

$$\hat{H} = \hat{T} + \frac{1}{2}M(\omega_\perp^2(x^2 + y^2) + \omega_z^2 z^2) + Cl^2 + Df_{so}(r)\vec{l}\cdot\vec{s}. \qquad (2.20)$$

To ensure that the volume of the nucleus remains constant, a volume conservation condition is imposed, $\omega_x\omega_y\omega_z = \omega_0^3 = $ const, where ω_0 is the spherical oscillator frequency and is related to the mass number A by $\hbar\omega_0 = 41A^{-\frac{1}{3}}$MeV.

The presence of quadruple deformations splits the degenerate energy levels of the spherical shell model. While in the spherical shell model, all states with the same total angular momentum j in a sub-shell have the same energy, in the Nilsson model this sub-shell splits into states of differing energy, depending on the projections of the total single-particle angular momentum $\vec{j}$ onto the nuclear symmetry axis.

For instance, in the context of the spherical shell model, the sub-shell $1g_{\frac{7}{2}}$ can accommodate a total of $2(\frac{7}{2}) + 1 = 8$ nucleons, all with the same energy. In the deformed Nilsson model, the $1g_{\frac{7}{2}}$ is split into $\frac{(2j+1)}{2}$ different orbitals with differing j projections onto the symmetry axis ($\Omega = \frac{7}{2}, \frac{5}{2}, \frac{3}{2}, \frac{1}{2}$) (see Figure 2.5 and 2.6). The total occupation number of the sub-shell does not change. Each Nilsson orbital accommodates two nucleons, in accordance with the Pauli exclusion principle. In the prolate (oblate) case, the Nilsson orbital with projection of $\Omega = \frac{7}{2}$ lies highest (lowest) in energy, followed by the orbital with projection $\Omega = \frac{5}{2}$ and so forth, the Nilsson orbital with projection of $\Omega = \frac{1}{2}$ is lowest (highest) in energy. At $\varepsilon_2 = 0$ the degeneracy of the sub-shells into different orbitals disappears and the Nilsson model becomes equivalent to the spherical shell model.

Each Nilsson orbital can be uniquely identified by the Nilsson quantum numbers $\Omega[N, n_z, \Lambda]$. Ω is the projection of the single-particle angular momentum j onto the symmetry axis. N is the oscillator shell number and n_z is the number of oscillator quanta in the direction of the symmetry axis. In this model $\Omega = \Lambda + \Sigma$, where
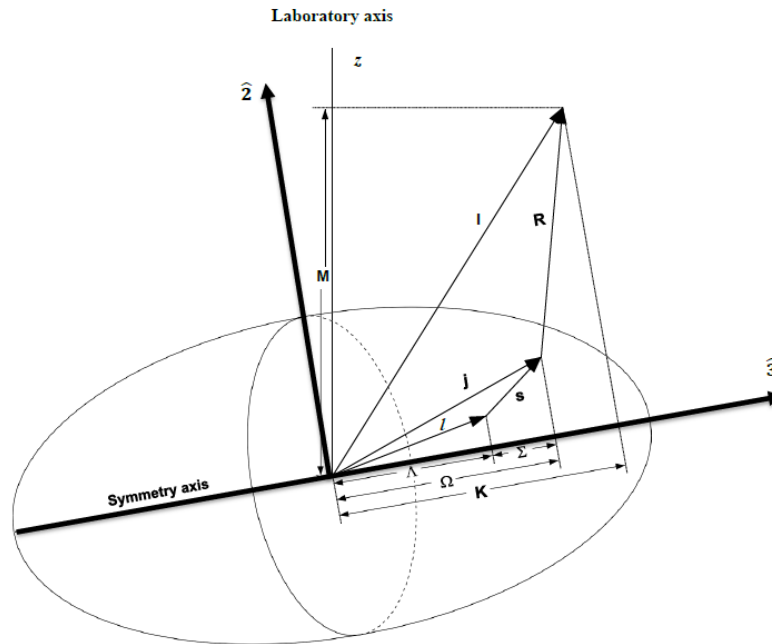
FIGURE 2.4: An illustration of angular momentum coupling in the Nilsson model. Adapted from Ref. [1].

Λ represents the projection of the orbital angular momentum onto the symmetry axis, and Σ is the projection of the intrinsic spin angular momentum onto the symmetry axis.

The coupling of angular momentum in the Nilsson model is illustrated in Figure 2.4. $\vec{R}$ is the rotational angular momentum of the nucleus and M is the projection of the total nuclear spin, $\vec{I} = \vec{R} + \vec{j}$ onto the laboratory z axis. In the absence of rotation, the parity π and Ω are good quantum numbers in the Nilsson model. Note, that axially symmetric nuclei can only rotate around an axis that is orthogonal to the symmetry axis. Therefore, $I = \Omega = K$ at the bandhead.

Due to the pairing interaction in the Nilsson model all the nucleons inside the core are paired up. If the nucleus is odd-even or even-odd, all nuclear spin I in the ground state is entirely due to the unpaired odd nucleon, that is $I = j$ in a non-rotating nucleus. In the the case of an odd-odd nucleus, the single-particle angular momentum is the vector sum of the unpaired nucleons single-particle angular momenta $\vec{j} = \vec{j_\pi} + \vec{j_\nu}$, with $\vec{j_\pi}$ and $\vec{j_\nu}$ representing the proton and neutron single-particle angular momenta, respectively. Figures 2.5 and 2.6 shows the Nilsson diagrams for neutrons and protons, respectively for occupation numbers between 50 and 82 for both.
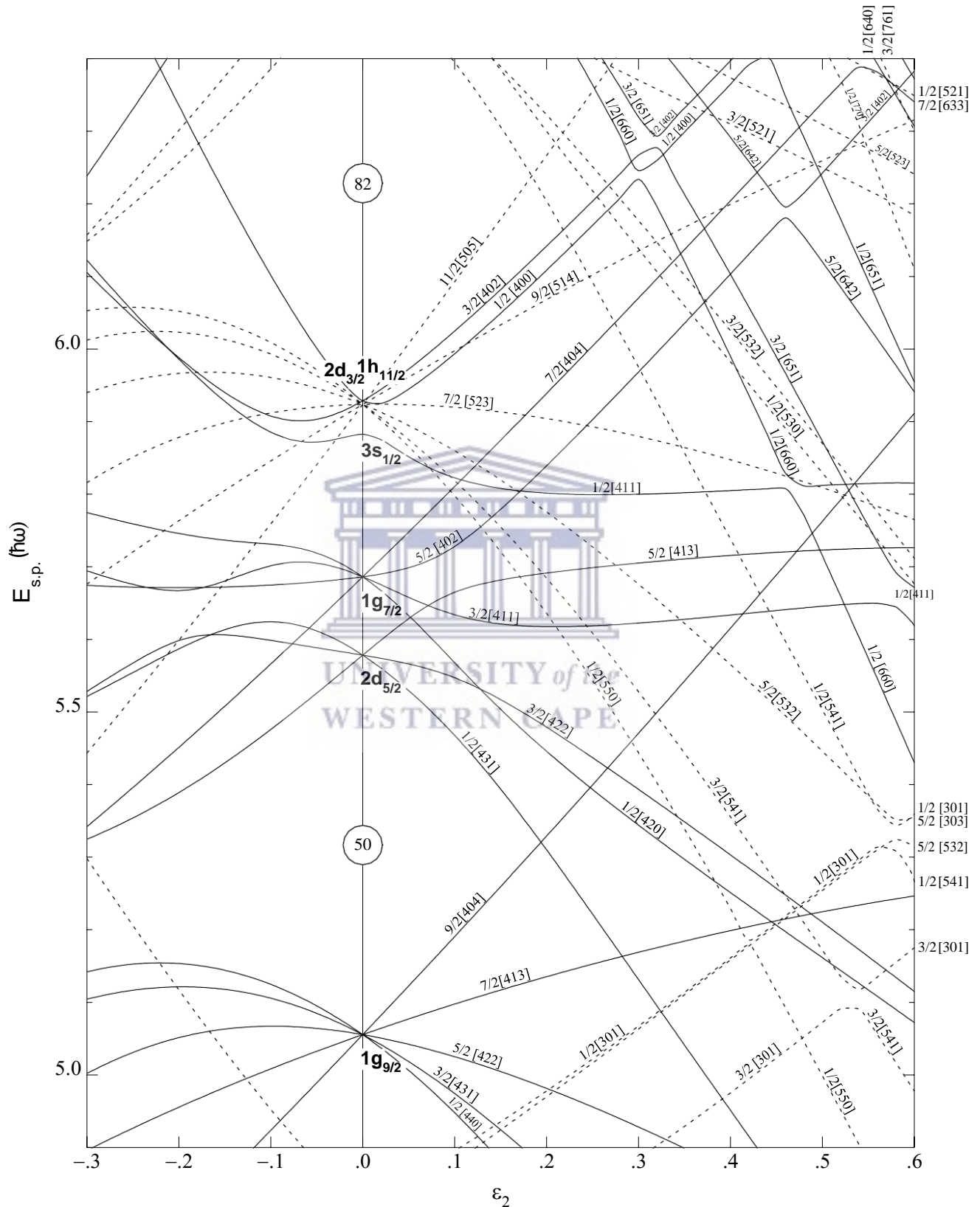
FIGURE 2.5: Nilsson diagram for neutrons, $50 \leq N \leq 82$ ($\varepsilon_4 = \frac{\varepsilon_2^2}{6}$). The solid lines represent orbitals with positive parity, $\pi = +1$ and the dashed lines are orbitals with negative parity, $\pi = -1$. Each orbital is labelled with the asymptotic Nilsson quantum numbers $\Omega[N, n_z, \Lambda]$. Adapted from Ref. [1].
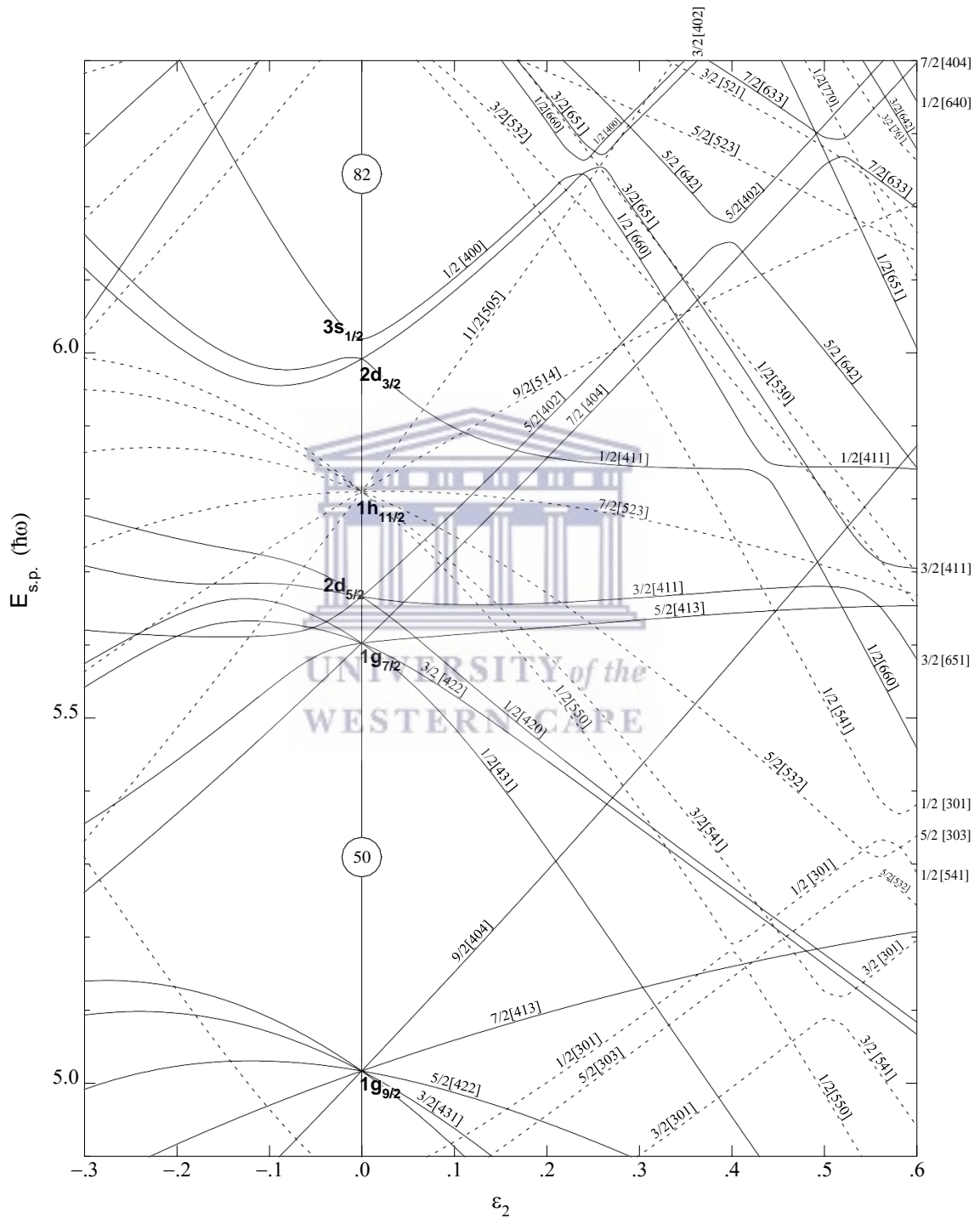
FIGURE 2.6: Nilsson diagram for protons, $50 \leq N \leq 82$ ($\varepsilon_4 = \frac{\varepsilon_2^2}{6}$). The solid lines represent orbitals with positive parity, $\pi = +1$ and the dashed lines are orbitals with negative parity $\pi = -1$. Each orbital is labelled with the asymptotic Nilsson quantum numbers $\Omega[N, n_z, \Lambda]$. Adapted from Ref. [1].

2.4 Nuclear Collectivity

When a nucleus absorbs energy it can exhibit two extreme types of behaviour; (i) single-particle excitations of the individual valence nucleon to a different single-particle state and (ii) collective mode of excitation, which is characterised by a coherent movement of a large number of nucleons. Single-particle excitations change the internal configurations of the nucleus. The spectra of the single-particle excitations consist of irregular sequences of states that are connected by gamma-ray transitions of different multipolarities. Collective modes of excitations such as vibrations and rotational motion, leave the internal single-particle configuration of the nucleus unchanged. Nuclear vibrations, while straightforward to treat [15], are not very important to the understanding of the current work, consequently no further attention will be paid to them, and only nuclear rotations will be discussed. The interplay between single-particle and collective degrees of freedom underpins a diverse range of phenomena in nuclear structure.

2.4.1 Nuclear Rotations

Due to spherical symmetry the rotation of spherical nuclear systems is forbidden by quantum mechanics as such rotational motion would only introduce a trivial phase factor to the wavefunction that is, there is absolutely no way to distinguish between a rotating spherical nucleus to one that is stationary. Only deformed nuclei can access the rotational mode of excitation [19]. Such rotational motion manifests as a regular sequence of states with increasing angular momentum. Rotational motion of the nucleus takes place around an axis that is orthogonal (the $\hat{2}$-axis in the body fixed system) to the symmetry axis, see Figure 2.4.

Classically, the energy of a rigid rotor as a function of the rotational angular momentum $\vec{R}$ is given by [38]:

$$E = \frac{\vec{R}^2}{2\Im},$$ (2.21)

where $\Im$ is the moment of inertia of a rigid rotor. By quantizing equation 2.21, we get:

$$E = \frac{\hbar^2}{2\Im}[I(I+1)]. \tag{2.22}$$

For even-even nuclei, $\vec{R} = \vec{I}$, with $\vec{I}$ as the total nuclear spin. The eigenvalue of the operator $\hat{\vec{I}}^2$ is $I(I+1)$. In this case, the energy eigenvalues of equation 2.22 consist of positive-parity states with spin sequence $I = 0, 2, 4, 6, 8, ...$ with $I = 0$ as the ground state, this sequence of states is linked by $\Delta I = 2$ gamma-ray transitions forming what is known as the ground-state (g.s.) rotational band.

The set of rotational states is distinguishable from the global set of states in the gamma-ray spectra of the nucleus because they exhibit a regular relationship between the energy of the state which is proportional to the angular momentum I of the state, $E \propto I(I+1)$. The states are linked by stretched pure E2 transitions. Other rotational bands are possible, for example excited rotational bands can form when a pair of nucleons is broken and promoted to a different shell-model configuration. It is possible to have $I = K$ as the lowest state in the rotational band, but also it is possible to have bands built on a $I = j$ state.

In contrast to an axially deformed nuclei, a triaxially deformed nucleus can rotate around any one of its three principle nuclear axes as no axis of symmetry is present in the system.

2.4.2 Particle-Rotor Coupling

In an odd-A deformed nucleus, the single-particle and collective degrees of freedom are coupled together to describe the behavior of the nucleus. The total nuclear spin is given by:

$$\vec{I} = \vec{R} + \vec{j}. \tag{2.23}$$
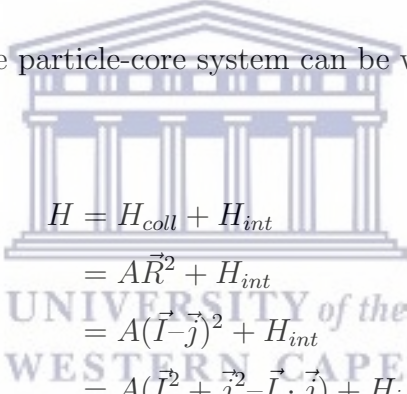
Thus, the rotational angular momentum is $\vec{R} = \vec{I} - \vec{j}$. In the description of axially deformed odd-A nuclei two extreme cases arise when single-particle angular momentum, $\vec{j}$ is coupled to the rotational angular momentum, $\vec{R}$ depending on the strength of the strength of Coriolis interaction and their relative orientation. They can either be oriented orthogonal to each other (strong coupling) or parallel to each other (rotational alignment).

2.4.2.1   Strong-coupling limit

For an axially symmetric nucleus the properties of the low-lying states are determined by the valence nucleon. The total nuclear spin $\vec{I}$ has a projection of K onto the nuclear symmetry axis. The rotational motion of the nucleus proceeds around an axis that is orthogonal to the nuclear symmetry axis. There is no collective rotation around the symmetry axis, the $\hat{3}$-component of $\vec{R}$ vanishes and the projection of $\vec{I}$ onto the symmetry axis is entirely due to the projection Ω of the single-particle angular momentum $\vec{j}$. That is $I_3 = \Omega = K$. Therefor, both Ω and K are good quantum numbers of the system.

In this coupling scheme, the Hamiltonian of the whole system is additive and the corresponding total nuclear wavefunction is a simple product of the inert core wavefunction and the intrinsic single-particle wavefunction.

The Hamiltonian of the particle-core system can be written as:

$$
\begin{aligned}
H &= H_{coll} + H_{int} \\
&= A\vec{R}^2 + H_{int} \\
&= A(\vec{I} - \vec{j})^2 + H_{int} \\
&= A(\vec{I}^2 + \vec{j}^2 - \vec{I} \cdot \vec{j}) + H_{int},
\end{aligned}
\tag{2.24}
$$

where $H_{coll} = AR^2$ is the collective rotational Hamiltonian with $A = \frac{\hbar^2}{2\Im}$ and $\vec{R} = (\vec{I} - \vec{j})$. The term H_{int} corresponds to the deformed intrinsic single-particle Hamiltonian, (for instance the Nilsson model Hamiltonian). By noting that $\vec{j} = \vec{j}_1 + \vec{j}_2 + \vec{j}_3$, and quantizing along the $\hat{3}$ axis as well as writing $\vec{j}_1$ and $\vec{j}_2$ in terms of the raising and lowering operators, equation 2.24 can be further simplified:

$$
H = H_{int} + A[I^2 - K^2 + (j_1^2 + j_2^2) - (I_+ j_- + I_- j_+)].
\tag{2.25}
$$

The last two terms correspond classically to the Coriolis and centrifugal forces. It gives the coupling between the motion of the valence nucleon in the deformed potential to that of the rotating core and causes mixing of states. In the strong coupling regime (adiabatic approximation), the influence of the rotating core on the single-particle motion is negligible (for small I). Only the diagonal matrix
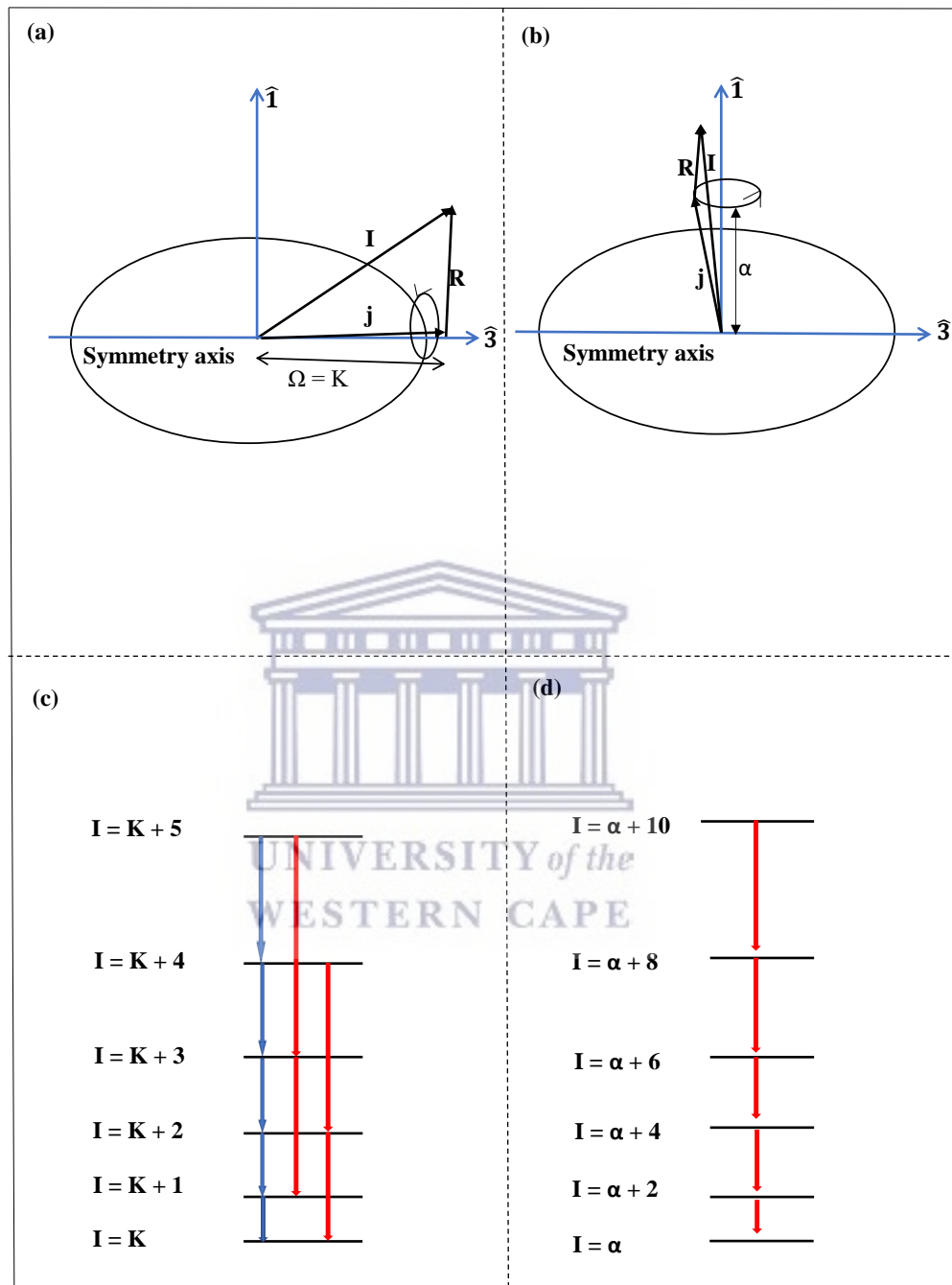
FIGURE 2.7: Particle-core angular momentum coupling (a) the strong coupling limit, (b) the rotational alignment limit. The observed band structures associated with them, in panel (c) the strong-coupling limit, and in panel (d) the rotational alignment limit. The transitions that link the states of the bands in panels (c) and (d) are shown with arrows. The blue arrows denote M1+E2 transitions, the red arrows correspond to pure E2 transitions.

elements of the Coriolis term have any influence on the system. The selection rules for j_+ and j_- mean that these operators act only for $\Omega = \pm 1/2$. The recoil term $(j_1^2 + j_2^2)$ is influenced only by the single particle wavefunctions and is rather constant and small for a given rotational band and can be neglected.

From the Nilsson model, $H_{int}\psi_\nu = \varepsilon_\nu \psi_\nu$, where ε_ν is the single-particle energy associated with the operator H_{int}, ψ_ν is the corresponding eigenstate labelled by the Nilsson numbers; $\psi_\nu = |NLJ\Omega\rangle$.

The energy of a state with given I and K is:

$$E_K(I) = |\varepsilon_\nu - \lambda_F| + A[I(I+1) - K^2] \ , \ K \neq \frac{1}{2}. \tag{2.26}$$

Energy is evaluated relative to the Fermi level λ_F. The bandhead in the yrast band (a rotational band formed with lowest energy states for a given I) has spin $I = K$. The states in the band will have an increasing spin, $I = K, K+1, K+2, K+3, ...,$ (see panels (a) and (c) in Figure 2.7). The states are linked with both pure stretched E2 transitions (for states with $\Delta I = 2$, shown in red in Figure 2.7) and mixed M1+E2 transitions (for states with $\Delta I = 1$, shown in blue in Figure 2.7). Besides the yrast band it is possible to observe other rotational bands. These can be formed by the promotion of the odd nucleon to a higher Nilsson orbital and building a rotational band on this new configuration.

For $K = \frac{1}{2}$ the diagonal contributions of the matrix element of the $(I_+j_- + I_-j_+)$ operator are non-zero and in this case, the energy of the rotational band is calculated as:

$$E_K(I) = |\varepsilon_\nu - \lambda| + A[I(I+1) - K^2 + \delta_{K\frac{1}{2}} a(-1)^{I+\frac{1}{2}}(I + \frac{1}{2})], \tag{2.27}$$

where a is called the decoupling parameter and has a fixed value for each $K = \frac{1}{2}$ orbital. It is given by:

$$a = \sum_j (-1)^{j-\frac{1}{2}}(j + \frac{1}{2})|C_{j\frac{1}{2}}^{(\alpha)}|^2, \tag{2.28}$$

and it corresponds to the decoupling of the particle motion from the rotor. This decoupling profoundly affects the order of the states in a rotational band, depending on the value of a. If $a = 0$, the ordering is identical to that predicted by relation 2.26. If $|a| = 1$, the states occur in degenerate pairs. For $a = -1$, the $\frac{1}{2}$ and $\frac{3}{2}$ states are degenerate and have the following pairs of states $(\frac{5}{2}, \frac{7}{2})$, $(\frac{9}{2}, \frac{11}{2})$,... When $a = +1$, the degenerate pairs are: $(\frac{3}{2}, \frac{5}{2})$, $(\frac{7}{2}, \frac{9}{2})$, $(\frac{11}{2}, \frac{13}{2})$... If $|a| > 1$, the spin sequence in a rotational band is no longer monotonic. In general the Coriolis term has the effect of mixing two different rotational bands for which $\Delta K = \pm 1$.

2.4.2.2   Rotational alignment limit

In this limiting case the angular momentum of the valence nucleon, $\vec{j}$ is parallel to the rotational angular momentum of the core $\vec{R}$. In even-even nuclei a rotational band is built on the 0^+ ground state. A sequence of pure E2 transitions link the states of this band. The spectrum of an odd-A nucleus whose single-particle angular momentum aligns itself with the core rotation, on the other hand, will have a rotational band that is built on the ground state with spin $I = \alpha$, where α is the projection of $\vec{j}$ on the rotational axis, see panel (b) of Figure 2.7. The states of the band have spin $I = \alpha, \alpha + 2, \alpha + 4,...$ etc. and are linked with pure E2 transitions. That is, in the rotationally aligned case only one sequence of E2 transitions is observed, (see panels (b) and (d) in Figure 2.7). The band structures in the rotational alignment limit are similar to the ground state bands of the neighboring even-even nuclei.

In the rotational aligned case the energy of the rotational states is given by:

$$E_{rot} = \frac{\hbar^2}{2\Im} R(R + 1) + 2\alpha. \tag{2.29}$$

2.5   Signature splitting

In the absence of rotation, parity (π) and and the projection of $\vec{j}$ on the nuclear symmetry axis, Ω are good quantum numbers in the Nilsson model. Introduction of nuclear rotation breaks the time-reversal symmetry of the system as such, and Ω becomes two-fold degenerate. Because of the loss of time-reversal symmetry, an additional quantum number called the signature (α) is required to labelled states

in a rotational band. The signature quantum number, α describes invariance of the axially symmetric potential with respect to a rotation of 180° perpendicular to the symmetry axis. The rotation operator [70] is given by:

$$\hat{R}_k = e^{i\pi j_k},\tag{2.30}$$

where k denotes the intrinsic $(\hat{1}, \hat{2}, \hat{3})$ nuclear axes and j_k the projection of the single-particle angular momentum onto the k axis. The signature quantum number, α is defined as:

$$r = e^{i\pi\alpha},\tag{2.31}$$

where r is the eigenvalue of the rotation operator, $\hat{R}$. The signature quantum number is related to the total angular momentum I by:

$$\alpha = I \bmod 2.\tag{2.32}$$

That is, for even-A nuclei the signature is related to the angular momentum as:

$$I = 0, 2, 4, ..., r = +1, \alpha = 0,\tag{2.33}$$

$$I = 1, 3, 5, ..., r = -1, \alpha = 1.\tag{2.34}$$

For odd-A nuclei:

$$I = 1/2, 5/2, 9/2, ..., r = -i, \alpha = +1/2,\tag{2.35}$$

$$I = 3/2, 7/2, 11/2, ..., r = +i, \alpha = -1/2.\tag{2.36}$$

A rotational band built on a given intrinsic configuration (with $K \neq 0$) splits into two families of $\Delta I = 2$ sequences with different signature. These are known as signature partner bands and they differ from each other by $1\hbar$. In general signature

partner bands may not be energetically equivalent. One lies lower in energy and is then called the "favored" configuration, while the other is "unfavored" and lies higher in energy. This results in signature splitting, which is strongly affected by the Coriolis interaction. Signature splitting is usually characterized by the parameter $S(I)$ and defined as:

$$S(I) = [E(I) - E(I-1)] - \frac{[E(I+1) - E(I) + E(I-1) - E(I-2)]}{2}. \quad (2.37)$$

The $S(I)$ values appear as a typical staggering curve when plotted as a function of nuclear spin, I (see Figure 2.8). In some cases the favored and unfavored signature partner bands can cross and interchange their roles, then the signature splitting changes its phase at a given spin. This phenomenon is known as signature inversion [10]. In a one-quasiparticle (1-qp) configuration in a high-j orbital, the favored signature configuration is obtained by:

$$\alpha_f = \frac{1}{2}(-1)^{j-\frac{1}{2}}. \quad (2.38)$$
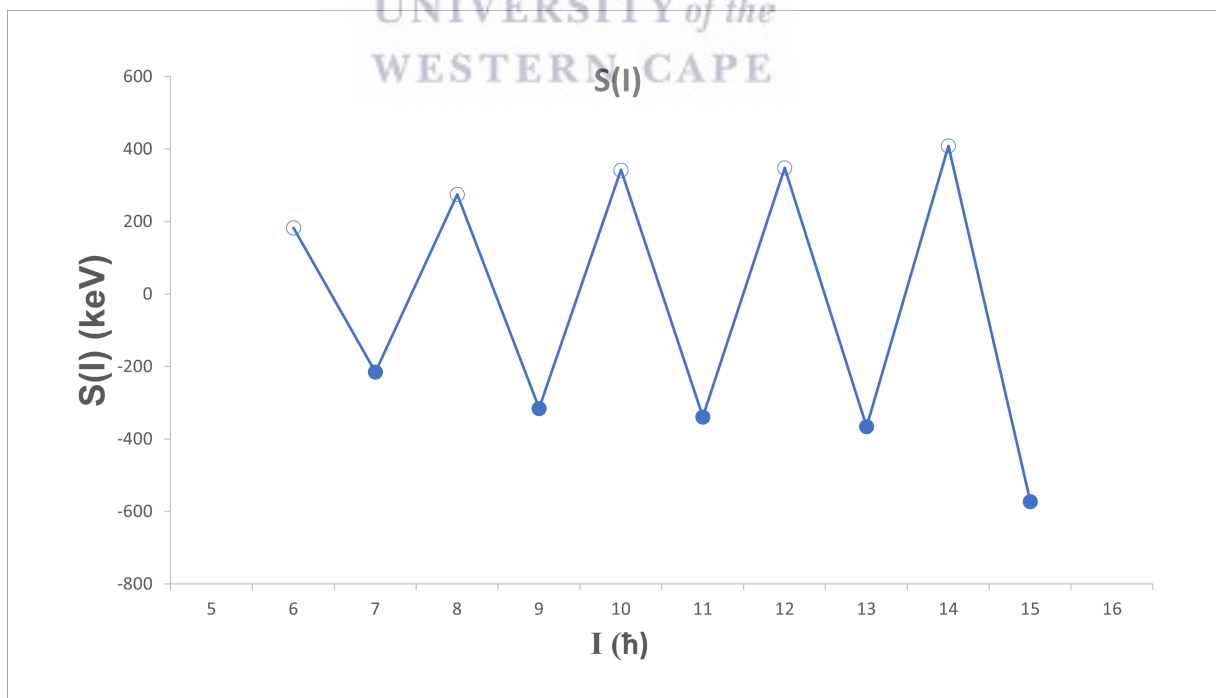
FIGURE 2.8: An illustration of a typical energy staggering curve. Filled circles denote the favored signature branch, while the open circles denote the unfavored signature branch.

Chapter 3

Nuclear Triaxiality

3.1 Introduction

In the preceding chapter we looked at the axially symmetric rotor and the band structures arising from such nuclear rotations where K, the projection of the total nuclear spin I, was a good quantum number. When the nucleus is triaxial, there is no axis of symmetry and K is no longer a good quantum number. A triaxial nucleus can rotate around any one of its body-fixed axes simultaneously. The spectra of triaxial nuclei can exhibit complex patterns. This chapter is devoted to reviewing the current understanding of the rotational states in non-axially deformed nuclei.

3.2 The Asymmetric Particle-Plus-Rotor Model

Rotations of triaxially deformed even-even core is governed by:

$$
\begin{aligned}
H_{rot} &= \hbar^2 \sum_{k=1}^{3} \frac{R^2}{2\Im_k} \\
&= \hbar^2 \left[\frac{R_1^2}{2\Im_1} + \frac{R_2^2}{2\Im_2} + \frac{R_3^2}{2\Im_3} \right] \\
&= \hbar^2 [A_1 R_1^2 + A_2 R_2^2 + A_3 R_3^2],
\end{aligned}
\tag{3.1}
$$

where $k = 1, 2, 3$ are the intrinsic (body-fixed) axes, representing the intermediate, short and long axes respectively. The moments of inertia (MoI) $\Im_k$, are usually described by the irrotational flow model and are defined as [20, 21]:

$$\Im_k = \frac{4}{3}\Im_0 \sin^2(\gamma - \frac{2\pi}{3}k). \tag{3.2}$$

Among them $\Im_1$ is the largest. For $0° < \gamma < 30°$, $\Im_1 > \Im_2 > \Im_3$ and if $30° < \gamma < 60°$, $\Im_1 > \Im_3 > \Im_2$. In this work irrotational-flow MoI's are assumed as this choice is supported by experimental evidence [2]. The rotation proceeds mostly around the intermediate axis which is favored, as this axis has the largest MoI and thus rotation around this axis needs minimum energy. The Hamiltonian (equation 3.1) becomes:

$$H = A_1 I_1^2 + A_2 I_2^2 + A_3 I_3^2, \tag{3.3}$$

where $A_k = \hbar^2/2\Im_k$. The solutions to the Hamiltonian presented in relation 3.3 is a series of rotational states, which include the ground-state band and several excited rotational bands. The excited bands are often termed $\gamma-$bands [74]. To distinguish these exited low-lying rotational states from the $K = 2$, $K = 4$, etc. $\gamma-$bands that result from the Bohr Hamiltonian [15], which are produced by coupling the rotational and vibration collective modes, the rotational bands in triaxial nuclei were called Tilted Precession Bands [42] as they represent the simultaneous precession of the nucleus around all three nuclear axes, see Section 3.2.1.
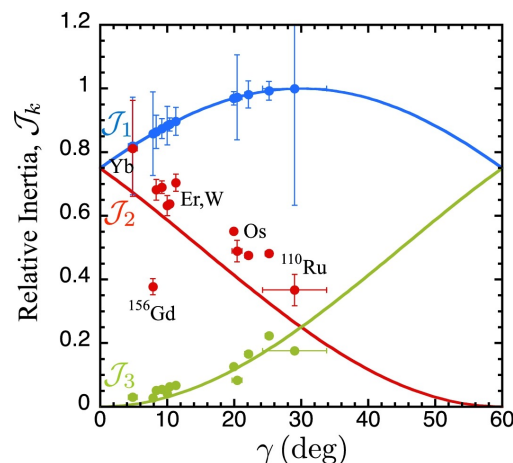
FIGURE 3.1: Empirically measured MoIs for some nuclei as a function of the γ-deformation. Adapted from Ref. [2].

The excited bands arise from the solutions of the $3D$ Hamiltonian. There is exactly one state with $I = 0$, no state with $I = 1$, two states with $I = 2$, one state with $I = 3$, three states with $I = 4$, two states with $I = 5$, four states with $I = 6$ etc. That is the spin sequence predicted by the model goes like: $I = \{0, 2, 2, 3, 4, 4, 4, 5, 5, 6, 6, 6, 6, ...\}$. These states can be organized in the following way to form rotational bands; the ground state band is formed by the lowest energy states with spin sequence $I = 0, 2, 4, 6, ...$, the first excited band consists of the sequence $I = 2, 3, 4, 5, 6...$, the next excited band is formed by $I = 4, 5, 6, 7, 8...$. The third excited band is made up of the spin sequence $I = 6, 7, 8, ...$ with $K = 6$ etc. The arrangement of rotational states of a triaxial rotor is presented in Figure 3.2, and described in more details in the next section.

3.2.1 Tilted-precession bands

Perhaps a better way to describe the excited rotational bands that result from the rotation of even-even triaxial nuclei is by modelling them as a consequence of the tilting of the total angular momentum vector $\vec{I}$ away from the intermediate axis and precessing around this axis. As stated previously, the intermediate axis has the largest moment of inertia and rotation around this axis is preferred. At $\gamma = 30°$ the Hamiltonian (equation 3.3) exhibits a symmetry, and the moments of inertia along the short and long axes (2 and 3, respectively) are equal ($\Im_2 = \Im_3$). Thus one can write the Hamiltonian as [42]:

$$H = \frac{3\hbar^2}{8\Im_0}[4I(I + 1) - 3R_1^2]. \tag{3.4}$$

The corresponding energy eigenvalues are:

$$E = \frac{3\hbar^2}{8\Im_0}[4I(I + 1) - 3i^2], \tag{3.5}$$

where i is the projection of $\vec{I}$ on the intermediate axis. When $i = |I|$, it corresponds to a full alignment of $\vec{I}$ along the intermediate axis, see Figure 3.2 (d) and the resulting sequence of $\Delta I = 2$ states forms the g.s. band as shown in Figure 3.2 (a). The excited bands are formed by tilting I away from the intermediate axis see panels (e) and (f) of Figure 3.2. When $i = I - 1$ and $i = I - 2$, the resulting
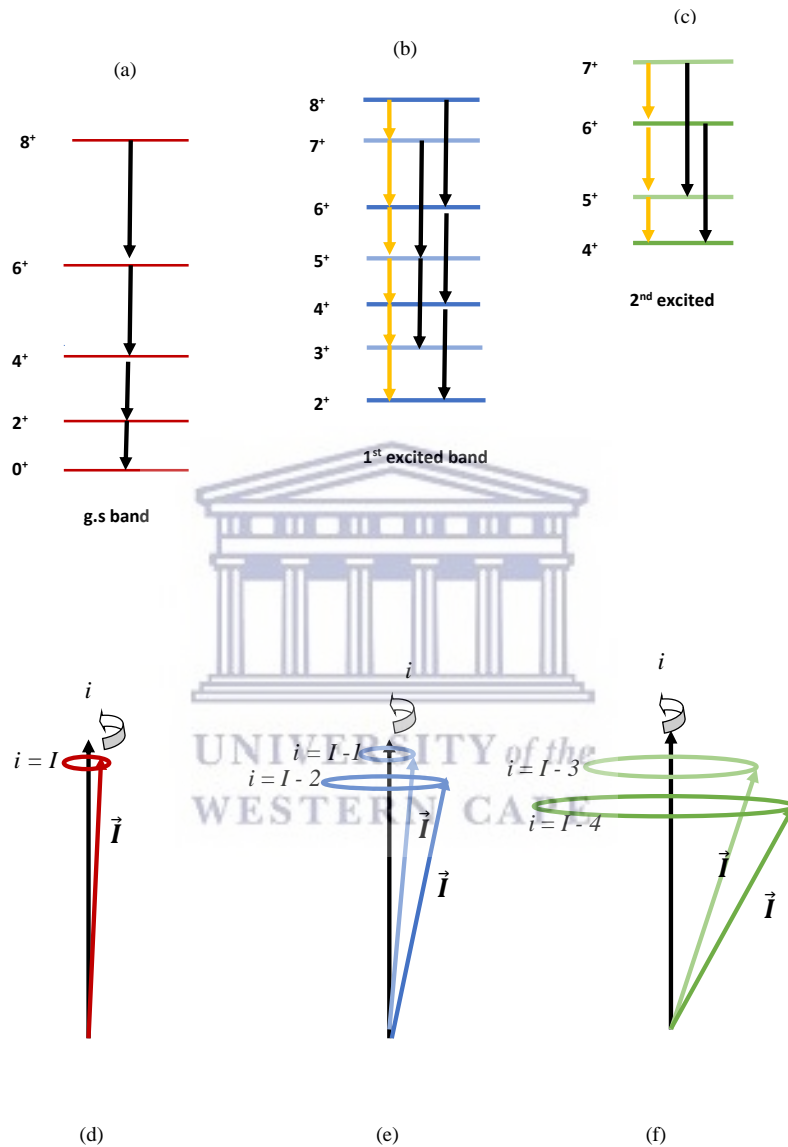
FIGURE 3.2: Spectrum of a triaxial even-even rotor. Panel (a) shows the ground-state band, $(i = I)$ (in red). Panel (b) shows the first excited band (blue states, $i = I - 2$. light-blue states $i = I - 1$). Panel (c) shows the second excited band (green states, $i = I - 4$; light-green states, $i = I - 3$). Black arrows denote E2 transitions, mixed M1+E2 transitions are represented by yellow arrows. Panels $(d) - (f)$ show the corresponding tilting of the angular momentum vectors.

sequence of states are the $\Delta I = 2$, odd- and even- spin sequences of the first excited band (shown in Figure 3.2 (b) in black), respectively. If $i = I - 3$ and $i = I - 4$, the corresponding rotational states form the odd- and even- spin sequences of the second excited band (shown in Figure 3.2 (c) in black). In fact, excited bands result when $i < |I|$, that is by tilting $\vec{I}$ away from the intermediate axis.

In odd-A nuclei, the rotational angular momentum of the core $\vec{R}$, is coupled to $\vec{j}$, the single-particle angular momentum of the nucleon (hole). Because the intermediate axis is the preferred axis of rotation for a triaxial rotor, generally $\vec{R}$ points in this direction. The single-particle angular momentum $\vec{j}$ can be coupled longitudinally (parallel) to $\vec{R}$ or, transversely (perpendicular) to $\vec{R}$ in the extreme limits [23]. The total angular momentum of a rotational state is the sum, $\vec{I} = \vec{R} + \vec{j}$. The Hamiltonian of the system for longitudinal and transverse coupling can be expressed as:

$$H = A_1(I_1 - j)^2 + A_2 I_2^2 + A_3 I_3^2 \text{ , for longitudinal coupling} \tag{3.6}$$

and

$$H = A_2(I_2 - j)^2 + A_1 I_1^2 + A_3 I_3^2 \text{ , for transverse coupling.} \tag{3.7}$$

Longitudinal coupling results when the single-particle angular momentum $\vec{j}$ is aligned along the intermediate axis. It occurs when the valence nucleon occupies an orbital near the middle of a given sub-shell. This results in a series of $\Delta I = 2$ states that form the yrast rotational band starting off with $I = j$ and proceeds with $I = j + 2$, $j + 4$, $j + 6$, ... Excited bands result from tilting $\vec{I}$ away from the intermediate axis. There are two distinct ways of doing this: (i) by tilting the collective angular momentum $\vec{R}$ or, (ii) by tilting the single-particle angular momentum $\vec{j}$ away from the intermediate axis.

When the single-particle angular momentum is transversely coupled to an even-even triaxial core, $\vec{R}$ points mainly along the intermediate axis and $\vec{j}$ points in a direction that is orthogonal to the intermediate axis, that is either along the short axis or along the long axis. In this case the valence nucleon occupies an orbital near the bottom (top) of a given sub-shell and points along the short (long) nuclear axis as it behaves as a particle (hole). The angular momentum in a transversely coupled rotational band can be generated in two ways; (i) by increasing $R_{||}$, the component of the rotational angular momentum along the intermediate axis which

results in bands of $\Delta I = 1$ nature or, (ii) by increasing $R_\perp$, the rotational angular momentum along the perpendicular axis, which results in bands of $\Delta I = 2$ nature.

For bands of $\Delta I = 1$ type and when the nuclear shape is axially symmetric the projections on the symmetry axis of the total angular momentum, K, and the single-particle angular momentum, Ω, are good quantum numbers. The band is built on the $I = \Omega = K$ state, and proceeds with $K + 1, K + 2, K + 3, ...$, forming the yrast band shown in black in panel (a) of Figure 3.3. High spin states in the yrast band are formed by increasing the rotational angular momentum along the intermediate axis $(R_\parallel)$. Due to triaxiality additional rotational bands are brought down in energy, shown in blue and red in panel (a) of Figure 3.3. K and Ω are not good quantum numbers in the triaxial case, however, it has been shown that for a nucleon in an $i_{13/2}$ or $h_{11/2}$ sub-shell and $\gamma \approx 30°$, K and Ω are approximately good quantum numbers, particularly near the bandhead [51].

To generate excited bands of $\Delta I = 1$ nature the nucleus increases its rotation along the orthogonal axis (long or short, depending on the orientation of $\vec{j}$) by $R_\perp \approx 2\hbar$. Thus the first excited band must have a bandhead of $I \approx \Omega + 2$. For instance a first excited band built on the $h_{11/2}$ orbital with $\Omega = 9/2$ has a bandhead of $I = 13/2$. It consists of states with $I = 13/2, 15/2, 17/2, 19/2...$, shown in blue in panel (a) of Figure 3.3. A second excited band is created by a further increase of $\approx 2\hbar$ in $R_\perp$, shown in red in panel (a) of Figure 3.3. Panel (b) of Figure 3.3 shows the generation of angular momentum for the yrast band (black), the first excited band (blue), and the second excited band (red). The symbols $\parallel$ and $\perp$ denote components along the intermediate axis and in a direction orthogonal to the intermediate axis, respectively.

The rotational bands can be classified by the projection of the single-particle angular momentum on the orthogonal axis $\Omega_\perp$, the projection of the total angular momentum on the orthogonal axis $K_\perp$, and the projection of the rotational angular momentum on the orthogonal axis $R_\perp$; $(\Omega_\perp, K_\perp, R_\perp)$. The yrast band consists of states with $(\Omega_\perp, K_\perp, R_\perp) = (9/2, 9/2, 0)$, the first excited band consists of states with $(\Omega_\perp, K_\perp, R_\perp) = (9/2, 13/2, 2)$, and the second excited band consists of states with $(\Omega_\perp, K_\perp, R_\perp) = (9/2, 17/2, 4)$.

The bands of $\Delta I = 2$ type can form when the strength of the Coriolis interaction is strong [44]. It is possible in some nuclei that the states with the same spin I and $R_\perp \approx 2$ lie lower in energy than the states with $R_\perp \approx 0$. For instance in ^{135}Pr
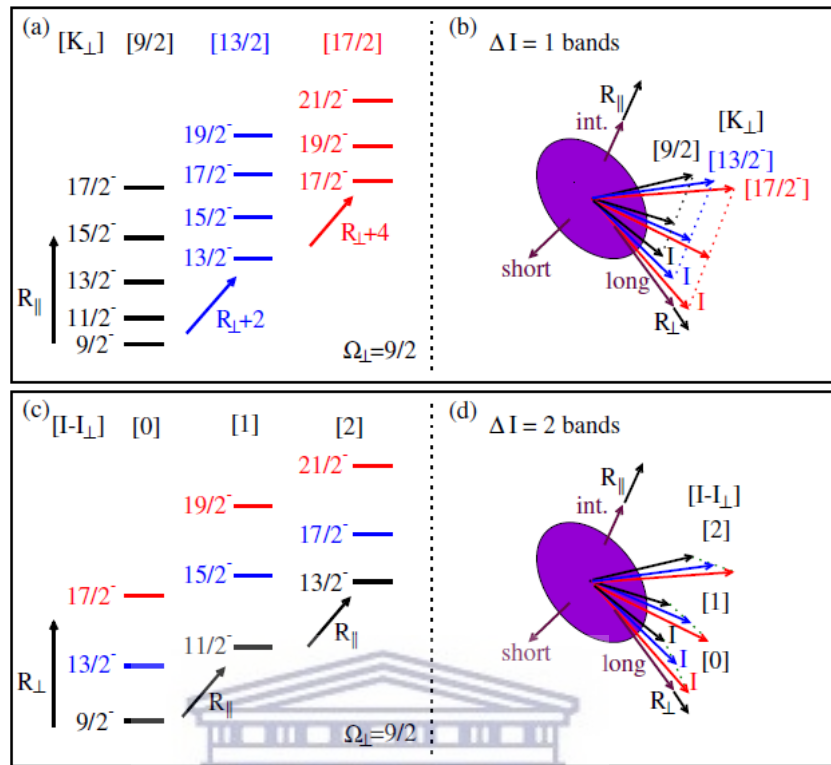
FIGURE 3.3: An illustration of transversely coupled for bands in odd-A triaxial nuclei based on the $h_{11/2}$ orbital with $\Omega = 9/2$. Panel (a) shows $\Delta I = 1$ bands and panel (b) illustrates the angular momentum generation mechanism. Panel (c) shows bands of $\Delta I = 2$ nature and panel (c) shows the corresponding mechanism of angular momentum generation. Adapted from Ref. [44].

the 13/2 state with the configuration $(\Omega_\perp, K_\perp, R_\perp) = (9/2, 13/2, 2)$, lies lower in energy than the 13/2 state with configuration $(\Omega_\perp, K_\perp, R_\perp) = (9/2, 13/2, 2)$ [45]. In this case the yrast rotational band consists of states with the lowest energy, which do not have the same $(\Omega_\perp, K_\perp, R_\perp)$. In fact, each state in the rotational band with $I > \Omega_\perp$ has an extra $2\hbar$ of angular momentum than the immediately preceding state forming $\Delta I = 2$ nature rotational states of the band, thus in such bands the rotation proceeds along the orthogonal axis. This is illustrated in panel (c) of Figure 3.3. Excited rotational bands are formed by increasing the rotational angular momentum along the intermediate axis. The first excited band has a bandhead spin of $I_{bandhead} = \Omega + 1$ and proceeds with the spin sequence; $I = I_{bandhead} + 2, I_{bandhead} + 4, I_{bandhead} + 6, ...$ The next excited band is built on a state with extra $1\hbar$ than the bandhead spin of the immediately preceding rotational band. Panel (c) of Figure 3.3 illustrates the $\Delta I = 2$ type rotational bands and panel (d) of Figure 3.3 represents the mechanisms of angular momentum generation.

3.2.2 Nuclear wobbling motion

Nuclear wobbling motion was proposed by Bohr and Mottelson for even-even nuclei in Ref. [15] as a collective mode of excitation which results when the nuclear density distribution along the three principle nuclear axes is unequal. For even-even triaxial rotors, the wobbling approximation replaces the $3D$ rotational Hamiltonian (equation 3.3) by simple $1D$ rotation coupled to wobbling phonon excitations,

$$H = A_1[I(I + 1)] + \hbar\omega(n + \frac{1}{2}).$$ (3.8)

The solutions of the wobbling Hamiltonian describe a set of rotational bands called wobbling bands, where ω is the wobbling frequency, $n = 0, 1, 2, ...$ is the number of excited wobbling phonons, where $n = 0$ corresponds to the g.s. band, $n = 1$ and $n = 2$ correspond to the odd and even spin sequences of the first excited (γ-) band, respectively etc. In fact each phonon excitation corresponds to an excited rotational band. Within the wobbling approximation, each phonon excitation causes a tilt of the rotational angular momentum away from the intermediate axis.

The wobbling frequency, ω is defined by the relation:

$$\hbar\omega = E(n, I) - E(n - 1, I).$$ (3.9)

Wobbling bands exhibit characteristic quantized behaviour for the excitation energies and transition probabilities. In particular:

(i) the energy of a rotational band has a linear dependence on n as;

$$E(n, I) = A_1[I(I + 1)] + \hbar\omega(n + \frac{1}{2}).$$ (3.10)

This relationship is manifested as equal spacing of excitation energies between two successive wobbling bands, for instance the excitation energy plots of the wobbling bands corresponding to $n = 0$ and $n = 1$ have the same energy spacing as that between wobbling bands with $n = 1$ and $n = 2$.

(*ii*) the intraband $B(E2)$ transition probabilities are identical for all wobbling bands, because they all correspond to rotations around the same axis−the intermediate axis;

$$B(E2; n, I \longrightarrow n, I \pm 2) = \frac{5}{16\pi} e^2 Q_2^2, \qquad (3.11)$$

(*iii*) the interband $B(E2)$ transition probabilities are linearly dependent on n, as they link bands with different phonon excitations;

$$B(E2; n, I \longrightarrow n-1, I-1) = \frac{5}{16\pi} e^2 (\sqrt{3} Q_0 x - \sqrt{2} Q_2 y)^2 \frac{n}{I}, \qquad (3.12)$$

where Q_0 and Q_2 denote the intrinsic and spectroscopic quadrupole moments, respectively. The wobbling approximation of the $3D$ rotational Hamiltonian is only valid at high spins [15]. Probably that is why wobbling had not been observed so far at low spins in even-even nuclei. Wobbling motion was observed experimentally in the $A \approx 160$ mass region, in the odd-A, $^{161-167}$Lu and ^{167}Ta isotopes, and the rotational bands corresponded to triaxial superdeformed nuclear shapes [4, 16, 31, 34, 55, 63].

Recently nuclear wobbling was investigated in odd-mass nuclei by Frauendorf and Dönau [23], and the concepts of transverse and longitudinal wobbling were proposed depending on whether the single-particle angular momentum was oriented perpendicular or parallel to the intermediate axis, respectively. Longitudinal (transverse) wobbling bands are expected to have (*i*) increasing (decreasing) wobbling frequency with increasing spin and, (*ii*) the $B(E2; n, I \longrightarrow n-1, I-1)$ and $B(M1; n, I \longrightarrow n-1, I-1)$ reduced transition probabilities should be proportional to n.

In addition two wobbling bands based on the same one-quasiparticle configuration and differing by one wobbling phonon $\Delta n = 1$, should be linked with $\Delta I = 1$, M1 + E2 transitions with dominant E2 nature, that is with a mixing ratio $|\delta| > 1$. Therefore, measuring mixing ratios with magnitudes larger than one is the necessary supporting experimental evidence for the wobbling interpretation. Mixing ratios with magnitudes larger than one were reported for several linking transitions in ^{135}Pr, ^{105}Pd, ^{183}Au, ^{133}La, ^{187}Au, ^{130}Ba and ^{127}Xe [49, 65], [73], [53], [14], [64], [18, 58], [17]. However, recently these results were questioned [27, 29, 45]
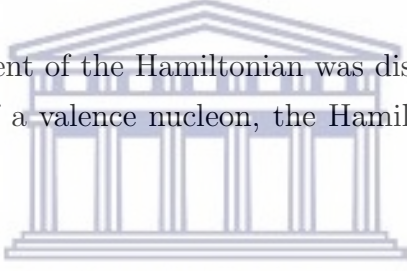
and new experimental data suggesting that the mixing ratios are in fact less than one were shown for ^{135}Pr [44].

3.3 The Quasiparticle-Plus-Triaxial Rotor (QTR) Model Formalism

The quasiparticle-plus-triaxial rotor (QTR) model has been used extensively to study triaxiality in odd-mass atomic nuclei [44, 52, 61]. The model Hamiltonian takes the form;

$$H = H_{coll} + H_{int}. \tag{3.13}$$

The collective component of the Hamiltonian was discussed in Sections 2.4.2 and 3.2. In the presence of a valence nucleon, the Hamiltonian can be written down as:

$$
\begin{aligned}
H_{coll} &= \sum_{k=1}^{3} \frac{R^2}{2\Im_k} \\
&= \sum_{k=1}^{3} \frac{(I_k - j_k)^2}{2\Im_k},
\end{aligned}
\tag{3.14}
$$

where $\vec{I}, \vec{R}, \vec{j}$ have their usual meaning as the total, collective core, and the single-particle angular momentum vectors and $\vec{R} = \vec{I} - \vec{j}$. The $\Im_k$ are the moments of inertia along the k axis, with $k = 1, 2, 3$. Irrotational-flow type moments of inertia are assumed.

3.3.1 QTR energies and wavefunctions

The intrinsic part of the Hamiltonian can be written down as,

$$H_{int} = H_{sp} + H_{pair}$$
$$= \sum_{\nu>0} |\varepsilon_\nu - \lambda_F|(a_\nu^+ a_\nu + a_{\overline{\nu}}^+ a_{\overline{\nu}}) - \frac{\Delta}{2} \sum_{\nu>0} (a_\nu^+ a_{\overline{\nu}}^+ + a_{\overline{\nu}} a_\nu),$$

(3.15)

where λ_F denotes the Fermi energy, Δ is the pairing gap parameter and is calculated following particle conservation [51] and $|\overline{\nu}\rangle$ is the time-reversal state of $|\nu\rangle$. The single-particle states $|\nu\rangle$ and the corresponding energies are obtained by diagonalizing the Hamiltonian H_{sp}. Similar to Refs. [39, 62], a Nilsson type Hamiltonian is employed,

$$H_{sp} = (\frac{p^2}{2m} + \frac{1}{2}m\omega_0\rho^2 - \frac{2}{3}\varepsilon_2\sqrt{\frac{4\pi}{3}}\hbar\omega_0\rho^2[\cos\gamma Y_2^0 + \frac{1}{\sqrt{2}}\sin\gamma(Y_2^2 + Y_2^{-2})]$$
$$- \kappa\hbar(\overline{\omega})\{2\vec{l}\cdot\vec{s} + \mu(\vec{l^2} - <\vec{l^2}>_N)\},$$

(3.16)

with ρ as the radius in a stretched coordinate system, ε_2 and γ are the usual Nilsson deformation parameters, $Y_2^{\pm2}$ and Y_2^0 are the second-order spherical harmonics, and κ and μ are the standard Nilsson parameters.

The single-particle states are written as;

$$a_\nu^+ |0\rangle = \sum_{Nlj\Omega} c_{Nlj\Omega}^\nu \Psi_{j\Omega}^{Nl},$$
$$a_{\overline{\nu}}^+ |0\rangle = \sum_{Nlj\Omega} (-1)^{j-\Omega} c_{Nlj\Omega}^\nu \Psi_{j-\Omega}^{Nl},$$

where Ω is the projection of the single-particle angular momentum operator j on the 3-axis and is restricted to the values ..., $-7/2$, $-3/2$, $+1/2$, $+5/2$, ... due to time reversal degeneracy [51].

The QTR model solutions can be obtained by diagonalizing the Hamiltonian (equation 3.13) in a complete basis space, which couples the inert core with the intrinsic wavefunctions of the valence nucleon. When the pairing interaction is ignored, a strong coupling basis can be constructed as;

$$|IMK\nu\rangle = \sqrt{\frac{1}{2}}\sqrt{\frac{2I+1}{8\pi^2}}[D^I_{M,K}a^+_\nu\,|0\rangle + (-1)^{I-K}D^I_{M,-K}a^+_{\overline{\nu}}\,|0\rangle], \qquad (3.17)$$

where $D^I_{M,K}$ denote the rotational D functions, which describe transformations between differently oriented coordinate systems. In the equation above, K assumes the values of ..., $-7/2$, $-3/2$, $+1/2$, $+5/2$, ... and the restriction on K is due to the fact that the basis states are symmetrized under the point group D_2, which requires the wave function to be invariant under a rotation of $180°$ around the body-fixed $\hat{1}$-axis, this leads to $K - \Omega$ being an even integer [40]. The matrix elements of H_{coll} and H_{int} can be evaluated in this basis (equation 3.17), and the diagonalization yields the eigenenergies and eigenstates of the QTR model Hamiltonian.

Pairing effects can be included in a straightforward manner in the QTR model by replacing the single-particle state $a^+_\nu\,|0\rangle$ in the basis state (equation 3.17) with BCS quasiparticle state $a^+_\nu\,|\tilde{0}\rangle$ to get a new expansion basis, where $|\tilde{0}\rangle$ is the BCS vacuum state. The quasiparticle operators α^+_ν are given by;

$$\begin{pmatrix} \alpha^+_\nu \\ \alpha_{\overline{\nu}} \end{pmatrix} = \begin{pmatrix} u_\nu & -v_\nu \\ v_\nu & u_\nu \end{pmatrix} \begin{pmatrix} a^+_\nu \\ a_{\overline{\nu}} \end{pmatrix}, \qquad (3.18)$$

where $u^2_\nu + v^2_\nu = 1$. In this new basis, the wavefunctions of the QTR Hamiltonian can be written as;

$$|IM\rangle = \sum_{K,\nu} C^{IK}_\nu\,|IMK\nu\rangle, \qquad (3.19)$$

here ν represents the quasiparticle states $\alpha^+_\nu\,|\tilde{0}\rangle$ instead of the single-particle states a^+_ν. The single-particle energies ε_ν must be replaced by the quasiparticle energies $\varepsilon'_\nu = \sqrt{(\varepsilon_\nu - \lambda_F)^2 + \Delta^2}$. The total Hamiltonian is expressed as;

$$H = H_{coll} + \sum_\nu \varepsilon'_\nu(\alpha^+_\nu\alpha_\nu + \alpha^+_{\overline{\nu}}\alpha_{\overline{\nu}}). \qquad (3.20)$$

The Hamiltonian in relation 3.14 possesses a particle-hole symmetry arising from the permutations of the intrinsic nuclear axes [51]. One consequence of this symmetry is that a particle coupled to a core with parameters $(\varepsilon_2, \gamma, \lambda_F)$ and a quasi-particle (hole) coupled to a core with parameters $(\varepsilon_2, 60° - \gamma, -\lambda_F)$ have exactly same energy spectrum.

3.3.2 QTR transitions probabilities

Electromagnetic transition probabilities are given as in Ref. [15], and have the general form;

$$B(O\lambda; I_i \to I_f) = \frac{1}{2I_i + 1} | \langle I_f | \Gamma(O\lambda) | I_i \rangle |^2, \tag{3.21}$$

where $\Gamma(O\lambda)$ is the electromagnetic operator, O stands for the type of operator (magnetic/electric), λ is the order of the transition, B is the reduced transition probability and $|I_i\rangle$ and $\langle I_f|$ stand for the initial state before the transition, and the Hermitian conjugate of the final state after the transition. The magnetic dipole $(\lambda = 1)$ moment operator is defined as;

$$\Gamma(M1) = g_R \vec{R} + \sum (g_l \vec{l} + g_s \vec{s}), \tag{3.22}$$

the sum is performed over the odd particle(s), $g_R = Z/A$ is the core g-factor, g_l and g_s are the single-particle orbital angular momentum and spin g-factors, respectively [36]. $\vec{R}$, $\vec{l}$ and $\vec{s}$ have their usual meanings. The electric quadruple $(\lambda = 2)$ operator is defined as;

$$\Gamma(E2) = \int d^3r[\rho(r)r^2 Y_2^\mu], \tag{3.23}$$

which splits into a dominant core component and an odd particle(s) component. The mixing ratio, $\delta_{E2/M1}$, is defined as;

$$\delta_{E2/M1} = \sqrt{0.7} \frac{\langle I| \Gamma(E2) |I - 1\rangle}{\langle I| \Gamma(M1) |I - 1\rangle} E_\gamma, \tag{3.24}$$

where $\Gamma(E2)$ and $\Gamma(M1)$ are the electric quadruple and magnetic dipole operators and E_γ is the γ-ray energy, which corresponds to the usual definition of

$$\delta^2_{E2/M1} = \frac{T(E2, I \rightarrow I-1)}{T(M1, I \rightarrow I-1)}, \tag{3.25}$$

where $T(E2)$ and $T(M1)$ are the corresponding electric and magnetic transition probabilities, respectively.

3.4   QTR Model Calculations

In this work the QTR model codes of Ragnarson and Semmes [39, 40], the three programs called GAMPN, ASYMO and PROBMO, in this particular sequence, were run one after the other. GAMPN calculates the single-particle eigenstates and matrix elements. ASYMO calculates the triaxial rotor states and couples them to the single particle states produced by GAMPN. The last program PROBMO uses the outputs of the previous two programs to calculate electromagnetic transition properties of the nucleus [66].

3.4.1   GAMPN

As stated previously, the program GAMPN calculates the single-particle states of the QTR model Hamiltonian. To run the calculations for a particular nucleus with a proton number Z and a mass number A, the program requires the quadruple deformation parameter ε_2, the axial asymmetry deformation γ and the hexade-capole deformation parameter ε_4, the valence nucleon(s) configuration, as well as the standard Nilsson parameters κ and μ. In these calculations the standard Nilsson parameters were adopted as in Ref. [11]. In general ε_2 and γ can be deduced from potential energy surface (PES) calculations or from experimental data. In addition, the program requires one to specify the single-particle configuration space of interest, that is to specify the orbitals near the Fermi level that will be included in the calculations.

The program outputs the single particle energies ε_ν, single-particle matrix element and the single-particle eigenstates $|\nu\rangle$, expanded in the basis $|NLJ\Omega\rangle$. For an

axially symmetric nuclear shape the output of the program is a pure Nilsson state, while for the asymmetric nuclear shape, the output is a mixture of basis states with the same parity but differing in occupation probabilities. This information is passed down to the next program ASYMO.

3.4.2 ASYMO

The program ASYMO couples the core rotation to the selected single-particle matrix elements and eigenstates $|\nu\rangle$ that are passed down from the program GAMPN and constructs the quasiparticle+triaxial rotor sates. A maximum of 15 single-particle states can be used in the calculations, typically a subset of the single-particle states lying close to the Fermi level are included. The inputs to ASYMO comprise information on these single-particle states (the same states as in GAMPN or, fewer). The moments of inertia of the core can be extracted from the experimental energy of the first 2^+ state [51] or can be parametrized by Harris parameters, which takes into account the spin dependence of the MoI's [30, 48].
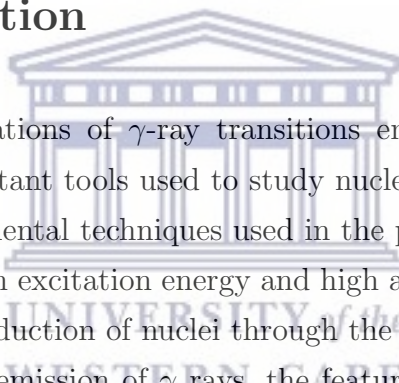
3.4.3 PROBMO

The results of GAMPN and ASYMO are passed down to the program PROBMO, which uses them to calculate the electromagnetic transition properties of all transitions that link all calculated nuclear states. That includes the $B(E2)$ and $B(M1)$ transition probabilities as well as the mixing ratios $\delta_{E2/M1}$ for the M1+E2 transitions and the quadruple moment for each state.

Chapter 4

Experimental Techniques

4.1 Introduction

Spectroscopic investigations of γ-ray transitions emitted by excited nuclei are among the most important tools used to study nuclear structure. This chapter is devoted to the experimental techniques used in the production and spectroscopic studies of nuclei at high excitation energy and high angular momenta. In particular it discusses the production of nuclei through the heavy-ion fusion evaporation (HIFE) reactions, the emission of γ rays, the features of high-purity germanium (HPGe) detectors and the AFRican Omnipurpose Detector for Innovative Techniques (AFRODITE) array, and the experimental data analyses used to build a level scheme and assign spin and parity to the nuclear states.

4.2 Heavy-Ion Fusion Evaporation

The heavy-ion fusion evaporation reaction mechanism involves the fusing of an incident projectile nucleus with a target nucleus, resulting in the formation of a compound system. The compound system can decay via several channels, for instance the compound nucleus can emit one or more particles such as protons (p), neutrons (n), and alpha (α) particles to produce a daughter nucleus in an excited state, which proceeds to decay via γ-ray emission. HIFE reactions provide the most efficient way of producing nuclei at high-spin states. Nuclear states with sufficient energy and cross section (reaction probability) can be reached with a

greater degree of selectivity [59]. HIFE reactions can occur if the incident projectile nucleus possess sufficient kinetic energy to overcome the Coulomb barrier of the target nucleus V_C, which can be approximated (in MeV) by [36];

$$V_C = \frac{Z_p Z_t}{4\pi\varepsilon_0 r} e^2,$$

(4.1)

with $r = 1.2(A_p^{\frac{1}{3}} + A_t^{\frac{1}{3}})$ fm. Here Z_p and A_p are the atomic number and the mass number of the incident projectile nucleus, and Z_t and A_t represent the atomic number and the mass number of the target nucleus.

A compound nucleus forms if the lifetime of the compound system is long enough (of the order of $\sim 10^{-20}$s). The probability of decay is solely dependent on the total energy imparted on the compound system, and is independent of the formation process [15]. Shortly after formation (of the order of $\sim 10^{-19}$s), the compound system resembles a hot, charged, rotating liquid drop and is highly unstable. It decays rapidly by evaporating particles away, which carry with them a large amount of energy, but very little angular momentum of $\sim 1\hbar$. Due to the Coulomb barrier, proton emission is hindered in the early stages of particle emissions from the compound system and neutron emission is the dominant decay path.

When particle emission is no longer a favorable decay path, a compound nucleus decays via the emission of electromagnetic radiation (γ rays). The first set of γ rays that are emitted are statistical, their strengths are dictated by random overlaps between the initial and final states wavefunctions, typically states that lie close to each other in energy and spin. These statistical γ decays are predominantly non-collective electric dipole $E1$ transitions that carry large amounts of excitation energy, but very little angular momentum.

4.3 Gamma Decay

A γ ray is a high energy photon that is emitted when a nucleus decays by electromagnetic radiation. The energy of the emitted γ ray contains information about the nucleus, for instance the energy of a γ ray, E_γ, is the energy difference between the initial nuclear state E_i and final nuclear state E_f; $E_\gamma = E_i - E_f$. The emission of a γ ray is dictated by conservation laws and quantum mechanical selection rules

for angular momentum and parity [36]. The multipole order of the emitted γ ray is given by:

$$|I_i - I_f| \leq L \leq I_i + I_f, \tag{4.2}$$

with I_i and I_f as the angular momenta of the initial and final state, respectively. L is the multipole order of the emitted γ ray. Stretched transitions have $L = |I_i - I_f|$ and unstretched transitions have $L > |I_i - I_f|$. Electric and magnetic multipoles of the same order have opposite parity, such that $\pi(EL) = (-1)^L$ for electric transitions and $\pi(ML) = (-1)^{(L+1)}$ for magnetic transitions. Transitions between states of the same parity are of the even multipole order for electric transitions and of the odd multipole order for magnetic transitions (M1, E2, M3, E4, ...), while transitions that involve parity change are of the odd multipole order for the electric transitions and of the even multipole order for magnetic transitions (E1, M2, E3, M4, ...). This information is summarized in Table 4.1. Transitions between two states with $I = 0$, cannot proceed through γ decay as a photon should carry a minimum $L = 1\hbar$ of angular momentum. Such a $0 \rightarrow 0$ transition proceeds through emission of internal conversion electrons.

L	1	2	3	4	5
$\pi_i \pi_f = -1$	$E1$	$M2$	$E3$	$M4$	$E5$
$\pi_i \pi_f = +1$	$M1$	$E2$	$M3$	$E4$	$M5$

TABLE 4.1: Multipolarity of a γ ray transition with multipole order L, linking initial and final states with parities of π_i and π_f, respectively.

4.4 Detection of Gamma Radiation

When a nucleus de-excites through γ decay, it is possible to measure the properties of the emitted γ ray when it interacts with the detector material. Germanium, which is a semiconductor, is the material of choice used by nuclear physicists to detect γ rays. Electron-hole pairs can form inside a semiconductor crystal when a γ ray with sufficient energy passes through the semiconductor material. If the crystal is placed between a pair of electrodes, it is possible to collect the created charge in the material. Germanium has an ionisation energy of ~ 2.9 eV, which allows greater power to resolve the energy of the emitted γ rays.

4.5 The AFRODITE Detector Array

The AFRODITE High Purity Germanium (HPGe) detector array at iThemba LABS is mounted on a rhombicuboctahedron frame with 16 detector positions [54]. The array consists of eight clover detectors, four positioned at 90° and four at 135°. The array also comprises of 7 low energy photon spectrometers (LEPS), two placed at 45°, three at 90° and two at 135°. The clover detectors are similar to those of EUROBALL III [67]. Each clover consists of four 50 x 70 mm HPGe crystals and eight clovers subtend a solid angle of $\sim 9.8\%$ of 4π. The detectors are suitable for measuring high-energy γ rays due to their large volume. The crystals are closely packed without any material between them which enables a good energy resolution for signals added from more than one crystal. The distance between the front face of the detector and the center of the AFRODITE array is 17.6 cm. Figure 4.1 shows the schematic diagram of the orientations of the clover detectors in the AFRODITE array. Recently the array was upgraded to comprise 17 clover detectors.

4.6 Data Analysis

Two experimental data sets are presented and discussed in this work. The first experiment was carried out at iThemba LABS (iTL), South Africa. The second one was performed at the Laborotori Nazionali di Legnaro (LNL), Italy. Both experimental data sets were analysed with the collaboration of Chinese, French and South African researchers and students [22]. The experimental data collected at LNL were analysed by the collaborators, but the theoretical calculations were performed as part of this work and presented in Chapter 6. Thus the experimental data on ^{131}Ba is also presented in Chapter 5. The second experiment performed at iTL collected data on ^{133}Ce. The preliminary analysis of these data, including calibrations and data sorting in matrices were carried out by our collaborators. However, the analysis of the γ-γ coincidence matrix and building and extending the level scheme of ^{133}Ce, as well as the theoretical calculations, were performed in this work. In this section the γ-coincidence analysis used to build the ^{133}Ce level scheme is discussed, while theoretical calculations are discussed in Chapter 6.
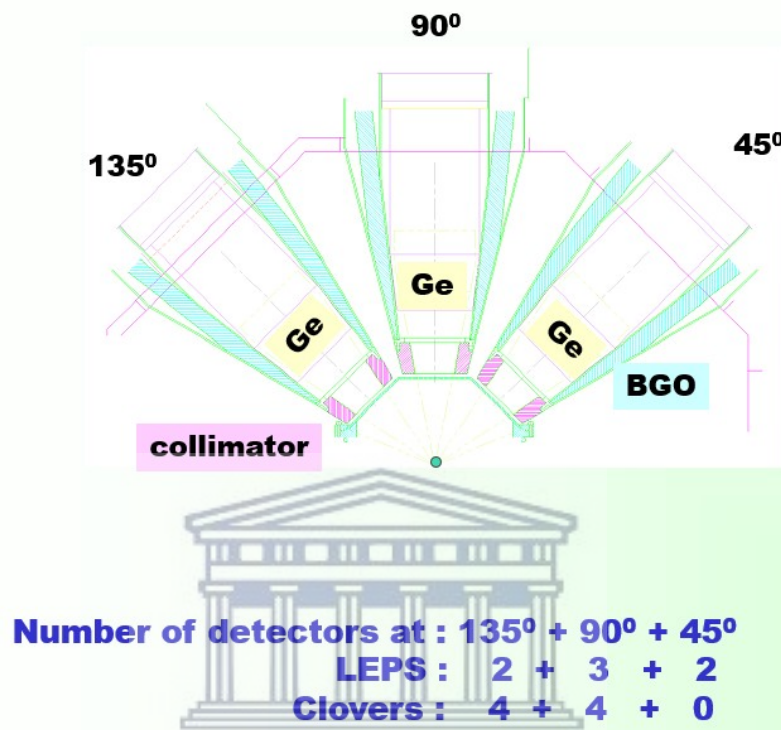
FIGURE 4.1: A schematic illustration of the detector orientation in the AFRODITE array. The corresponding number of LEPS and clover detectors placed at $45°, 90°$, and $135°$ is given at the bottom of the figure. Adapted from Ref. [41].

The AFRODITE detector array at iThemba LABS makes it possible to detect more than one γ ray simultaneously. By detecting γ rays simultaneously it is possible to construct a coincidence matrix, which represents the γ rays in coincidence. Figure 4.2 illustrates such a matrix. The γ rays of each event are arranged in pairs and each pair is counted in the coincidence matrix. For instance, γ rays a and b that were observed simultaneously and thus belong to one event are in coincidence and will be arranged as (a, b) and (b, a) pairs. Likewise, γ rays d and e are in coincidence and will be arranged as (d, e) and (e, d) pairs. The count numbers (the z axis in a coincidence matrix) will be increased by one at coordinated $x = a$ and $y = b$ when the pair (a, b) is counted, and similarly for all other pairs.

The spectra of coincident γ rays can be produced by such an arrangement of events in a coincident matrix. By gating on a single γ ray energy, it will show only those
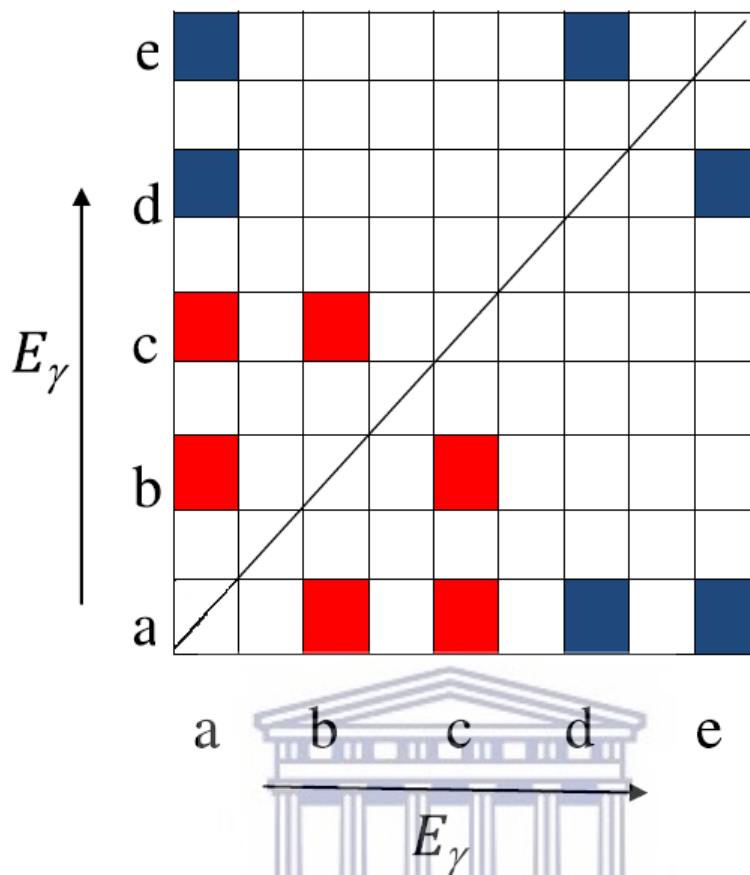
FIGURE 4.2: Schematic representation of a symmetric γ-γ matrix. γ ray a is in coincidence with all γ rays (b, c, d and e, shown by the red and blue squares). γ ray b is in coincidence only with γ rays a and c. Similarly, γ ray c is in coincident with a and b. γ ray d is coincident with a and e, etc...

γ rays that are in the decay path of the γ ray chosen as a gate. In such a way it becomes possible to construct this γ decay path. Gamma-ray emissions that proceed through the same path will be in coincidence, while those that do not belong to the same decay path will be anti-coincident to each other, that is, they will not "see" each other when gated on. To make the point more clear, in Figure 4.2, γ rays c and d are anti-coincident so when gating on either one, it is not possible to see the other. In Figure 4.3 a representative level scheme and sample gated spectra are shown for the symmetric matrix presented in Figure 4.2. It is possible to use the apparent strength of the detected γ rays in the gated spectra as transitions that are close to each other on the decay path see each other more strongly.

Coincident spectroscopy techniques such as γ-γ matrices, γ-γ-γ cubes, and so forth offer powerful tools to study the coincidence relationships of γ ray transitions,
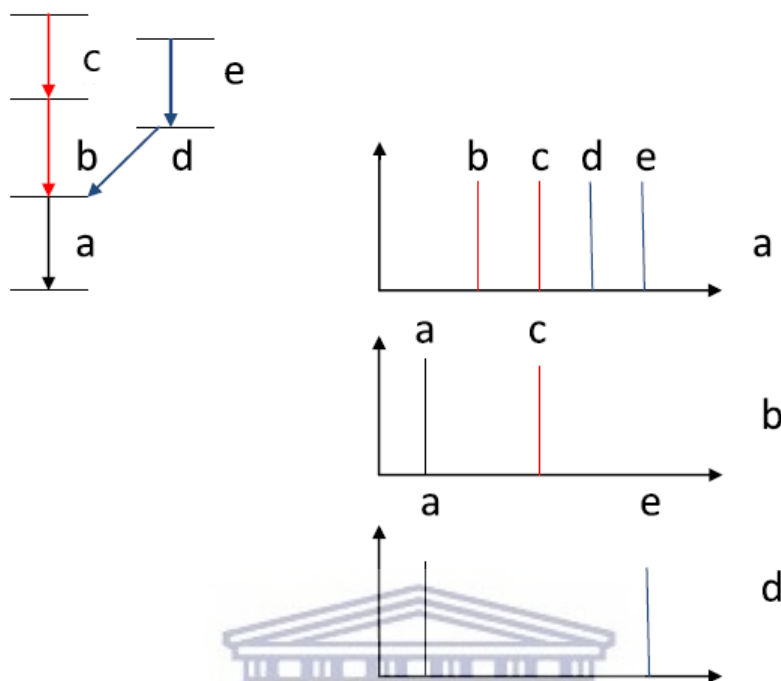
FIGURE 4.3: Schematic diagram showing coincidences between γ rays on the same decay path. The spectrum gated on transition a (top, right) shows all other transitions and indicates γ rays in coincidence with γ ray a. The spectrum gated on γ ray b (middle spectrum, right) shows only γ rays a and c as they are in coincident and belong to the same decay path. The spectrum gated on γ ray d shows only γ rays a and e as those are the transitions that are on the same decay path as d. The corresponding level scheme is drawn in the top left of the figure.

which in turn allow to build level schemes and give insight into the structure of the nucleus.

4.7 Correlations of Gamma Ray Transitions

4.7.1 Angular Distribution

Following HIFE reactions, the populated states are found to have their spins aligned perpendicular to the beam axis so that the emitted γ rays exhibit angular distributions depending upon their multipolarities and spins. Therefore, the

measurement of angular distributions provides information on the γ ray multipolarities. The normalized empirical γ ray intensities at each angle are fitted to the Legendre expansion:

$$W(\theta) = A_0[1 + a_2 P_2(\cos\theta) + a_4 P_4(\cos\theta)], \qquad (4.3)$$

where the $P_i(\cos\theta)$ are the Legendre polynomials. The a_2 and a_4 coefficients are characteristic to the transitions and their mixing ratios $\delta_{E2/M1}$:

$$\delta_{E2/M1} = \frac{\langle\psi_f|\,\hat{E}2\,|\psi_i\rangle}{\langle\psi_f|\,\hat{M}1\,|\psi_i\rangle}, \qquad (4.4)$$

where $|\psi_i\rangle$ and $\langle\psi_f|$ are the initial and final states of the transitions, respectively. $\hat{E}2$ and $\hat{M}1$ represent the electric quadruple and the magnetic dipole operators, respectively. The mixing ratios $\delta_{E2/M1}$ represent the ratios of the relative matrix elements for E2 and M1 components for transitions with mixed M1+E2 multipolarity (see Chapter 3, equation 3.24).

In practice in most fusion evaporation reaction experiments the nuclear spins are not fully aligned orthogonally with respect to the beam direction when the γ rays are emitted, which leads to some attenuation of the theoretical a_2 and a_4 coefficients. The attenuation is usually evaluated from the experimental data.

4.7.2 Angular Correlations

Angular correlation measurements involve the determination of coincidence intensities for a cascade of two γ ray transitions detected in coincidence by two detectors at different angles. The multipolarity of an emitted γ ray can be obtained using the Directional Correlation from Oriented states (DCO) ratios (R_{DCO}) [35, 37]. Such R_{DCO} values can be extracted by sorting the data from all detectors into an asymmetric γ-γ matrix, constructed in such a way that coincidence events detected by the detectors mounted at one angle (say 90°) are on one axis and those detected by a detector mounted at another angle (say 135°) are on the other axis. The R_{DCO} ratios are calculated using the γ ray intensities (I_γ) extracted from this matrix as:

$$R_{DCO} = \frac{I_{\gamma_1}^{135°}(\text{gated on } \gamma_2 \text{ at } 90°)}{I_{\gamma_1}^{90°}(\text{gated on } \gamma_2 \text{ at } 135°)}, \qquad (4.5)$$

where, $I_{\gamma_1}^{135°}$(gated on γ_2 at 90°) is the intensity of γ ray 1 at an angle of 135° as seen from a gate set on γ ray 2 at an angle of 90°, $I_{\gamma_1}^{90°}$(gated on γ_2 at 135°) is the intensity of γ ray 1 at an angle of 90° as seen from a gate set on γ ray 2 at an angle of 135°. For stretched quadrupole transitions, R_{DCO} values of ≈ 1 are obtained and for stretched pure dipole transitions R_{DCO} values are ≈ 0.5 when gating on stretched quadrupole transitions (that is γ_2 is E2). When we gate on a stretched dipole transitions R_{DCO} values of ≈ 1.0 are obtained for pure stretched dipoles while R_{DCO} values of ≈ 2.0 are obtained for stretched quadrupole transitions.

The data on ^{133}Ce, obtained with the AFRODITE array at iTL were analysed using angular distribution ratios,

$$R_{AD} = \frac{I_{\gamma_1}^{135°}(\text{gated on } \gamma_2 \text{ in all detectors})}{I_{\gamma_1}^{90°}(\text{gated on } \gamma_2 \text{ in all detectors})}, \qquad (4.6)$$

where $I_{\gamma_1}^{135°}$ is the intensity of γ ray 1 at an angle of 135°, when a gate is set on γ ray 2, where this γ ray is detected in all detectors. Similarly, $I_{\gamma_1}^{90°}$ corresponds to the intensity of γ ray 1 at an angle of 90°, when a gate is set on γ ray 2, where this γ ray is detected in all detectors.

The R_{AD} values do not depend on the multipolarity of the gated γ ray. For the AFRODITE array, the values obtained were $R_{AD} \sim 1.3$ for stretched quadrupole transitions and $R_{AD} \sim 0.8$ for stretched dipole transitions. The angular distribution analysis for ^{133}Ce and the spin and parity assignments for the new levels were carried out by our Chinese collaborators. The experimental results for ^{133}Ce and ^{131}Ba are presented in Chapter 5.

Chapter 5

Results

5.1 Introduction

Theoretical and experimental studies have shown that odd-N nuclei in the $A \approx 130$ region present one of the richest regions across the nuclear chart to study exotic nuclear phenomena across extended spin ranges. Nuclear triaxiality is one such phenomenon, which results when there is unequal density distribution across the three intrinsic nuclear axes.

This chapter presents the results obtained from two experiments. The first experiment was performed at the separated sector cyclotron of iThemba LABS in Cape Town, South Africa. The experiment populated high-spin states in ^{133}Ce. In the second experiment excited states in ^{131}Ba were populated via the fusion-evaporation ^{122}Sn$(^{13}$C, $4n)^{131}$Ba reaction at the XTU Tandem accelerator of Laborotori Nazionali di Legnaro, Italy.

The discussion of the results presented here is deferred to the next chapter.

5.2 ^{133}Ce Results

5.2.1 Experimental Details

The experiment was performed at the separated sector cyclotron of iThemba LABS in Cape Town, South Africa. High-spin states in ^{133}Ce were populated via the ^{125}Te(^{12}C, $4n$) ^{133}Ce at a beam energy of 57 MeV and an intensity of 5 pnA. The target was an isotopically enriched ^{125}Te metallic foil with a thickness of 2 mg/cm^2 on an 8 mg/cm^2 gold backing. The γ rays emitted by the excited residual nuclei have been measured with the AFRODITE array [54, 68] which consists of thirteen Compton-suppressed clover detectors arranged in three rings at 45° (one clover), 90° (eight clovers) and 135° (four clovers) with respect to the beam direction. A total of 2.8×10^{10} double- and 5.4×10^9 triple- and higher coincidence events were collected and sorted into two- and three-dimensional matrices for off-line analysis by our Chinese collaborators. However the data analysis is part of the present work, and it was carried out using the RADWARE software package [60].

5.2.2 ^{133}Ce Experimental Results

In this work the γ-γ coincidence matrix for the ^{133}Ce data were analysed. The deduced level scheme of ^{133}Ce is shown in Figure 5.1. The ordering of transitions within the proposed level scheme is based on γ-ray coincidences and their relative intensities. A number of new transition were identified. The experimental results will be discussed in two sections, one for the negative-parity bands and the other for the positive-parity bands.

5.2.2.1 The Negative-Parity Bands

Band 1

This negative-parity band structure has been previously identified in Refs. [7, 47, 52]. It constitutes the yrast band, a sequence of rotational states with the least amount of excitation energy for a given spin. It is built on the $I^\pi = 9/2^-$ state and extends up to the $I^\pi = 35/2^-$ state. Band 1 is based on a neutron hole in the $\nu h_{11/2}$ sub-shell that is coupled to a rotating triaxial core. The γ-ray energies,

relative intensities, spins and parities for the intraband transitions in Band 1 are listed in Table 5.1 and the corresponding level scheme is shown in Figure 5.1. No new transitions were found for Band 1.

Band 4

All intraband transitions of Band 4 are new and they constitute a new band, see Figure 5.1. The lowest observed state in the band is the $I^\pi = 13/2^-$ state and the band was extended up to $I^\pi = 27/2^-$. The new transitions were observed in the AFRODITE data. Six intraband E2 transitions with energies of 578, 608, 890, 871, 984, and 936 keV and six new intraband M1+E2 transitions with energies of 369, 209, 399, 490, 380, 604 and 332 keV were observed in this work. In addition, seven new interband $E2$ transitions with energies of 795, 993, 982, 955, 1090, 1083, and 1130 keV and eight interband M1+E2 transitions with energies of 625, 609, 583, 464, 709, 479, 797 and 484 keV were observed to feed into the yrast band (Band 1). Experimental information about the transitions in this band are presented in Table. 5.2. In Figure 5.2, spectra gated on the 608-, 871-, 936- and 795- keV transitions are presented to illustrate the transitions of Band 4.

See panel (b) of Figure 5.2, for instance when we gate on 871- keV we do not 'see' the 490- and 380- keV transitions, but we 'see' the 490- and 380- keV transitions if we gate on 936- keV they show, therefore, the 490- and 380- keV transitions are in coincidence with the 936- keV transition, but anti-coincidence with the 871- keV transition, so they are placed in parallel to the 871- keV transition.

Two transitions with very similar energies of 608 keV and 609 keV were placed in Band 4. When a gate is set on the 608 keV transition linking the $19/2^-$ and the $15/2^-$ states of Band 4, the resulting spectrum consists of all γ rays in coincidence with transitions in the energy range of 607 to 609 keV. Similarly, when a gate is set on the 609 keV transition linking the $15/2^-$ state of Band 4 with the $13/2^-$ state of Band 1, the resulting spectra consists of all γ rays in coincidence with transitions in the energy range of 608 to 610 keV. The pair (608, 609) is in coincident, that is they lie on the same decay path. Because the two transitions have an overlapping energy range when gated on such a pair is known as a 'doublet' transition. Panel (a) of Figure 5.2 shows the spectrum when a gate is set on the 608- keV transition. The 608- keV γ ray 'sees' the 609- keV transition. The 608 keV gate also 'sees' the 209- and 399- keV transitions in the gated spectra, this may appear puzzling, because the 209- and 399- keV transitions are placed in a parallel decay branch with the 608- keV transition in Figure 5.1. This becomes easy to understand when

one recalls that the 608- and 609- keV transitions are a doublet pair, thus the 209- and 399- keV transitions observed in this gate are in coincidence, not with the 608- keV transition, but rather the 609- keV transition.

The gate set on the 936- keV transition shown in panel (c) of Figure 5.2 'sees', all intraband transitions except the 332-, 604 and 984- keV transitions because the three transitions are in parallel. The 936 keV gate also 'sees' all linking interband transitions except for the 484-, 1130-, 797, and 1083 keV transitions, thus the gated spectra doesn't contain them because all they are anti-coincident.

The gate set on the 795- keV transition shown in panel (d) of Figure 5.2 'sees' all intraband transitions as this transition is one of the two transitions (the other is the 625 keV transition) that depopulates the band head state of $13/2^-$ which is linked to all the levels in Band 4. However, the spectra resulting from the 795 keV gate does not see any linking transitions between Band 4 and Band 1 because it is in parallel to all of them.

5.2.2.2 The Positive-Parity Bands

Band 2

The 844- and 782 keV transitions that form the positive-signature branch ($\alpha = +1/2$) of Band 2 were previously identified (as band Q1 in Ref. [7]). This sequence was found to decay to the 340- keV level with, $I^\pi = 7/2^+$, state via a dipole transition of 338 keV. In this work, this band structure is extended and a further four intraband E2 transitions with energies of 693, 819, 881 and 887 keV, forming the negative-signature branch ($\alpha = -1/2$) of Band 2, and four M1+E2 transitions with energies of 355, 426, 393, and 451 keV connecting the signature partners, were observed. In addition, an interband M1+E2 transition of 412 keV from Band 3 was also observed. Table 5.3 presents experimental details on the transitions of this band observed in this work.

In Figure 5.3, spectra gated on the 303-, 693-, 819- and 338- keV transitions are presented to illustrate the transitions of Band 2. The 303- keV transition is a known transition, and can be seen in panel (a) of Figure 5.3, it is in coincidence with all other γ-ray transitions in this band as it is the main channel to depopulate Band 2. The 693- keV transition is in coincident with the 303- keV transition,

however it is anti-coincident with the 338- and 355- keV transitions (see panel (b) of Figure 5.3) and is therefore placed in a parallel branch to the 338- and 355- keV γ rays. Similarly, the 393- and 426- keV transitions are in parallel branch to the 819- keV transition as these transitions are absent in the spectra gated on the 819- keV transition (see panel (c) of Figure 5.3).

Band 3

Band 3 is built on the $I^{\pi} = 1/2^+$ ground state. It was first reported in Ref [47]. The 318-, 498-, 630- and 726- keV transitions make up the positive-signature branch of the band, while the 436-, 631-, and 732- keV transitions form the negative-signature branch of Band 3. These two branches are interlinked by the 134-, 184-, 252-, 246-, 386- and 244- keV transitions. Two interband E2 transitions with energies of 712 and 768 keV feed into Band 2 [7]. A new 412- keV M1+E2 transition link the $I^{\pi} = 13/2^+$ state of Band 3 to the $I^{\pi} = 11/2^+$ state of Band 2. Table 5.4 presents the transitions observed.

FIGURE 5.1: A partial level scheme deduced for ^{133}Ce from this work. The width of the arrows is proportional to the relative intensity (normalized to the 170 keV transition). Energies are labelled in keV, new levels and new transitions are marked in red, while known transitions are shown in black.

$E_i(keV)$	I_i^π	$\rightarrow$	I_f^π	E_γ	I_γ	Multipolarity
207.4	$11/2^-$	$\rightarrow$	$9/2^-$	170.2	100(6)	M1+E2
592.1	$13/2^-$	$\rightarrow$	$11/2^-$	384.7	27.0(9)	M1+E2
592.1	$13/2^-$	$\rightarrow$	$9/2^-$	554.9	6.4(4)	E2
827.1	$15/2^-$	$\rightarrow$	$13/2^-$	235.0	12.1(4)	M1+E2
827.1	$15/2^-$	$\rightarrow$	$11/2^-$	619.7	34.7(11)	E2
1344.7	$17/2^-$	$\rightarrow$	$15/2^-$	517.6	9.4(4)	M1+E2
1344.7	$17/2^-$	$\rightarrow$	$13/2^-$	752.6	10.7(4)	E2
1590.3	$19/2^-$	$\rightarrow$	$17/2^-$	245.6	1.07(12)	M1+E2
1590.3	$19/2^-$	$\rightarrow$	$15/2^-$	763.2	15.2(5)	E2
2201.1	$21/2^-$	$\rightarrow$	$19/2^-$	610.8	3.33(22)	M1+E2
2201.1	$21/2^-$	$\rightarrow$	$17/2^-$	856.4	3.27(18)	E2
2486.6	$23/2^-$	$\rightarrow$	$21/2^-$	285.5	0.43(11)	M1+E2
2486.6	$23/2^-$	$\rightarrow$	$19/2^-$	896.3	6.65(25)	E2
3131.8	$25/2^-$	$\rightarrow$	$23/2^-$	645.2	0.28(10)	M1+E2
3131.8	$25/2^-$	$\rightarrow$	$21/2^-$	930.7	1.16(11)	E2
3434.0	$27/2^-$	$\rightarrow$	$25/2^-$	302.2	0.09(8)	M1+E2
3434.0	$27/2^-$	$\rightarrow$	$23/2^-$	947.4	2.45(19)	E2
4132.4	$29/2^-$	$\rightarrow$	$25/2^-$	1000.4	0.21(7)	E2
4406.4	$31/2^-$	$\rightarrow$	$27/2^-$	972.4	0.27(9)	E2
5401.8	$35/2^-$	$\rightarrow$	$31/2^-$	995.4	0.05(5)	E2

TABLE 5.1: Transitions in the yrast band (Band 1) of ^{133}Ce. Gamma-ray energies, relative intensities, spins and parities for the intraband M1+E2 and the E2 transitions assigned to Band 1 are presented where the intensities are given relative to that of the 170- keV transition. The error on the transition energies is within 0.3 keV for transitions with $I_\gamma \geq 10$ and up to 0.7 keV for transitions with $I_\gamma < 10$.

$E_i(keV)$	I_i^π	$\rightarrow$	I_f^π	E_γ	I_γ	Multipolarity
1200.8	$15/2^-$	$\rightarrow$	$13/2^-$	368.8	1.16(16)	M1+E2
1409.8	$17/2^-$	$\rightarrow$	$15/2^-$	209.0	5.5(6)	M1+E2
1409.8	$17/2^-$	$\rightarrow$	$13/2^-$	577.8	3.22(21)	E2
1809.1	$19/2^-$	$\rightarrow$	$17/2^-$	399.3	1.66(18)	M1+E2
1809.1	$19/2^-$	$\rightarrow$	$15/2^-$	608.3	1.89(18)	E2
2299.5	$21/2^-$	$\rightarrow$	$19/2^-$	490.4	0.80(16)	M1+E2
2299.5	$21/2^-$	$\rightarrow$	$17/2^-$	889.7	0.77(13)	E2
2679.9	$23/2^-$	$\rightarrow$	$21/2^-$	380.4	0.66(12)	M1+E2
2679.9	$23/2^-$	$\rightarrow$	$19/2^-$	870.8	1.95(18)	E2
3283.9	$25/2^-$	$\rightarrow$	$23/2^-$	604.0	2.12(20)	M1+E2
3283.9	$25/2^-$	$\rightarrow$	$21/2^-$	984.4	0.56(10)	E2
3616.2	$27/2^-$	$\rightarrow$	$25/2^-$	332.3	1.03(16)	M1+E2
3616.2	$27/2^-$	$\rightarrow$	$23/2^-$	936.3	0.49(11)	E2
832.0	$13/2^-$	$\rightarrow$	$11/2^-$	624.6	3.3(4)	M1+E2
832.0	$13/2^-$	$\rightarrow$	$9/2^-$	794.8	8.0(14)	E2
1200.8	$15/2^-$	$\rightarrow$	$13/2^-$	608.7	8.8(4)	M1+E2
1200.8	$15/2^-$	$\rightarrow$	$11/2^-$	993.4	0.01(3)	E2
1409.8	$17/2^-$	$\rightarrow$	$15/2^-$	582.7	3.53(25)	M1+E2
1809.1	$19/2^-$	$\rightarrow$	$17/2^-$	464.4	1.89(18)	M1+E2
1809.1	$19/2^-$	$\rightarrow$	$15/2^-$	982.0	1.95(17)	E2
2299.5	$21/2^-$	$\rightarrow$	$17/2^-$	954.8	6.08(24)	E2
2299.5	$21/2^-$	$\rightarrow$	$19/2^-$	709.2	1.26(14)	M1+E2
2679.9	$23/2^-$	$\rightarrow$	$21/2^-$	478.8	0.35(12)	M1+E2
2679.9	$23/2^-$	$\rightarrow$	$19/2^-$	1089.6	0.53(8)	E2
3283.9	$25/2^-$	$\rightarrow$	$23/2^-$	797.3	0.92(13)	M1+E2
3283.9	$25/2^-$	$\rightarrow$	$21/2^-$	1082.8	0.10(8)	E2
3616.2	$27/2^-$	$\rightarrow$	$25/2^-$	484.4	0.02(8)	M1+E2
3616.2	$27/2^-$	$\rightarrow$	$23/2^-$	1129.6	0.59(7)	E2

TABLE 5.2: Transitions in Band 4 of ^{133}Ce. Gamma-ray energies, relative intensities, spins and parities for the transitions assigned to Band 4 (where the intensities are given relative to the 170- keV transition of Band 1). The error on the transition energies is within 0.3 keV for transitions with energies below 1000 keV and up to 0.5 keV for transitions with energies above 1000 keV.
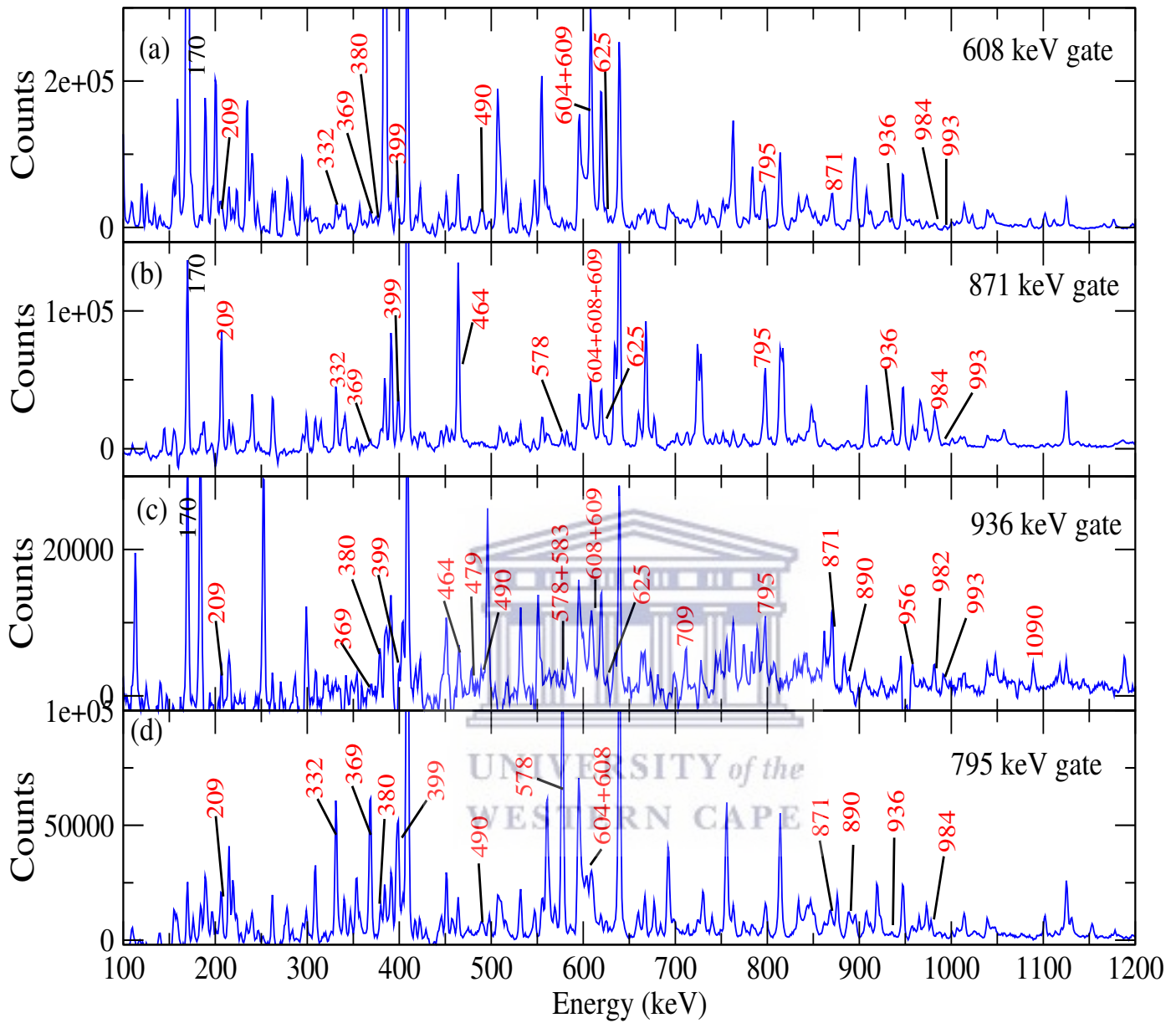
FIGURE 5.2: Spectra gated on (a) the 608- , (b) 870- , (c) 936- , and (d) 795-keV transitions of Band 4. New transitions and new levels are shown in red. Known transitions and levels are shown in black.

$E_i(keV)$	I_i^π	$\rightarrow$	I_f^π	E_γ	I_γ	Multipolarity
678.1	$9/2^+$	$\rightarrow$	$7/2^+$	337.8	2.10(13)	M1+E2
1033.4	$11/2^+$	$\rightarrow$	$9/2^+$	355.3	0.16(7)	M1+E2
1033.4	$11/2^+$	$\rightarrow$	$7/2^+$	693.1	1.32(13)	E2
1459.9	$13/2^+$	$\rightarrow$	$11/2^+$	426.4	0.15(9)	M1+E2
1459.9	$13/2^+$	$\rightarrow$	$9/2^+$	781.8	0.86(8)	E2
1852.7	$15/2^+$	$\rightarrow$	$13/2^+$	392.8	0.05(7)	M1+E2
1852.7	$15/2^+$	$\rightarrow$	$11/2^+$	819.3	0.76(9)	E2
2304.1	$17/2^+$	$\rightarrow$	$15/2^+$	451.4	0.27(10)	M1+E2
2304.1	$17/2^+$	$\rightarrow$	$13/2^+$	844.4	0.27(9)	E2
2733.4	$19/2^+$	$\rightarrow$	$15/2^+$	881.2	0.25(6)	E2
2739.5	$19/2^+$	$\rightarrow$	$15/2^+$	886.8	0.16(6)	E2
340	$7/2^+$	$\rightarrow$	$9/2^-$	303.1	–	E1

TABLE 5.3: Transitions in Band 2 of ^{133}Ce. Gamma-ray energies, relative intensities, spins and parities for the transitions assigned to Band 2 (where the intensities are given relative to the 170- keV transition of Band 1). The error on the transition energies is within 0.3 keV for transitions with energies below 1000 keV and up to 0.5 keV for transitions with energies above 1000 keV.
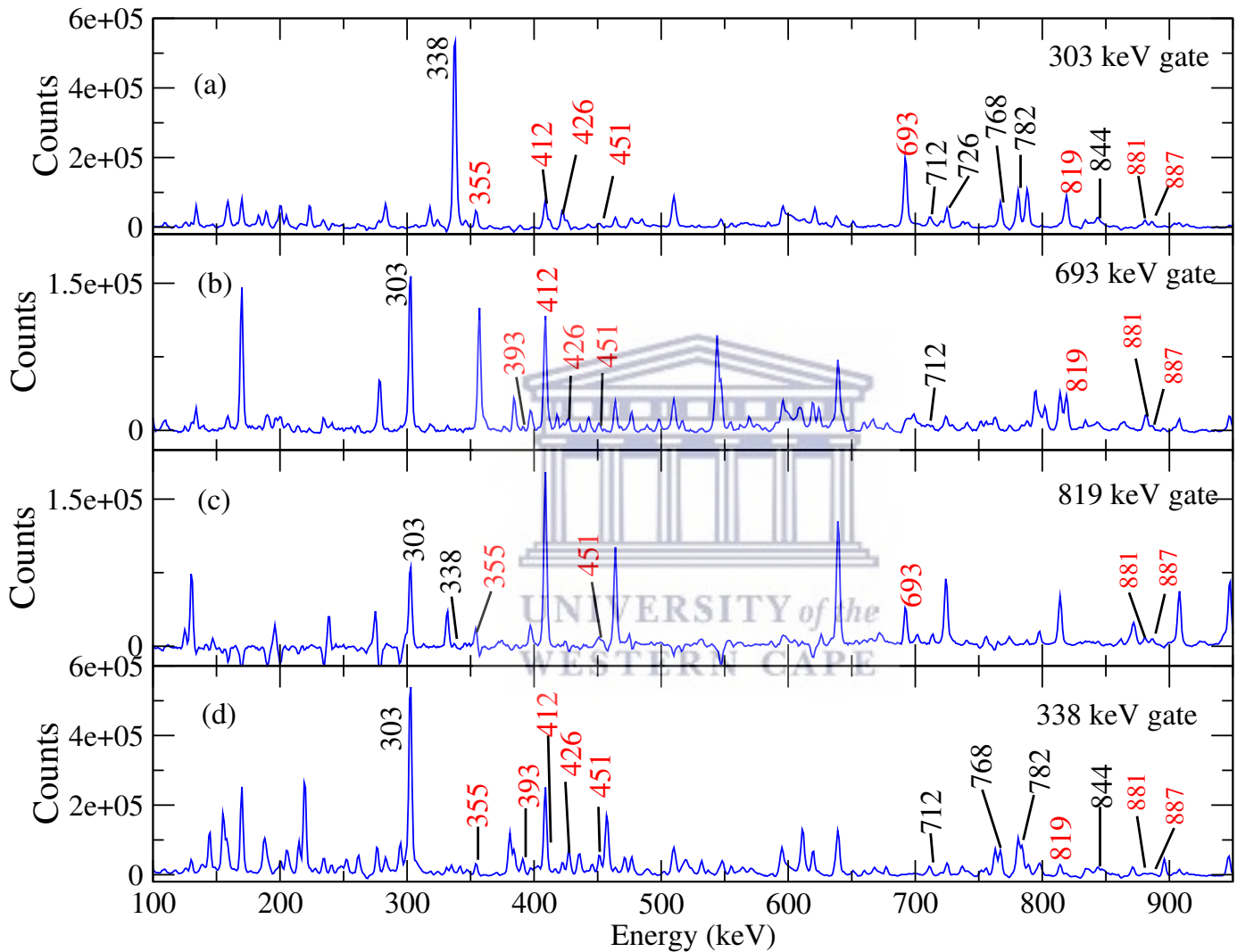
FIGURE 5.3: Spectra gated on (a) the 303-, (b) 693-, (c) 819-, and (d) 338-keV, illustrating the transitions of Band 2. New transitions and new levels are shown in red. Known transitions and levels are shown in black.

$E_i(keV)$	I_i^π	$\rightarrow$	I_f^π	E_γ	I_γ	Multipolarity
134.2	$3/2^+$	$\rightarrow$	$1/2^+$	134.2	–	M1+E2
318.3	$5/2^+$	$\rightarrow$	$3/2^+$	184.1	1.16(9)	M1+E2
318.3	$5/2^+$	$\rightarrow$	$1/2^+$	318.3	1.22(18)	E2
570.4	$7/2^+$	$\rightarrow$	$5/2^+$	252.1	0.38(8)	M1+E2
570.4	$7/2^+$	$\rightarrow$	$3/2^+$	436.2	2.03(14)	E2
815.9	$9/2^+$	$\rightarrow$	$7/2^+$	245.5	0.29(8)	M1+E2
815.9	$9/2^+$	$\rightarrow$	$5/2^+$	497.6	1.42(13)	E2
1201.4	$11/2^+$	$\rightarrow$	$9/2^+$	385.5	3.03(13)	M1+E2
1201.4	$11/2^+$	$\rightarrow$	$7/2^+$	631.0	1.41(12)	E2
1445.8	$13/2^+$	$\rightarrow$	$11/2^+$	244.4	0.11(7)	M1+E2
1445.8	$13/2^+$	$\rightarrow$	$9/2^+$	629.9	1.24(12)	E2
1932.9	$15/2^+$	$\rightarrow$	$11/2^+$	731.5	0.54(9)	E2
2171.9	$17/2^+$	$\rightarrow$	$13/2^+$	725.9	0.95(13)	E2
1445.8	$13/2^+$	$\rightarrow$	$9/2^+$	767.7	0.58(7)	E2
1445.8	$13/2^+$	$\rightarrow$	$11/2^+$	412.4	0.20(9)	M1+E2
2171.9	$17/2^+$	$\rightarrow$	$13/2^+$	711.0	0.25(8)	E2

TABLE 5.4: Transitions in Band 3 of ^{133}Ce. Gamma-ray energies, relative intensities, spins and parities for the transitions assigned to Band 3 (where the intensities are given relative to the 170- keV transition of Band 1). The error on transition energies is within 0.3 keV for transitions with energies below 1000 keV and up to 0.5 keV for transitions with energies above 1000 keV.

5.3 ^{131}Ba Results

5.3.1 Experimental Details

In this experiment excited states in ^{131}Ba were populated via the fusion-evaporation ^{122}Sn(^{13}C, $4n$)^{131}Ba reaction. A 65 MeV, ^{13}C beam with an intensity of 5 pnA was provided by the XTU Tandem accelerator at the Laborotori Nazionali di Legnaro, Italy. The target was a stack of two self-supported ^{122}Sn foils with a thickness of 0.5 mg/cm^2 each. The emitted γ-rays were detected with the GALILEO spectrometer, which consists of 25 Compton suppressed HPGe detectors, placed on four rings at 90° (10 detectors), 119° (5 detectors), 129° (5 detectors), and 152° (5 detectors). The EUCLIDES [8] silicon ball was used to detect charged particles, while neutrons were detected by the Neutron Wall array [43] in order to separate the different reaction channels.

Using the GALILEO data acquisition system [13], a total of 1.2×10^9 triple- or higher fold events were recorded. Doppler correction was performed on the γ spectra and the coincidence $\gamma\gamma\gamma$ events were sorted into a three dimensional cube. The data analysis of this experiment was carried out using the RADWARE and GASPware software packages by our Chinese collaborators. The experimental results are presented in this section. The theoretical calculations that were used to interpret these results are part of the present work and they are presented in Chapter 6.

5.3.2 ^{131}Ba Experimental Results

The deduced partial level scheme for ^{131}Ba is presented in Figure 5.4. The ordering of the transitions within the proposed level scheme is based on γ-ray coincidences. The arrow thickness represents the relative intensities of the γ rays. The experimental results will be discussed in two sections, one for the negative-parity yrast band (Band 1) and one for the two-positive parity bands (Band 2 and Band 3). A number of new transitions were identified and placed in the ^{131}Ba level scheme.
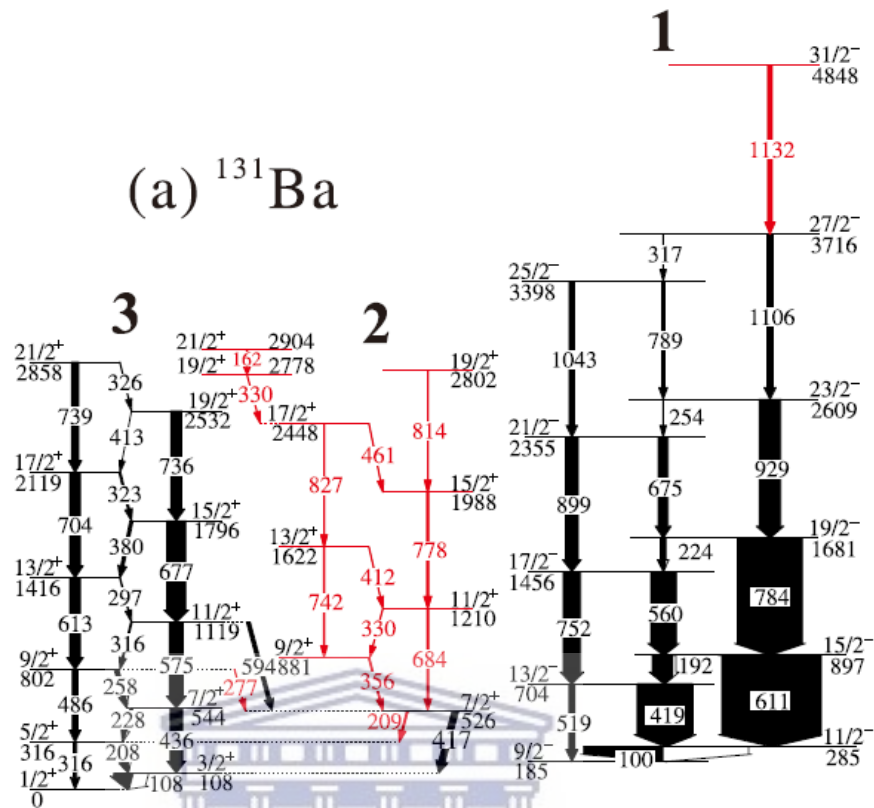
FIGURE 5.4: Partial level scheme of ^{131}Ba. The arrows indicate relative intensities. New transitions are marked in red.

5.3.2.1   The Negative-Parity Band

Band 1

This negative-parity band structure was observed in a prior work and is built on the $I^\pi = 9/2^-$ state [46]. States in this band were established up to the $I^\pi = 27/2^-$ state. In this experiment a new quadrupole transition feeding into the $I^\pi = 27/2^-$ with γ-ray energy of 1132 keV was found. The $\alpha = +1/2$ signature branch of this band consist of the 519-, 752-, 899- and 1043- keV quadrupole transitions. The 611-, 748-, 929-, 1106- and 1132-keV quadrupole transitions form the $\alpha = -1/2$ signature branch of the band. The 100-, 419-, 192-, 560-, 224-, 675-, 254-, 789- and 317- keV dipole transitions interlink the two signature branches of Band 1.

5.3.2.2   The Positive-Parity Bands

Band 2

Band 2 is a new band, deduced in the experiment. The band is built on the $I^\pi = 7/2^+$ state with an excitation energy of 526 keV and was established in prior works [46, 69]. This assignment was proposed based on the quadrupole character of the 417- keV transition to the $I^\pi = 3/2^+$ state of the ground-state band (Band 3). This structure consists of seven levels, three quadrupole transitions with γ-ray energies of 684, 778, and 814 keV were found forming the $\alpha = -1/2$ signature branch. The $\alpha = +1/2$ signature branch of the band consists of the 742 and 827- keV transitions. The two signature branches are connected by the 356-, 330-, 412- and 461- keV dipole transitions. In addition, Band 2 is connected to a new structure, for which two new levels were deduced, the $I^\pi = 21/2^+$ state at 2904 keV and the $I^\pi = 19/2^+$ state at 2778 keV. The $I^\pi = 19/2^+$ state decays towards Band 2 via a 330- keV dipole transition into the $I^\pi = 17/2^+$ state.

Band 3
Similar to Band 3 of ^{133}Ce, this band is built on the $I^\pi = 1/2^+$ ground state and extends up to the $I^\pi = 21/2^+$ state. It has been previously observed in Refs. [46, 69]. A new 277-keV dipole transition from the $I^\pi = 9/2^+$ state of Band 3 was observed to decay to the $I^\pi = 7/2^+$ state of Band 2.

Chapter 6

Discussion

6.1 Introduction

Odd-A neutron-deficient nuclei in the A $\sim$ 130 region exhibit a variety of nuclear shapes. Theoretical and experimental studies have shown that nuclei in this region can adopt prolate, oblate or triaxial nuclear shapes [26]. The neutron and proton Fermi surfaces lie between the 50 and 82 shell closures. Between these shell closures, there is only one unique-parity subshell, the $h_{11/2}$ subshell, whereas four positive-parity subshells are available for positive-parity states, namely, $d_{5/2}$, $g_{7/2}$, $d_{3/2}$ and $s_{1/2}$. Observables in odd-N nuclei in the A $\sim$ 130 region provide information about the nuclear shape, since observables such as the features of the observed rotational bands, including band-head spin, moment of inertia, and signature splitting, depend sensitively on the nuclear deformation.

The focus of the present investigation is two-fold, in the first part, the relationship between triaxiality and signature splitting is investigated in the newly observed positive-parity $g_{7/2}[404]7/2^+$ band structures of ^{131}Ba and ^{133}Ce (Band 2 in Section 5.3 and Band 2 in Section 5.2, respectively). In the second part of the investigation a new excited band in ^{133}Ce, built on the $I = 13/2^-$ state (Band 4 in Section 5.2), is investigated. The observed properties of these bands are compared to QTR model calculations.

6.2 Part I: Interpretation of the $g_{7/2}[404]7/2^+$ structures in ^{133}Ce and ^{131}Ba

The observed low-lying excited band structures in the $N = 75$ isotones of ^{133}Ce and ^{131}Ba built on the $I^\pi = 7/2^+$ states correspond to one-quasiparticle configurations. These bands exhibit a remarkable similarity, for instance they both show intense intraband M1+E2 transitions which suggests that they have a strong coupling nature. The observed values of the signature splitting, measured by the energy staggering parameter S(I) (see equation 2.37 in Section 2.5) in both bands are larger than expected for a high-K band (where $K \neq 1/2$). Inspecting the available intrinsic Nilsson orbitals for neutrons between the $N = 50$ and $N = 82$ shell closures, four positive-parity sub-shells are identified, the $d_{5/2}$, $g_{7/2}$, $s_{1/2}$, $d_{3/2}$ subshells (see Figure 2.5). From the $g_{7/2}$ sub-shell the available Nilsson orbitals are the $g_{7/2}[420]1/2^+$, $g_{7/2}[411]3/2^+$, $g_{7/2}[402]5/2^+$, and $g_{7/2}[404]7/2^+$ orbitals. The $s_{1/2}$ subshell consists of one Nilsson orbital, $s_{1/2}[411]1/2^+$. The $d_{3/2}$ subshell consists of the Nilsson orbitals $d_{3/2}[400]1/2^+$ and $d_{3/2}[402]3/2^+$. Among these Nilsson orbitals only the $\nu g_{7/2}[404]7/2^+$ configuration is consistent with the observed bandhead state of $I^\pi = 7/2^+$. This orbital is also very close to the Fermi level.

It is known that in the $N = 73$ isotonic chain of ^{129}Ba, ^{131}Ce, and ^{133}Nd, the $\nu g_{7/2}[404]7/2^+$ configuration is responsible for bands built on the $I^\pi = 7/2^+$ state [3, 9, 25]. It becomes natural to suspect the existence of similar structures in the $N = 75$ isotones. However the observed bands in ^{133}Ce and ^{131}Ba exhibit significant signature staggering, which is not expected for a high-K configuration, such as $g_{7/2}[404]7/2^+$.

On the other hand, rigid triaxial and γ-soft nuclear shapes can induce large signature splitting. Therefore the signature splitting can be possibly understood as a direct consequence of triaxial deformation. The energy staggering parameter, $S(I)$, is a useful measure to describe the extent of signature splitting and can be extracted as a function of nuclear spin. In addition to triaxiality, energy staggering can also be caused by $K = 1/2$ orbitals (see Section 2.5).

6.2.1 Signature splitting in Band 2 of ^{133}Ce

To gain insight on the influence of the triaxiality parameter γ on the signature splitting, calculations were performed using the QTR model (see Sections. 3.3 and 3.4). The calculated energy spectra $E(I)$ and the signature splitting $S(I)$ are compared with the experimental results. For the calculations, the included configuration space span ten positive-parity orbitals lying close to the Fermi level. Due to triaxiality, the QTR model single-particle orbital denoted by $|\nu\rangle$ does not correspond to a pure Nilsson orbital and is rather expressed as a linear combination of orbitals with the same parity. In the case of axial symmetry, $|\nu\rangle$ does correspond to a pure Nilsson orbital.

I^π	configuration	ε_2	γ	ε_4
^{131}Ba				
$\frac{7}{2}^+$	$\nu[404]7/2^+$	0.170	9°	0.003
^{133}Ce				
$\frac{7}{2}^+$	$\nu[404]7/2^+$	0.185	10°	0.1
$\frac{9}{2}^-$	$\nu[514]9/2^-$	0.183	21°	0.015
$\frac{13}{2}^-$	$\nu[514]9/2^-$	0.183	21°	0.015

TABLE 6.1: Deformation parameters obtained from potential energy surface (PES) calculations [22].

Constrained potential energy surface (PES) calculations [22] done within the collaboration, suggest a quadruple deformation of $\varepsilon_2 = 0.185$ and a hexadecapole deformation of $\varepsilon_4 = 0.01$ for the $\nu g_{7/2}$ orbital with a projection on the long axis of $7/2^+$ in ^{133}Ce (see Table 6.1). Information on the positive-parity single-particle neutron orbitals near the Fermi level, calculated with the QTR model is presented in Table 6.2. They are calculated with $(\varepsilon_2, \gamma) = (0.185, 15°)$. The QTR model orbital $|\nu\rangle$ is expanded in the basis $|NLJ\Omega\rangle$, where N is the major oscillator shell number, L is the orbital angular momentum number, J is the total single-particle angular momentum number, and Ω is the projection of J on a chosen intrinsic axis (the long axis is the chosen axis of projection in this work, therefore Ω and Ω_l are used interchangeably throughout this work). The corresponding approximate Nilsson quantum numbers are also listed in the table. The orbitals $|\nu\rangle$ couple to the even-even triaxial core rotation to produce QTR model states.

The MoI's of the core were assumed to follow the irrotational-flow dependence with respect to the γ deformation [48]. Harris parametrization for the MoI of the core was used with $\mathcal{J}_0 = 10.4\ \hbar^2\text{MeV}^{-1}$ and $\mathcal{J}_1 = 35.7\ \hbar^4\text{MeV}^{-3}$ [48]. The calculations place the Fermi surface at $\lambda_F = 50.6$ MeV for the deformation parameters listed in Table 6.1 and $\gamma = 15°$.

		Single-particle information	
$|\boldsymbol{\nu}\rangle$	$\Omega^\pi[Nn_z\Lambda]$	ε(MeV)	main components in terms of $|\boldsymbol{NLJ\Omega}\rangle$
$|14\rangle$	$1/2^+[420]$	5.4502	$-(0.687)\left|4g_{\frac{7}{2}}\frac{1}{2}\right\rangle-(0.397)\left|4g_{\frac{7}{2}}-\frac{3}{2}\right\rangle$
			$-(0.357)\left|4d_{\frac{5}{2}}\frac{1}{2}\right\rangle$
$|15\rangle$	$3/2^+[422]$	5.5149	$(0.567)\left|4d_{\frac{5}{2}}-\frac{3}{2}\right\rangle+(0.512)\left|4g_{\frac{7}{2}}-\frac{3}{2}\right\rangle$
			$-(0.424)\left|4g_{\frac{7}{2}}\frac{1}{2}\right\rangle$
$|16\rangle$	$3/2^+[411]$	5.6071	$-(0.696)\left|4g_{\frac{7}{2}}-\frac{3}{2}\right\rangle+(0.683)\left|4d_{\frac{5}{2}}-\frac{3}{2}\right\rangle$
			$+(0.209)\left|4d_{\frac{3}{2}}\frac{1}{2}\right\rangle$
$|17\rangle$	$5/2^+[402]$	5.6733	$(0.833)\left|4g_{\frac{7}{2}}\frac{5}{2}\right\rangle-(0.426)\left|4d_{\frac{5}{2}}\frac{5}{2}\right\rangle$
			$-(0.171)\left|4d_{\frac{3}{2}}\frac{1}{2}\right\rangle$
$|18\rangle$	$5/2^+[413]$	5.8046	$(0.842)\left|4d_{\frac{5}{2}}\frac{5}{2}\right\rangle+(0.457)\left|4g_{\frac{7}{2}}\frac{5}{2}\right\rangle$
			$-(0.186)\left|4s_{\frac{1}{2}}\frac{1}{2}\right\rangle$
$|19\rangle$	$1/2^+[400]$	5.8239	$-(0.616)\left|4d_{\frac{3}{2}}\frac{1}{2}\right\rangle+(0.437)\left|4s_{\frac{1}{2}}\frac{1}{2}\right\rangle$
			$+(0.404)\left|4d_{\frac{7}{2}}\frac{1}{2}\right\rangle$
$|\mathbf{20}\rangle$	$\mathbf{7/2^+[404]}$	**5.8985**	$-(\mathbf{0.957})\left|4g_{\frac{7}{2}}-\frac{7}{2}\right\rangle+(0.261)\left|4d_{\frac{3}{2}}-\frac{3}{2}\right\rangle$
			$+(0.07)\left|4g_{\frac{9}{2}}-\frac{7}{2}\right\rangle$
$|21\rangle$	$1/2^+[411]$	6.0517	$(0.572)\left|4s_{\frac{1}{2}}\frac{1}{2}\right\rangle+(0.553)\left|4d_{\frac{3}{2}}-\frac{3}{2}\right\rangle$
			$+(0.429)\left|4d_{\frac{3}{2}}\frac{1}{2}\right\rangle$
$|22\rangle$	$3/2^+[402]$	6.1829	$-(0.728)\left|4d_{\frac{3}{2}}-\frac{3}{2}\right\rangle+(0.446)\left|4s_{\frac{1}{2}}\frac{1}{2}\right\rangle$
			$+(0.337)\left|4d_{\frac{3}{2}}\frac{1}{2}\right\rangle$
$|23\rangle$	$1/2^+[660]$	6.4922	$(0.784)\left|6i_{\frac{13}{2}}\frac{1}{2}\right\rangle+(0.485)\left|6i_{\frac{13}{2}}-\frac{3}{2}\right\rangle$
			$+(0.258)\left|6g_{\frac{9}{2}}\frac{1}{2}\right\rangle$

TABLE 6.2: QTR model neutron single-particle orbitals, $|\boldsymbol{\nu}\rangle$ with positive-parity lying close to the Fermi level for ^{133}Ce. The orbitals are expanded in the $|\boldsymbol{NLJ\Omega}\rangle$ basis. The corresponding single-particle energies (ε) and the corresponding Nilsson orbitals with largest contributions are also included for the deformation parameters listed in Table 6.1 and $\gamma = 15°$.

Firstly, the Harris parameters for the MoI were chosen to reproduce the excitation energies $E(I)$ for the axially symmetric case ($\gamma = 0°$). Then triaxiality was introduced, for $\gamma = 10°$, $15°$, and $20°$. The calculated energy spectra for the $\nu g_{7/2}[404]7/2^+$ structure for $\gamma = 0°$ and $\gamma = 10°$ in comparison with experimental data are shown in panels (a) and (b) of Figure 6.1. At these γ values the calculated energy spectra and the experimentally measured values agree very well for low spins, while the calculations slightly underestimate the data at medium and high spins. Above the $I = 13/2^+$ level the extracted values of $S(I)$ show considerable staggering very similar to the experimental values for both the axially symmetric case and for $\gamma = 10°$ (see panels (c) and (d) in Figure 6.1).

To understand the impact of triaxiality, calculations with larger γ-values of $\gamma = 15°$ and $\gamma = 20°$ were carried out. Panels (a) and (b) of Figure 6.2 show a comparison between the QTR model excitation energies at $\gamma = 15°$ and $\gamma = 20°$ and the experimental values, respectively. There is an excellent agreement between the theory and the experimental energy spectra for $\gamma = 15°$ across the whole spin range. The agreement is even better than that obtained with $\gamma = 0°$ and $\gamma = 10°$ (see Figure 6.1). When $\gamma = 20°$, the excitation energies of the $15/2^+$ and the $19/2^+$ are not so well reproduced by the QTR model. The energy staggering, $S(I)$, extracted from the QTR model for $\gamma = 15°$ and $\gamma = 20°$ is compared to the experimental values in panels (c) and (d) of Figure 6.2, respectively. It can immediately be deduced that a γ deformation of $\gamma = 15°$ reproduces the experimentally observed staggering very well. When $\gamma = 20°$ the amplitude of the calculated $S(I)$ becomes larger than the experimental values. Thus the calculations support a moderate triaxial deformation, consistent with a γ deformation in the range of $0° \leq \gamma \leq 15°$.

The model wave functions provide further insights on the composition and nature of the states of Band 2. When the orbital $|\nu\rangle$ is coupled to a triaxial core, each state I^π is a mixture of different $|NLJ\Omega\rangle$ basis orbitals that have various projections on the chosen nuclear axis, with some having a projection of $\Omega = 1/2$. This means that both the projection of the total angular momentum $\vec{I}$, K, and the projection of the single-particle angular momentum $\vec{j}$, Ω, are not good quantum numbers. However, it was shown that usually K and Ω are approximately good quantum numbers for a high-K band, in particular near the band head and when $\gamma \approx 30°$[51].

Table 6.3 lists the three dominant components of the basis functions that contribute to each state. The basis functions are denoted as $(K_l, |\nu\rangle)$, for short. For reasons discussed in Section 3.2.1, the axis of projection in this work is the long axis, that is $K = K_l$ throughout the remainder of the text.
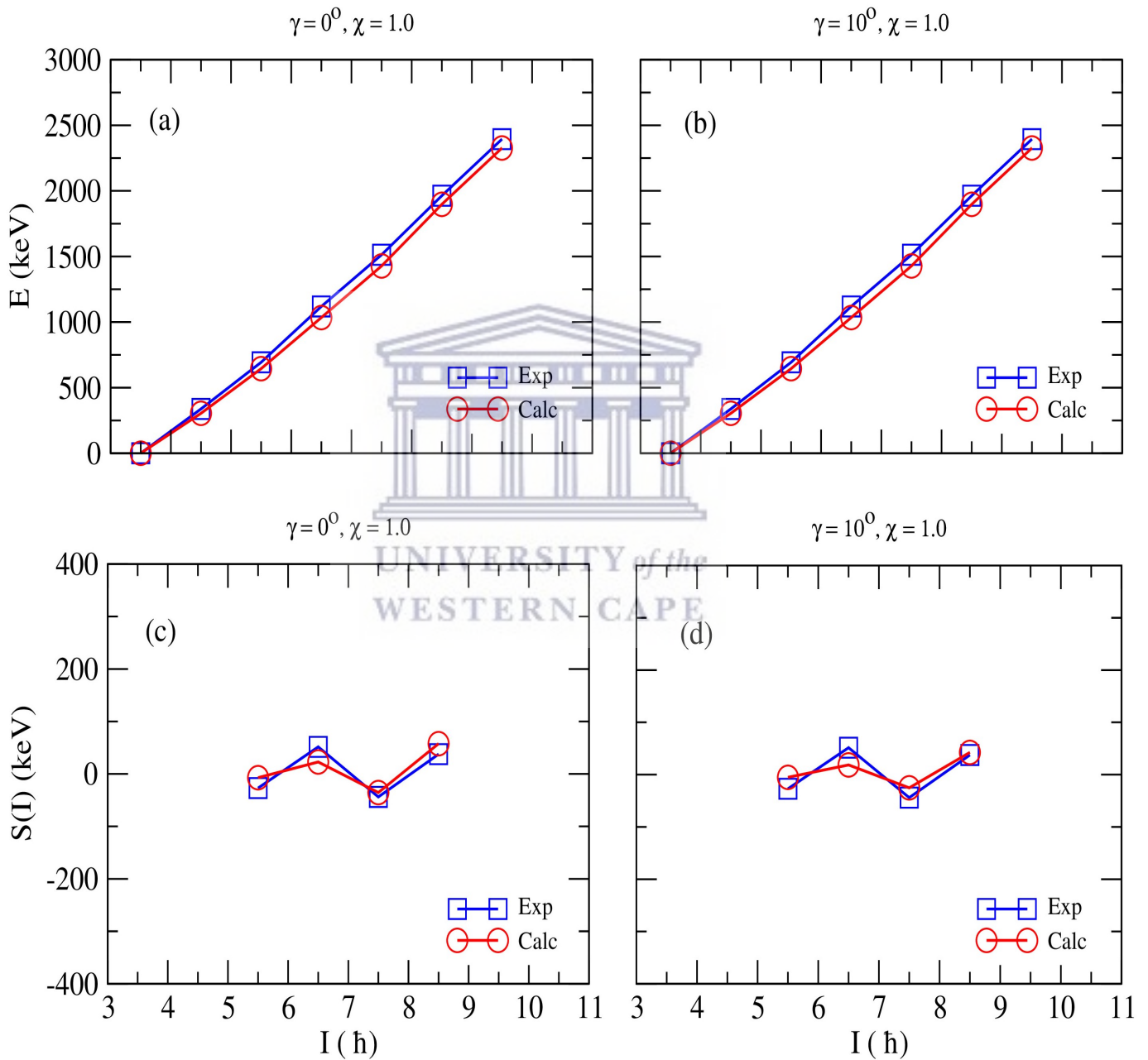
FIGURE 6.1: The energy spectra $E(I)$ and signature splitting $S(I)$ for Band 2 of ^{133}Ce at $\gamma = 0°$ and $10°$, and Coriolis interaction (χ) at full strength.
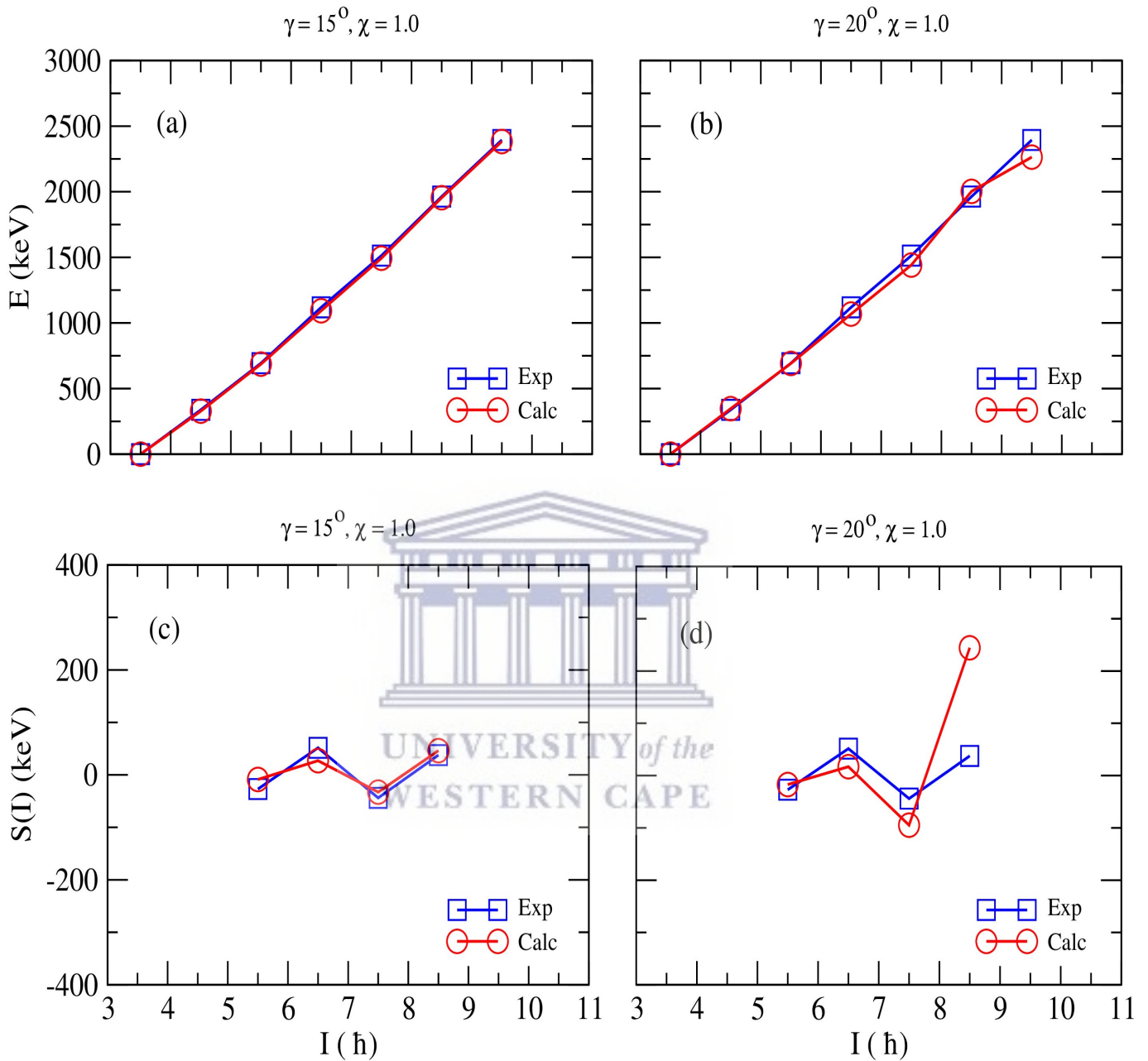
FIGURE 6.2: The energy spectra $E(I)$ and signature splitting $S(I)$ for Band 2 of ^{133}Ce at $\gamma = 15°$ and $20°$, and Coriolis interaction (χ) at full strength.

The information on the wave functions of the states of Band 2 is visualized in Figure 6.3. Each grouping of columns represents the wave function of the state. The orbitals $|\nu\rangle$ that are present are labelled from left to right on the x-axis of the plot by (#). The y-axis represents the value of K_l, the projection of the total angular momentum on the long nuclear axis. The different K_l values are also shown in different colors, see the legends of the figure. The z-axis (height of each column)

I^π	expansion in the basis $\lvert \boldsymbol{K_l \nu} \rangle$
$\frac{7}{2}^+$	$(0.947)\left\lvert -\frac{7}{2}20\right\rangle - (0.205)\left\lvert -\frac{7}{2}21\right\rangle - (0.135)\left\lvert \frac{5}{2}18\right\rangle$
$\frac{9}{2}^+$	$(0.982)\left\lvert -\frac{7}{2}20\right\rangle - (0.202)\left\lvert -\frac{7}{2}21\right\rangle + (0.185)\left\lvert \frac{5}{2}18\right\rangle$
$\frac{11}{2}^+$	$(0.878)\left\lvert -\frac{7}{2}20\right\rangle + (0.218)\left\lvert \frac{5}{2}18\right\rangle + (0.199)\left\lvert -\frac{7}{2}21\right\rangle$
$\frac{13}{2}^+$	$(0.869)\left\lvert -\frac{7}{2}20\right\rangle + (0.239)\left\lvert \frac{5}{2}18\right\rangle - (0.216)\left\lvert \frac{5}{2}17\right\rangle$
$\frac{15}{2}^+$	$(0.772)\left\lvert -\frac{7}{2}20\right\rangle - (0.247)\left\lvert \frac{5}{2}18\right\rangle - (0.226)\left\lvert \frac{5}{2}17\right\rangle$
$\frac{17}{2}^+$	$(0.767)\left\lvert -\frac{7}{2}20\right\rangle + (0.254)\left\lvert \frac{5}{2}18\right\rangle + (0.246)\left\lvert -\frac{3}{2}21\right\rangle$
$\frac{19}{2}^+$	$(0.672)\left\lvert -\frac{7}{2}20\right\rangle + (0.263)\left\lvert \frac{1}{2}19\right\rangle - (0.252)\left\lvert \frac{5}{2}18\right\rangle$

TABLE 6.3: The amplitude and main components of the QTR model wave functions for states in Band 2 of ^{133}Ce expanded in a strong coupling basis $\lvert K_l\nu \rangle$. The contribution of each $\lvert K_l\nu \rangle$ is the square of the amplitude.

represents the contribution of $(K_l, \lvert \nu \rangle)$ to the state wave function. For instance, the band head state, $I^\pi = 7/2^+$, has the composition $\sim 89\% \, (K_l, \lvert \nu \rangle) = (7/2, \lvert 20 \rangle)$, shown as the tallest yellow column in Figure 6.3. It corresponds to orbital $\lvert 20 \rangle$ with a dominant $g_{7/2}[404]7/2$ nature and $K_l = \Omega_l = 7/2$, see Table 6.3. Thus, the bandhead state has a dominant $(K_l, \Omega_l) = (7/2, 7/2)$ nature. This illustrates the strong coupling nature of the band at the bandhead, where the single-particle angular momentum of the $g_{7/2}$ neutron is mostly aligned along the long axis, because $\Omega_l = 7/2$, while the total angular momentum of $I = 7/2$ is also aligned along the long axis because $K_l = 7/2$. The rotational angular momentum along the long axis for the band head state is therefore negligible.

As the spin increases, the contribution from orbital $\lvert 20 \rangle$ with $\Omega_l = 7/2$, that is the contribution of the configuration $(K_l, \Omega_l) = (7/2, 7/2)$ to the total wavefunction, begins to decrease, with the lowest contribution ($\sim 45\%$) for the, $I^\pi = 19/2^+$ state. However it remains the dominant contributor to the wave functions of the states in the band, see the tall yellow column for each state in Figure 6.3. This is in line with the observed nature of strongly coupled bands, where the higher-spin states are generated by rotation, that is orthogonal to the direction of the single-particle angular momentum. In the present case the dominant rotation is around the intermediate axis, because it has largest MoI, as such rotation around this axis needs minimum energy.

The gradual decrease in contribution of the $(K_l, \Omega_l) = (7/2, 7/2)$ component can be understood as resulting from the particle-core coupling and the corresponding Coriolis interaction. The $\lvert 19 \rangle$ and $\lvert 21 \rangle$ orbitals, which are associated mostly with $s_{1/2}$ and $d_{3/2}$ components, see Table 6.2, come close to the Fermi level, and because
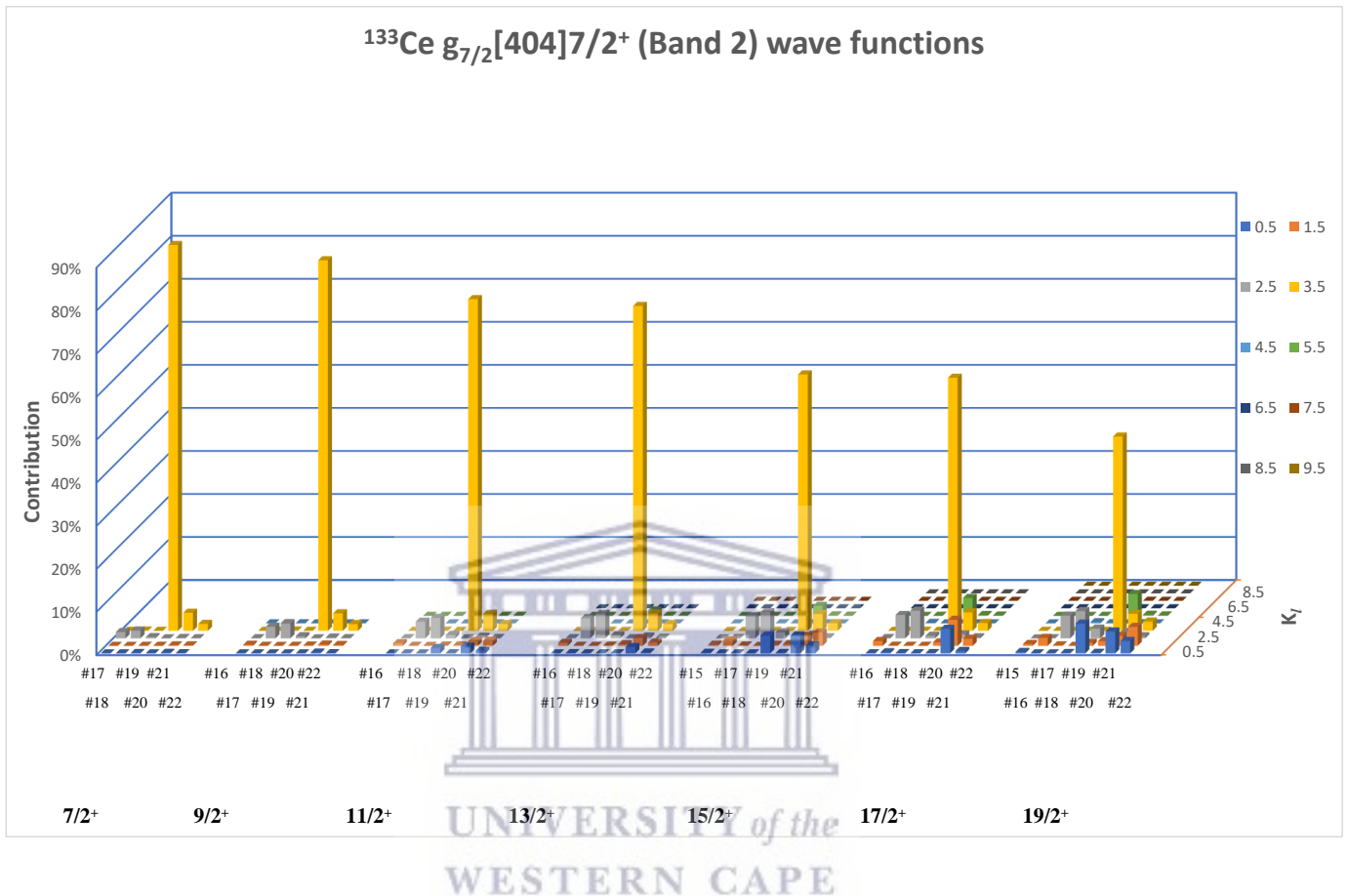
FIGURE 6.3: QTR model wave functions for the states in Band 2 of ^{133}Ce projected onto the long nuclear axis.

they accidentally appear at similar energy to that of the $g_{7/2}$ orbital they mix with it. These orbitals have strong $K_l = 1/2$ components. Such contributions affect the relative energy of the two signature branches of the band due to the decoupling parameter $'a'$ (see Section 2.4.2.1). The decoupling for a $K = 1/2$ configuration is due to the Coriolis interaction thus we conclude that the presence of $K = 1/2$ components in the wave functions of the states in Band 2 is one of the important causes that generate the observed signature splitting. The wave functions of the states in Figure 6.3 also reveal small contributions from components with $(K_l, |\nu\rangle) = (5/2, |17\rangle)$ and $(K_l, |\nu\rangle) = (5/2, |18\rangle)$, shown as grey columns. Orbitals $|17\rangle$ and $|18\rangle$ correspond to a major $g_{7/2}$ component with $\Omega_l = 5/2$ (see Table 6.2)

and thus reflect re-alignment of the angular momentum of the valence $g_{7/2}$ neutron away from the long axis due to the Coriolis interaction.

To gauge the influence of the Coriolis interaction in the states of Band 2 in ^{133}Ce, the QTR model calculations were repeated with the Coriolis interaction (χ) attenuated to 70% of the usual strength, see Figure 6.4. The new set of calculations was able to reproduce the excitation energies across an extended spin range assuming the same deformation parameters as in the first case. When the assumed nuclear shape is axially symmetric with $\gamma = 0°$, the QTR excitation energies reproduce the experimental excitation energies (see panel (a) of Figure 6.4), however the calculations reveal that the signature splitting is absent (see panel (c) of Figure 6.4).

Triaxiality was introduced with $\gamma = 10°$, $15°$ and $20°$. The QTR model is able to reproduce the excitation energies at these values of the γ deformation, however the signature splitting remains vanishingly small for $\gamma = 10°$ and $\gamma = 15°$ (see panel (d) of Figure 6.4 and panel (c) of Figure 6.5, respectively). Only for $\gamma > 15°$ the amplitude of $S(I)$ begins to rise (see panel (d) of Figure 6.5). Therefore when the Coriolis interaction is reduced to 70% a much larger γ deformation of $\gamma \sim 20°$ is required to reproduce the observed energy staggering. This suggests that in these $g_{7/2}$ bands there is a competition between the two modes of generating signature splitting namely; (i) nuclear triaxiality and (ii) Coriolis interaction due to $K = 1/2$ contributions associated with $s_{1/2}$ and $d_{3/2}$ configuration mixture.

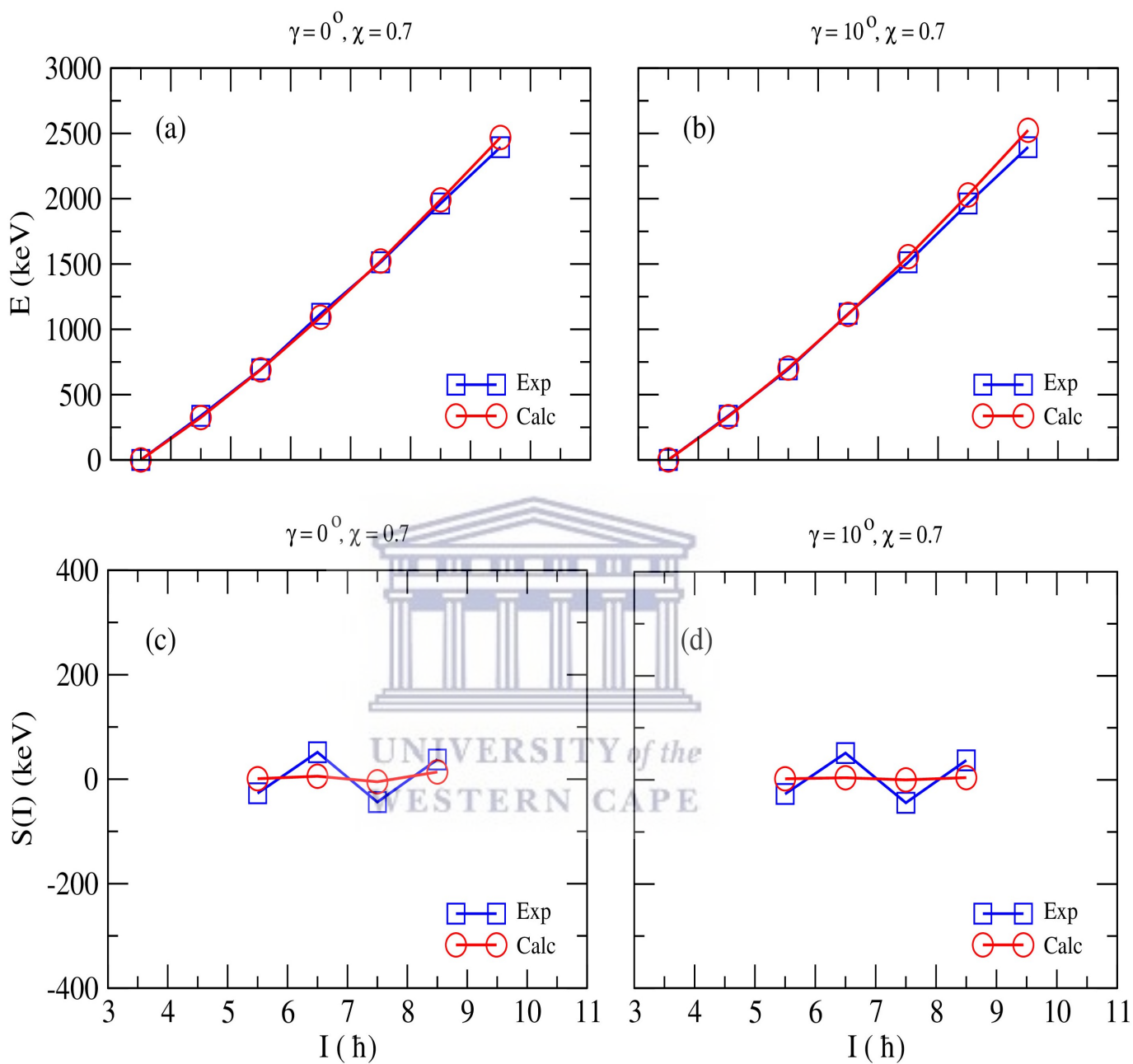FIGURE 6.4: The energy spectra $E(I)$ and signature splitting $S(I)$ for Band 2 of ^{133}Ce at $\gamma = 0°$ and $10°$, and Coriolis interaction (χ) at 70% of the usual strength.
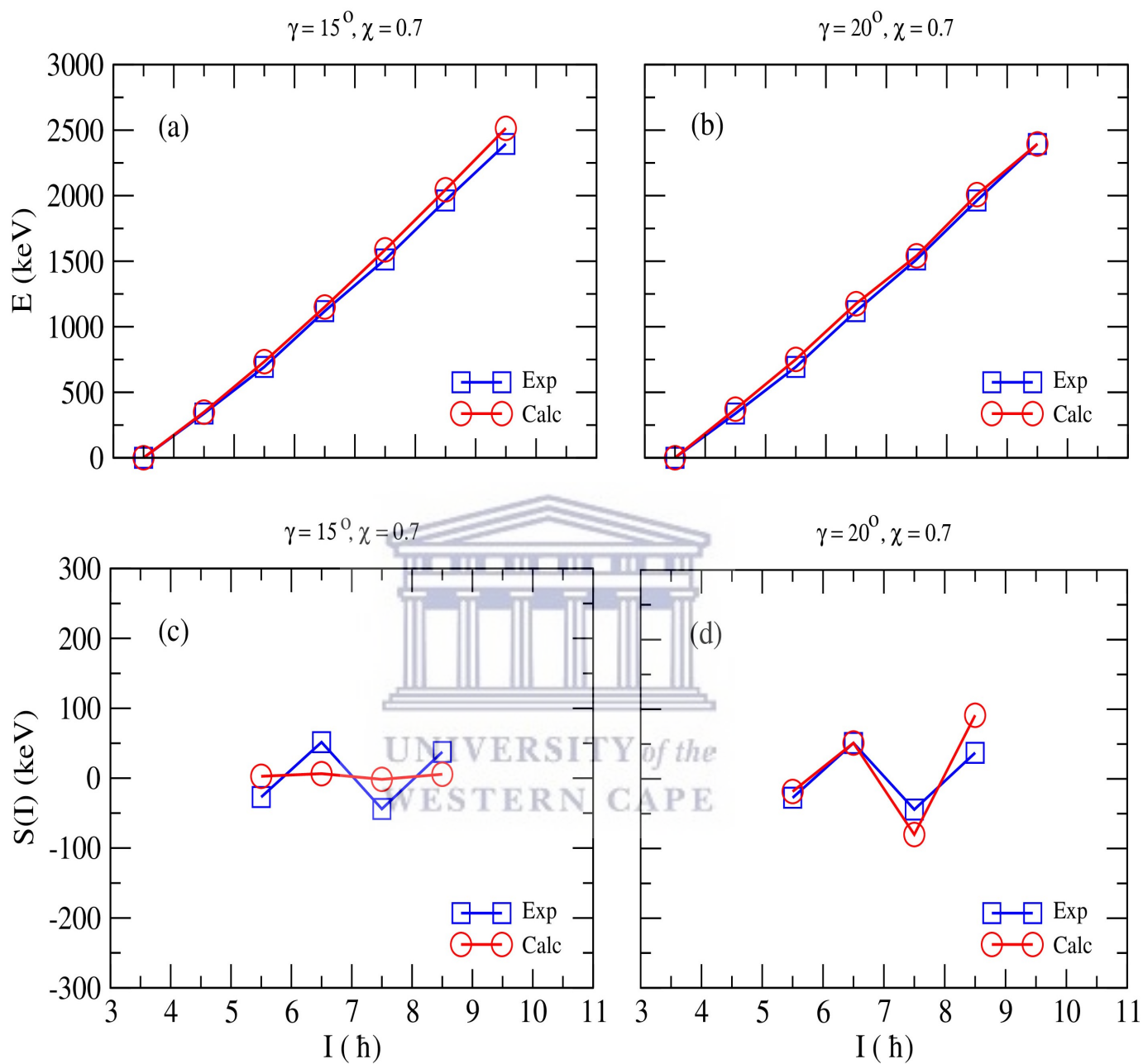
FIGURE 6.5: The energy spectra $E(I)$ and signature splitting $S(I)$ for Band 2 of ^{133}Ce at $\gamma = 15°$ and $20°$, and Coriolis interaction at 70% of the usual strength.

6.2.2 Signature splitting in Band 2 of ^{131}Ba

QTR model calculations were performed to understand the interplay between tri-axiality and signature splitting in Band 2 of ^{131}Ba. The procedure followed for this analysis is the same as that presented for the corresponding structure (Band 2) of the ^{133}Ce isotone in Section 6.2.1, that is a configuration space spanning ten positive-parity orbitals was utilized in the construction of the QTR model states. The deformation parameters used for the calculations are listed in Table 6.1. The Harris parameters used in the calculations are the same as those fitted for the corresponding structure in ^{133}Ce, that is; $\mathcal{J}_0 = 10.4\ \hbar^2\text{MeV}^{-1}$ and $\mathcal{J}_1 = 35.7\ \hbar^4\text{MeV}^{-3}$.

Detailed single-particle information obtained from the QTR model calculations for the ten positive-parity orbitals closest to the Fermi surface (which is placed at $\lambda_F = 51.0$ MeV) is presented in Table 6.4. The information includes the QTR model orbitals $|\nu\rangle$, the single-particle energies ε, the corresponding Nilsson orbitals with largest contributions and the expansion of $|\nu\rangle$ in the basis $|NLJ\Omega\rangle$. The QTR model single-particle orbital that is the main contributor to the states of the $I = 7/2^+$ band structure is $|\nu\rangle = |20\rangle$ and consists predominantly (93%) of the $g_{7/2}$ orbital with a projection of $\Omega_l = 7/2$ on the long axis and is thus mainly related to the $g_{7/2}[404]7/2^+$ Nilsson orbital. In the case of axial symmetry, the orbitals $|\nu\rangle$ corresponds directly to this Nilsson orbital.

The single-particle orbitals are coupled to the triaxial rotor core to produce the QTR model states. At first the calculations were performed assuming an axially symmetric nuclear shape, then nuclear triaxiality was introduced for $\gamma = 10°$, $15°$, and $20°$ with the Coriolis interaction at full strength. The calculations were able to reproduce the excitation energies for axially symmetric deformation (see panel (a) of Figure 6.6), however the calculated S(I) shows an opposite phase at all spins to the experimentally extracted S(I) (see panel (c) of Figure 6.6).

The calculations reveal that the excitation energies are not very sensitive to the γ deformation for small values of γ as the good agreement between the calculated excitation energies and the experimental values persists at $\gamma = 10°$ (see panel (b) of Figure 6.6). However it is noticeable that the signature splitting is very sensitive to the γ deformation, and while at $\gamma = 10°$, $S(I)$ still exhibits opposite phases for the states with $I = 15/2$ and $I = 17/2$, the magnitudes and phases of the calculated and the experimental $S(I)$ match for the states with $I = 11/2$

			Single-particle information
$\|\boldsymbol{\nu}\rangle$	$\Omega^\pi[Nn_z\Lambda]$	$\varepsilon(\text{MeV})$	main components in terms of $\|\boldsymbol{NLJ\Omega}\rangle$
$\|14\rangle$	$1/2^+[420]$	5.4674	$-(0.693)\left\|4g_{\frac{7}{2}}\frac{1}{2}\right\rangle-(0.395)\left\|4g_{\frac{7}{2}}-\frac{3}{2}\right\rangle$
			$-(0.346)\left\|4d_{\frac{5}{2}}\frac{1}{2}\right\rangle$
$\|15\rangle$	$3/2^+[422]$	5.5293	$(0.603)\left\|4d_{\frac{5}{2}}-\frac{3}{2}\right\rangle+(0.475)\left\|4g_{\frac{7}{2}}-\frac{3}{2}\right\rangle$
			$-(0.435)\left\|4g_{\frac{7}{2}}\frac{1}{2}\right\rangle$
$\|16\rangle$	$3/2^+[411]$	5.6143	$-(0.729)\left\|4g_{\frac{7}{2}}-\frac{3}{2}\right\rangle+(0.611)\left\|4d_{\frac{5}{2}}-\frac{3}{2}\right\rangle$
			$+(0.200)\left\|4d_{\frac{3}{2}}\frac{1}{2}\right\rangle$
$\|17\rangle$	$5/2^+[402]$	5.6774	$(0.813)\left\|4g_{\frac{7}{2}}\frac{5}{2}\right\rangle-(0.478)\left\|4d_{\frac{5}{2}}\frac{5}{2}\right\rangle-(0.178)\left\|4d_{\frac{3}{2}}\frac{1}{2}\right\rangle$
$\|18\rangle$	$5/2^+[413]$	5.7862	$(0.828)\left\|4d_{\frac{5}{2}}\frac{5}{2}\right\rangle+(0.498)\left\|4g_{\frac{7}{2}}\frac{5}{2}\right\rangle-(0.162)\left\|4d_{\frac{3}{2}}\frac{1}{2}\right\rangle$
$\|19\rangle$	$1/2^+[400]$	5.8281	$-(0.620)\left\|4d_{\frac{3}{2}}\frac{1}{2}\right\rangle-(0.465)\left\|4s_{\frac{1}{2}}\frac{1}{2}\right\rangle+(0.391)\left\|4g_{\frac{7}{2}}\frac{1}{2}\right\rangle$
$\|\boldsymbol{20}\rangle$	$\boldsymbol{7/2^+[404]}$	**5.8795**	$-\boldsymbol{(0.965)}\left\|4g_{\frac{7}{2}}-\frac{7}{2}\right\rangle+(0.236)\left\|4d_{\frac{3}{2}}-\frac{3}{2}\right\rangle$
			$+(0.067)\left\|4g_{\frac{9}{2}}-\frac{7}{2}\right\rangle$
$\|21\rangle$	$1/2^+[411]$	6.0340	$(0.582)\left\|4s_{\frac{1}{2}}\frac{1}{2}\right\rangle+(0.554)\left\|4d_{\frac{3}{2}}-\frac{3}{2}\right\rangle+(0.446)\left\|4d_{\frac{3}{2}}\frac{1}{2}\right\rangle$
$\|22\rangle$	$3/2^+[402]$	6.1537	$-(0.743)\left\|4d_{\frac{3}{2}}-\frac{3}{2}\right\rangle+(0.459)\left\|4s_{\frac{1}{2}}\frac{1}{2}\right\rangle$
			$+(0.338)\left\|4d_{\frac{3}{2}}\frac{1}{2}\right\rangle$
$\|23\rangle$	$1/2^+[660]$	6.5126	$-(0.793)\left\|6i_{\frac{13}{2}}\frac{1}{2}\right\rangle-(0.482)\left\|6i_{\frac{13}{2}}-\frac{3}{2}\right\rangle$
			$-(0.248)\left\|6g_{\frac{9}{2}}\frac{1}{2}\right\rangle$

TABLE 6.4: QTR model neutron single-particle orbitals, $|\boldsymbol{\nu}\rangle$ with positive-parity lying close to the Fermi level for ^{131}Ba. The orbitals are expanded in the $|\boldsymbol{NLJ\Omega}\rangle$ basis. The corresponding single-particle energies (ε) and the corresponding Nilsson orbitals with largest contributions are also included for the deformation parameters listed in Table 6.1 and $\gamma = 15°$.

and $I = 13/2$. The best agreement between theory and experience is obtained at $\gamma = 15°$ (see panel (c) of Figure 6.7), where the phase and amplitude of the calculated $S(I)$ and the experimentally extracted $S(I)$ show very good agreement. In addition, at $\gamma = 15°$, the QTR model excitation energies reproduce very well the experimental values (see panel (a) of Figure 6.6). Increasing the γ deformation past $\gamma = 15°$ increases the amplitude of $S(I)$, and the agreement for both the excitation energies and $S(I)$ worsens (see panels (b) and (d) of Figure 6.7).

The QTR model calculations reproduce very well the experimentally observed values of $S(I)$ when the adopted nuclear shape is triaxial with $\gamma \approx 15°$ as well as the other experimentally observed band properties, such as excitation energies.
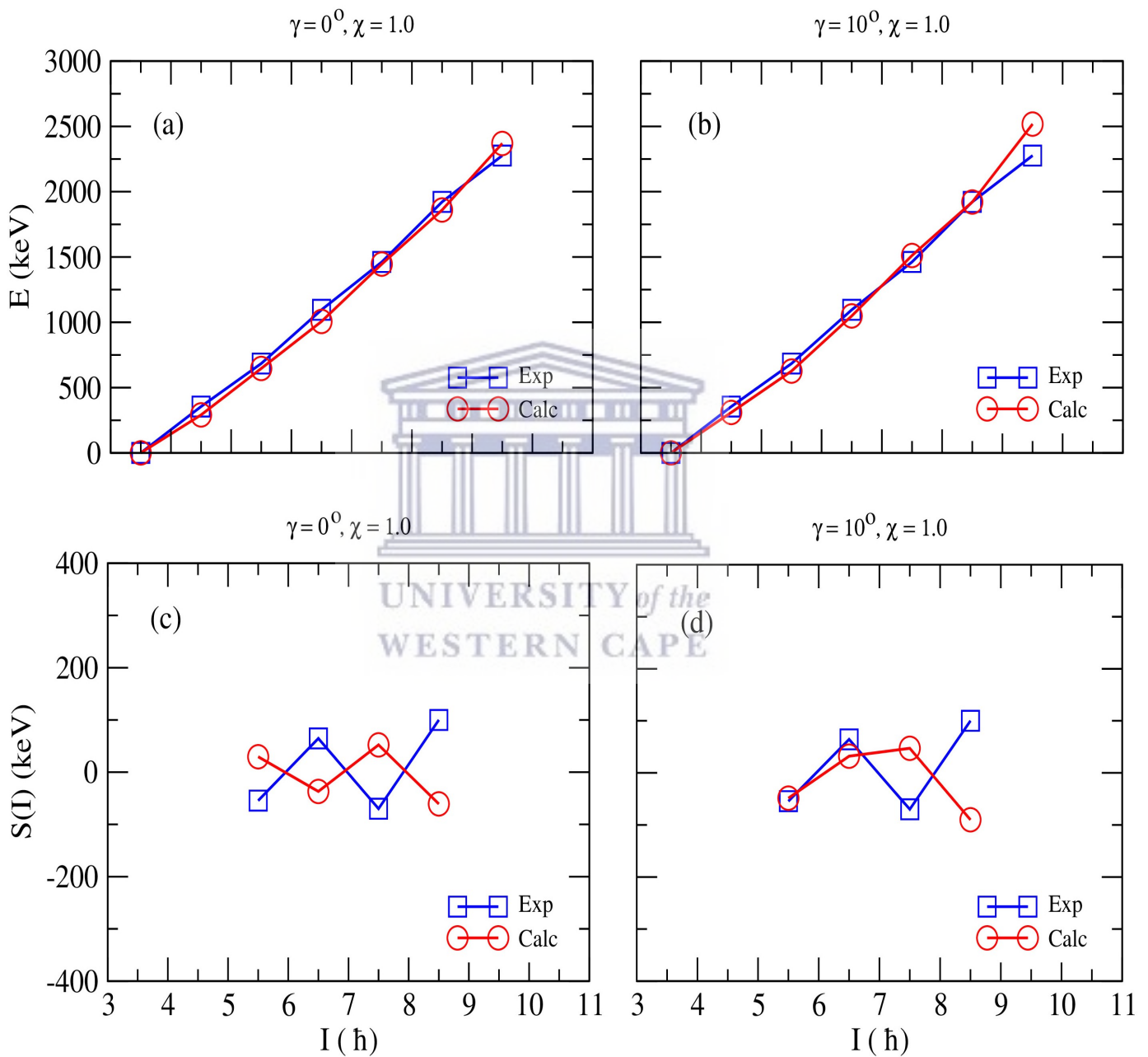
FIGURE 6.6: The energy spectra $E(I)$ and signature splitting $S(I)$ for Band 2 of ^{131}Ba at $\gamma = 0°$ and $10°$, and Coriolis interaction (χ) at full strength.
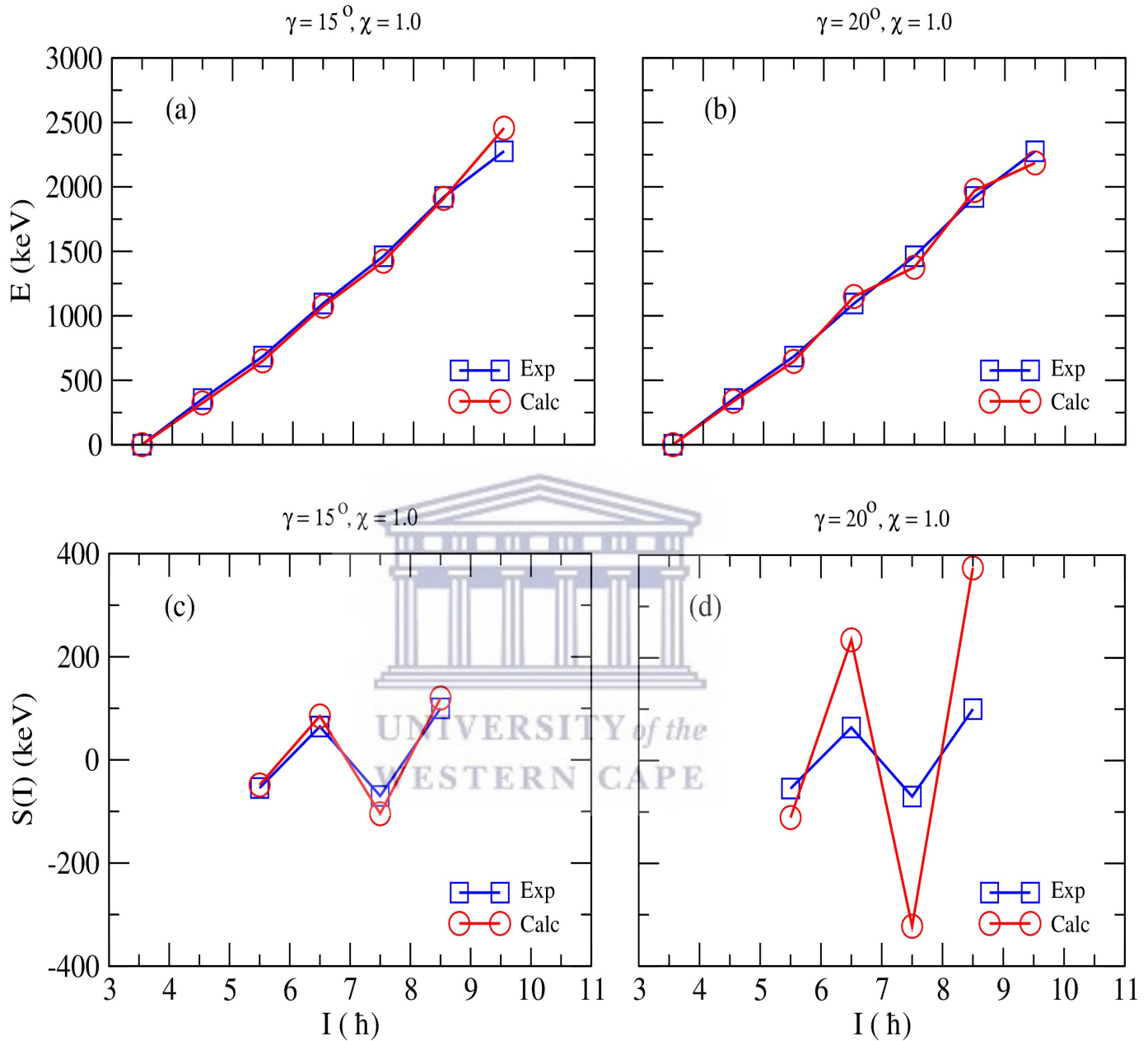
FIGURE 6.7: The energy spectra $E(I)$ and signature splitting $S(I)$ for Band 2
^{131}Ba at $\gamma = 15°$ and $20°$, and Coriolis interaction (χ) at full strength.

Further insights can be gained by looking at the model wave functions. In Table
6.5 the three dominant contributors to the wave function for each state in the ro-
tational band are presented, expanded in a strong coupling basis (K_l, Ω_l). Orbital
$|20\rangle$ with a projection on the long axis of $\Omega_l = 7/2$, and with $(K_l, \Omega_l) = (7/2, 7/2)$
is the largest contributor to each wave function in the band. The bandhead state,

$I^\pi = 7/2^+$, has the composition $\sim 85\%$ $(K_l, \Omega_l) = (7/2, 7/2)$, and marks the highest contribution of any type in the rotational band. It corresponds to a dominant $g_{7/2}[404]7/2$ nature of the type $((K_l, \Omega_l) = (7/2, 7/2)$. This confirms the strong coupling character of the rotational band at the bandhead.

I^π	contribution in terms of $\lvert \boldsymbol{K\nu} \rangle$
$\frac{7}{2}^+$	$(0.927)\left\lvert-\frac{7}{2}20\right\rangle - (0.188)\left\lvert-\frac{7}{2}21\right\rangle - (0.145)\left\lvert\frac{5}{2}18\right\rangle$
$\frac{9}{2}^+$	$(0.912)\left\lvert-\frac{7}{2}20\right\rangle - (0.197)\left\lvert\frac{5}{2}18\right\rangle - (0.188)\left\lvert-\frac{7}{2}21\right\rangle$
$\frac{11}{2}^+$	$(0.653)\left\lvert-\frac{7}{2}20\right\rangle - (0.269)\left\lvert\frac{1}{2}19\right\rangle + (0.199)\left\lvert-\frac{7}{2}21\right\rangle$
$\frac{13}{2}^+$	$(0.779)\left\lvert-\frac{7}{2}20\right\rangle - (0.281)\left\lvert\frac{1}{2}21\right\rangle + (0.266)\left\lvert-\frac{3}{2}21\right\rangle$
$\frac{15}{2}^+$	$(0.519)\left\lvert-\frac{7}{2}20\right\rangle - (0.404)\left\lvert\frac{1}{2}21\right\rangle - (0.345)\left\lvert\frac{1}{2}19\right\rangle$
$\frac{17}{2}^+$	$(0.590)\left\lvert-\frac{7}{2}20\right\rangle - (0.435)\left\lvert\frac{1}{2}21\right\rangle + (0.407)\left\lvert-\frac{3}{2}21\right\rangle$
$\frac{19}{2}^+$	$-(0.461)\left\lvert-\frac{7}{2}20\right\rangle + (0.374)\left\lvert\frac{1}{2}19\right\rangle - (0.366)\left\lvert\frac{1}{2}21\right\rangle$

TABLE 6.5: The amplitude and main components of the QTR model wave functions for states in Band 2 of ^{131}Ba expanded in a strong coupling basis $\lvert K_l\nu \rangle$. The contribution of each $\lvert K_l\nu \rangle$ is the square of the amplitude.

Figure 6.8, is understood in a similar fashion to Figure 6.3. It shows the wave functions of the states in Band 2 of ^{131}Ba. Each grouping of columns represents the state wave function. The orbitals $\lvert \nu \rangle$ that are present are labelled from left to right on the x-axis by $(\#)$. On the y-axis one obtains the value of K_l, the projection of the total angular momentum on the long nuclear axis, which is also reflected by color, see the legend of the figure. The height of each column represents the contribution (square of the amplitude) of the component (K_l, Ω_l) to the state wave function.

From Figure 6.8 one can deduce that as the spin increases, the contribution of $(K_l, \Omega_l) = (7/2, 7/2)$ type (yellow column) to the wave functions decreases as in the corresponding structure of ^{133}Ce. However the decline in ^{131}Ba is much more rapid when compared to the ^{133}Ce structure. The model wave functions exhibit a strong oscillatory pattern for the states in the ^{131}Ba structure, that is—while as a general trend the $(7/2, 7/2)$ contributions to the total state wave function decrease with increasing spin, this decrease is not monotonic. The contribution of $(7/2, 7/2)$ to a positive-signature state is noticeably greater when compared to the immediately preceding negative-signature state.

In addition, the odd-signature states have significantly greater contributions of components with $K_l = 1/2$ from orbitals $\lvert 19 \rangle$, $\lvert 21 \rangle$ and $\lvert 22 \rangle$. The staggering behavior observed for the $S(I)$ plots is thus reflected in the wave functions which
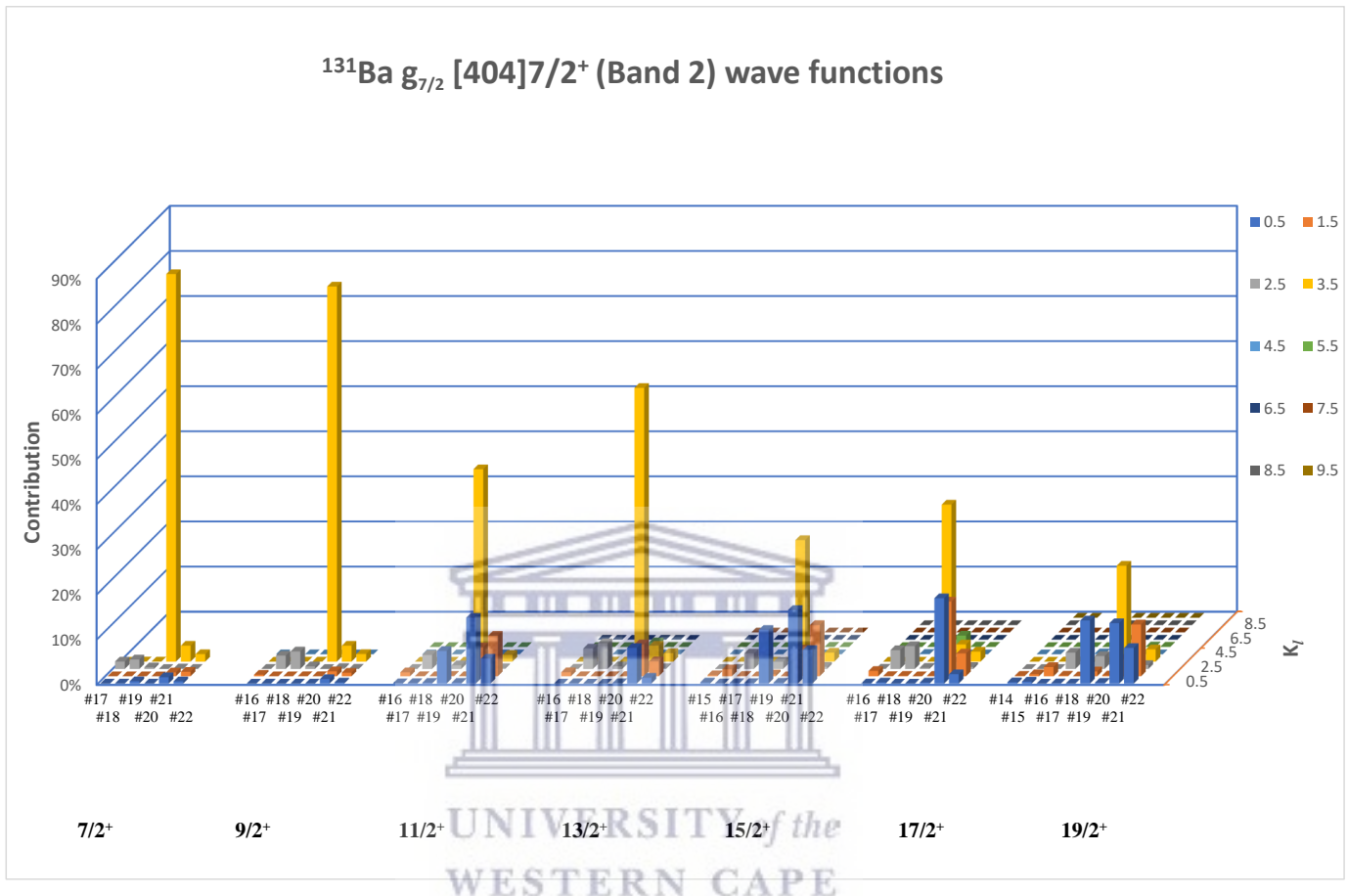
FIGURE 6.8: An illustration of the components of the QTR model wave functions for the states in Band 2 of ^{131}Ba.

have dominant $g_{7/2}$ nature but also includes components with $\Omega_l = 1/2$ and their relative strengths oscillates for the positive and negative signature components of the band. At the deformation of $\varepsilon_2 = 0.170$, the $\nu s_{1/2}[411]1/2^+$ orbital lies very close to the $\nu g_{7/2}[404]7/2^+$ orbital and as we discussed previously, the Coriolis interaction can cause significant staggering in $K = 1/2$ bands.

Furthermore, there are many contributions with different K_l in the state wave functions. In particular there are contributions from orbitals $|17\rangle$ and $|18\rangle$ with major $g_{7/2}$ nature, but $\Omega_l = 5/2$, suggesting that the Coriolis interaction also re-aligns the single-particle angular momentum away from the long axis. Thus the

wave functions for the states of Band 2 reveal a mixture of contributions with generally dominant $g_{7/2}$ nature.

To gauge the impact of the Coriolis interaction in this band, the QTR model calculations were repeated with the Coriolis interaction (χ) attenuated to 70% of the usual strength. The calculations show that for $\chi = 0.7$ a much larger value of triaxiality of $\gamma \sim 20°$ is required to reproduce the amplitude and phase of the experimentally observed staggering (see panel (d) of Figure 6.10) as the absence of energy level staggering is evident for the entire range of $0° \leq \gamma < 20°$ (see panels (c) and (d) of Figure 6.9 and panel (c) of Figure 6.10). In addition, there is worse agreement for the excitation energies, except for $\gamma = 20°$.

To summarize the discussion so far, there are two known modes of generating energy staggering in atomic nuclei; (i) nuclear non-axiality (triaxiality) and (ii) the Coriolis interaction. In this work and based on the presented QTR model calculation, the newly observed bands built on the $I^\pi = 7/2^+$ states in both ^{131}Ba and ^{133}Ce isotones are associated with the $\nu g_{7/2}[404]7/2^+$ Nilsson configuration and with a moderate triaxiality of $\gamma \approx 15°$. The calculations reproduce well the excitation energies and the signature splitting in these bands. While the states in both bands were described as associated with a dominant $g_{7/2}[404]7/2^+$ nature, however, there are also admixture of other $g_{7/2}$, $s_{1/2}$ and $d_{3/2}$ orbitals. The presence of some $K_l = 1/2$ contributions with $s_{1/2}$ and $d_{3/2}$ nature in the wave functions causes significant energy staggering due to the Coriolis interaction. Thus, in addition to triaxiality the energy staggering, $S(I)$, in the band structures of ^{131}Ba and ^{133}Ce is also significantly affected by the Coriolis interaction.
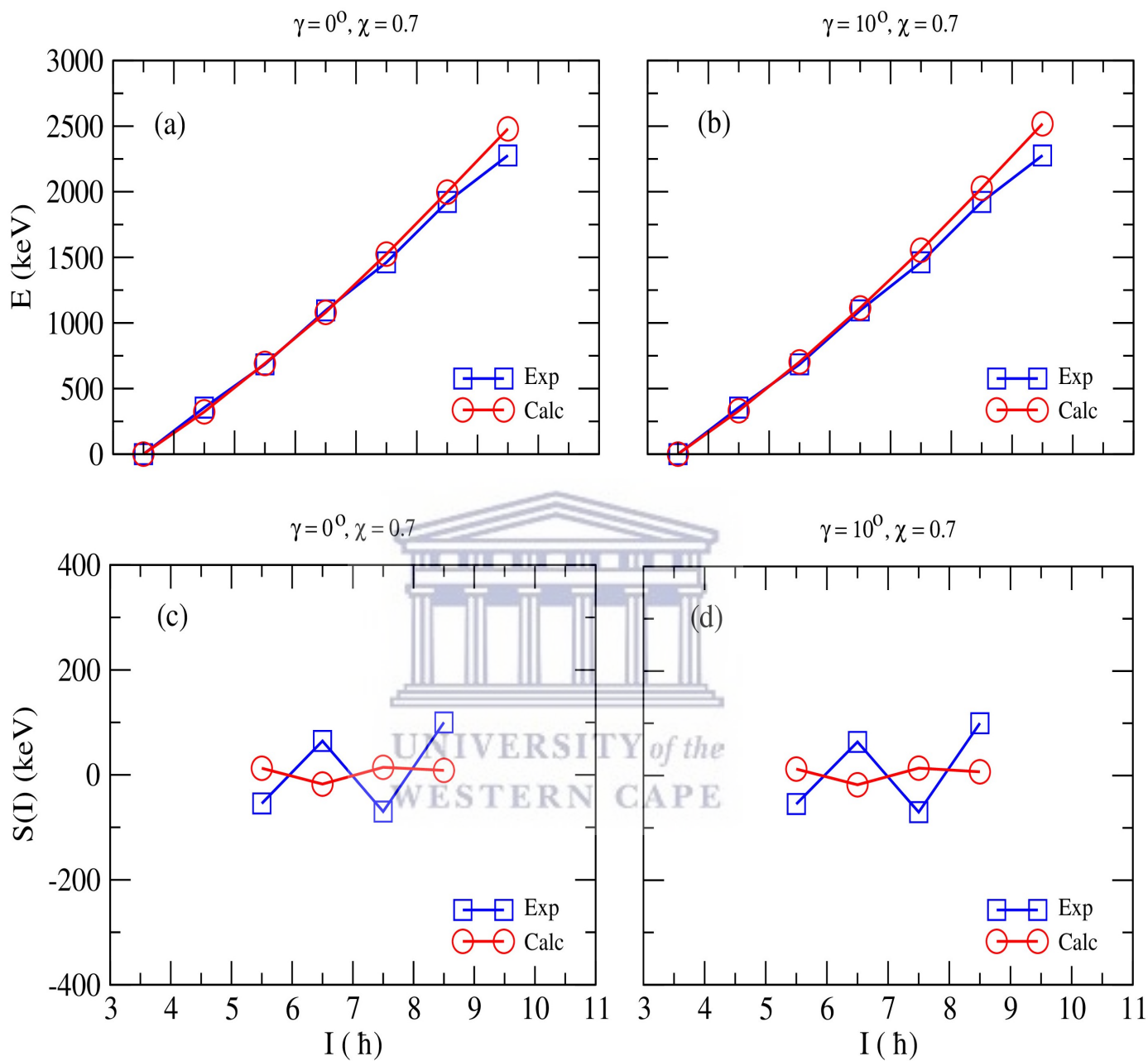
FIGURE 6.9: The energy spectra $E(I)$ and signature splitting $S(I)$ for Band 2 of ^{131}Ba at $\gamma = 0°$ and $10°$, and Coriolis interaction (χ) at 70% of the usual strength.
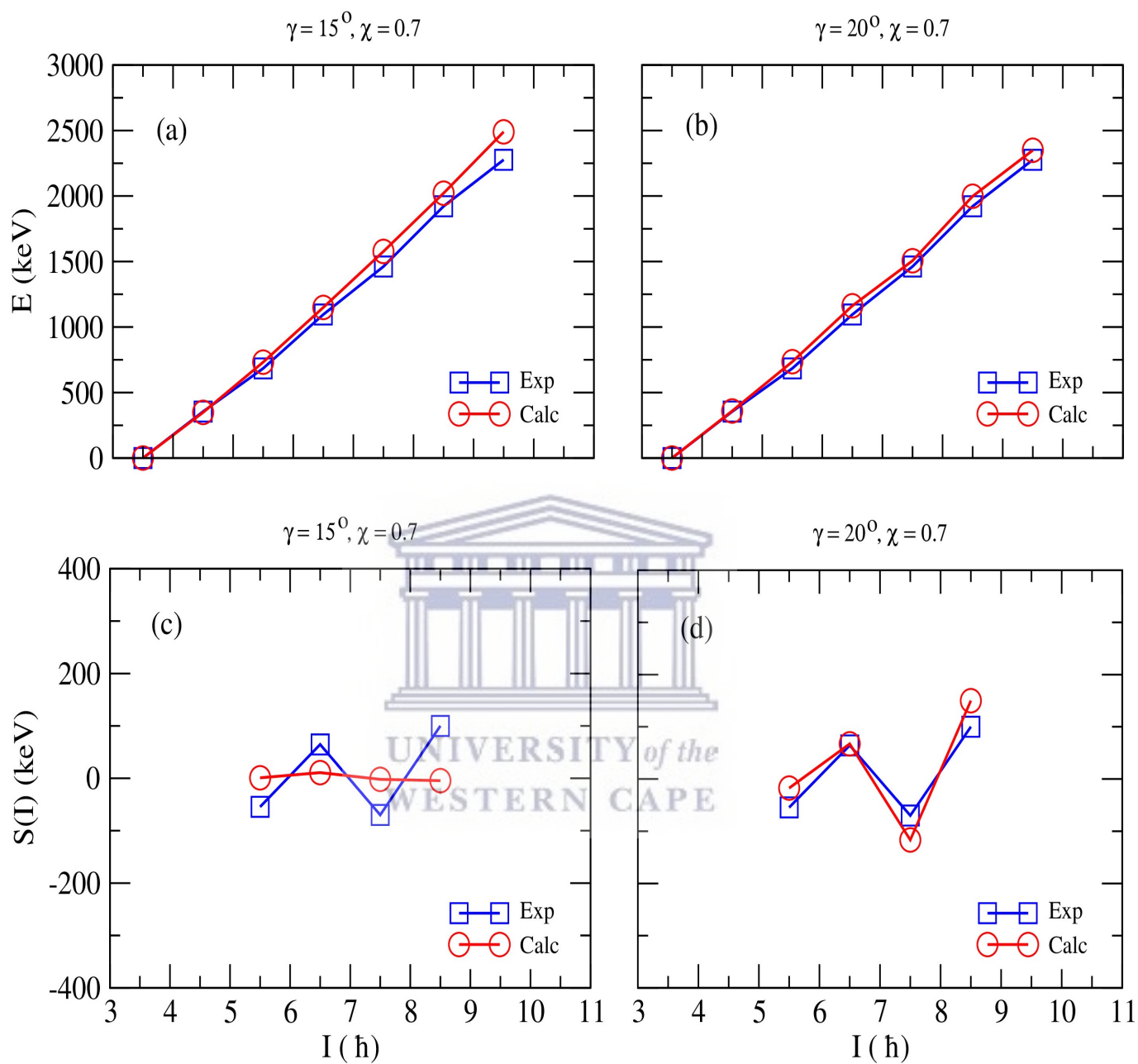
FIGURE 6.10: The energy spectra $E(I)$ and signature splitting $S(I)$ for Band 2 of ^{131}Ba at $\gamma = 15°$ and $20°$, and Coriolis interaction (χ) at 70% of the usual strength.

6.2.3 Signature splitting in the $\pi g_{7/2}[404]7/2^+$ bands of the $Z = 75$ isotopes

It is interesting to compare the signature splitting $S(I)$ in the $N = 75$ isotones and in the $Z = 75$ isotopes. When one looks at bands built on the $\pi g_{7/2}[404]7/2^+$ configuration in the $Z = 75$ isotopes, practically all nuclei have absent or vanishingly small signature splitting $S(I)$. It should be noted that the nuclei in this mass region are predicted to have an axially symmetric nuclear shape. Furthermore, the $\pi s_{1/2}[411]1/2^+$ proton orbital lies far from the $\pi g_{7/2}[404]7/2^+$ orbital (see Figure 2.6). As there is a large energy gap the contributions of $\pi s_{1/2}$ orbitals to the $\pi g_{7/2}$ band would be small. Contrary to that the $\nu s_{1/2}[411]1/2^+$ neutron orbital lies very close to the $\nu g_{7/2}[404]7/2^+$ orbital, see Figure 2.5.

This is confirmed by the experimental observations. For instance, the $7/2^+$ state of the $\nu g_{7/2}[404]7/2^+$ band structure in ^{131}Ba lies only 18 keV below the $7/2^+$ state of the $\nu s_{1/2}[411]1/2^+$ ground state band and the $13/2^+$ state of the $\nu g_{7/2}[404]7/2^+$ band structure in ^{133}Ce is nearly-degenerate (within 14 keV) with the $13/2^+$ state of the $\nu s_{1/2}[411]1/2^+$ ground state band. Contrary to that, bands associated with $\pi s_{1/2}[411]1/2^+$ configuration are not observed in any of the $Z = 75$ isotopes and are thus expected to appear at much higher excitation energy. Therefore the observed lack of energy staggering in the $\pi g_{7/2}$ bands in the $Z = 75$ isotopes can be explained by the absence of the $\pi s_{1/2}$ orbital contributions in the wave functions and by the axial deformation of the nuclear shapes.

6.2.4 Summary of Part I

QTR model calculations were performed for two newly discovered rotational bands in the $Z = 75$ isotones of ^{133}Ce and ^{131}Ba. The bands are built on the $I^\pi = 7/2^+$ states in both nuclei. A dominant Nilsson configuration of $\nu g_{7/2}[404]7/2^+$ was suggested with a quadruple deformation of $\varepsilon_2 = 0.185$ for the structure in ^{133}Ce and $\varepsilon_2 = 0.170$ for the band in ^{131}Ba. A modest triaxiality of $\sim 15°$ was required to reproduce the observed band properties.

The calculations revealed that in addition to nuclear non-axiality (triaxiality), the observed band properties, including the excitation energies and energy staggering are strongly influenced by the Coriolis interaction which causes orbital mixing between the $\nu g_{7/2}$ and the nearby $\nu s_{1/2}$ and $\nu d_{3/2}$ orbitals, such mixing has a significant $K = 1/2$ component in their wave functions and is one of the main contributors generating energy staggering in these $g_{7/2}$ bands.

6.3 Part II: Interpretation of the negative-parity structure in ^{133}Ce

6.3.1 Introduction

As we have seen in Chapter 3, triaxially deformed nuclei can access a variety of excitation modes including vibrations, three-dimensional rotational motion, nuclear wobbling motion as proposed in Ref. [15], and chirality. The last three modes necessarily being unique to triaxial nuclei. Nuclear chirality has been reported in the $A = 130$ mass region (see for instance works on chiral bands in ^{131}Ba [28], ^{133}La [57], and ^{133}Ce [6]). Evidence for nuclear wobbling motion was reported in the $A = 160$ mass region where the observed bands were built on the $\pi i_{13/2}$ configuration and corresponded to a large nuclear deformation of $\varepsilon_2 \approx 0.40$, see for instance published results for ^{161,163,165,167}Lu [16, 34, 55, 63], and ^{167}Ta [31]. The longitudinal wobbling bands reported in these Lu isotopes were later re-interpreted in terms of transverse wobbling motion in Ref. [23], but this new interpretation remains controversial [42, 71, 72].

The negative-parity structure, Band 1 of ^{133}Ce (see Figure 5.1), forms the yrast rotational sequence. It was observed in previous works and a 1-quasineutron $\nu(h_{11/2})^{-1}[514]9/2^-$ configuration with a triaxiality of $\sim 20°$ [33, 52, 56] was assigned to this band. Nuclei in the $A = 130$ mass region are predicted to exhibit large triaxiality at low to medium spins, while the valence protons from the bottom of the $h_{11/2}$ shell favor prolate nuclear shapes, valence neutrons from the top of the $h_{11/2}$ shell favour oblate shapes. It is this competing mechanisms that drives these nuclei to triaxial shapes [56].

6.3.2 Tilted precession (TiP) interpretation for $h_{11/2}$ bands in ^{133}Ce

QTR model calculations were performed with the deformation parameters presented in Table 6.1. A single-particle configuration space spanning nine negative-parity orbitals close to the Fermi surface were used to account for the single-particle degrees of freedom. The MoI's of the core were assumed to follow the irrotational-flow dependence with respect to the γ deformation [48]. Harris parametrization

for the MoI's of the core was used with $\mathcal{J}_0 = 10 \ \hbar^2\text{MeV}^{-1}$ and $\mathcal{J}_1 = 25 \ \hbar^4\text{MeV}^{-3}$. The electromagnetic transition probabilities were calculated with an effective g_s factor of $g_s = 0.6g_{free}$ and a core g-factor of $g_R = Z/A = 0.44$ was used [62].

Table 6.6 presents the nine negative-parity orbitals close to the Fermi surface used in the calculations and includes; the orbital, $|\nu\rangle$, the approximate Nilsson quantum numbers, the single-particle energies (ε) and the main components of $|\nu\rangle$ expanded in a basis $|NLJ\Omega\rangle$, where N is the major oscillator shell number, L is the orbital angular momentum quantum number, J is the total single-particle angular momentum quantum and Ω_l is the projection of J on the long axis. Orbitals $|14\rangle$ to $|19\rangle$ originate from the $h_{11/2}$ sub-shell with projections on the long axis of $\Omega_l = 1/2$ to $\Omega_l = 11/2$, respectively (see Table 6.6).

		Single-particle information	
$\|\boldsymbol{\nu}\rangle$	$\Omega^\pi[Nn_z\Lambda]$	$\varepsilon(\text{MeV})$	main components in terms of $\|\boldsymbol{NLJ\Omega_l}\rangle$
$\|14\rangle$	$1/2^-[550]$	5.6569	$0.783 \left\|5h_{\frac{11}{2}}\frac{1}{2}\right\rangle + 0.512 \left\|5h_{\frac{11}{2}} -\frac{3}{2}\right\rangle + 0.246 \left\|5h_{\frac{11}{2}}\frac{5}{2}\right\rangle$
$\|15\rangle$	$3/2^-[541]$	5.7429	$0.772 \left\|5h_{\frac{11}{2}} -\frac{3}{2}\right\rangle - 0.404 \left\|5h_{\frac{11}{2}}\frac{1}{2}\right\rangle - 0.359 \left\|5h_{\frac{11}{2}}\frac{5}{2}\right\rangle$
$\|16\rangle$	$5/2^-[532]$	5.8083	$-0.864 \left\|5h_{\frac{11}{2}}\frac{5}{2}\right\rangle + 0.360 \left\|5h_{\frac{11}{2}}\frac{1}{2}\right\rangle + 0.185 \left\|5f_{\frac{7}{2}}\frac{1}{2}\right\rangle$
$\|17\rangle$	$7/2^-[523]$	5.9012	$-0.955 \left\|5h_{\frac{11}{2}}\frac{7}{2}\right\rangle + 0.192 \left\|5h_{\frac{11}{2}}\frac{-3}{2}\right\rangle + 0.152 \left\|5f_{\frac{7}{2}} -\frac{3}{2}\right\rangle$
$\|\mathbf{18}\rangle$	$\mathbf{9/2^-[514]}$	**6.0356**	$\mathbf{0.981} \left\|5h_{\frac{11}{2}}\frac{9}{2}\right\rangle - 0.149 \left\|5f_{\frac{7}{2}}\frac{5}{2}\right\rangle - 0.104 \left\|5h_{\frac{11}{2}}\frac{5}{2}\right\rangle$
$\|19\rangle$	$11/2^-[505]$	6.2121	$0.986 \left\|5h_{\frac{11}{2}} -\frac{11}{2}\right\rangle - 0.155 \left\|5f_{\frac{7}{2}} -\frac{7}{2}\right\rangle - 0.049 \left\|5h_{\frac{11}{2}} -\frac{7}{2}\right\rangle$
$\|20\rangle$	$1/2^-[541]$	6.2637	$-0746 \left\|5f_{\frac{7}{2}}\frac{1}{2}\right\rangle - 0.400 \left\|5p_{\frac{3}{2}} -\frac{3}{2}\right\rangle - 0.299 \left\|5f_{\frac{7}{2}} -\frac{3}{2}\right\rangle$
$\|21\rangle$	$1/2^-[530]$	6.3212	$-0.724 \left\|5h_{\frac{9}{2}}\frac{1}{2}\right\rangle - 0.463 \left\|5h_{\frac{9}{2}} -\frac{3}{2}\right\rangle - 0.317 \left\|5f_{\frac{5}{2}}\frac{1}{2}\right\rangle$
$\|22\rangle$	$3/2^-[532]$	6.3921	$-0.606 \left\|5f_{\frac{7}{2}} -\frac{3}{2}\right\rangle + 0.437 \left\|5h_{\frac{9}{2}}\frac{1}{2}\right\rangle + 0.320 \left\|5h_{\frac{9}{2}} -\frac{3}{2}\right\rangle$

TABLE 6.6: Neutron single-particle orbitals, $|\nu\rangle$ with negative-parity lying close to the Fermi level for ^{133}Ce, expanded in the basis $|\boldsymbol{NLJ\Omega_l}\rangle$ together with the single particle energies (ε) and approximate Nilsson quantum numbers at the deformation parameters listed in Table 6.1. The contribution of $|NLJ\Omega_l\rangle$ to $|\nu\rangle$ is the square of the amplitude of $|NLJ\Omega_l\rangle$.

The orbital closest to the Fermi level is $|\nu\rangle = |18\rangle$. The yrast band (Band 1) is thus mainly associated with orbital $|18\rangle$ which consists predominantly (96%) of the $h_{11/2}$ orbital with a projection of 9/2 on the long axis. The projections K and Ω do not have sharp values on any intrinsic nuclear axis. Each $|\nu\rangle$ consists of contributions with different Ω on the long axis. The excited band (Band 4) has the same intrinsic configuration as Band 1, that is it is associated mainly

with $|\nu\rangle = |18\rangle$, however the states in this band have an extra $\sim 2\hbar$ of rotational angular momentum along the long axis (for more information, see the discussion in Chapter 3, Section 3.2.1).

The excitation energies of the negative-parity bands are compared with the experimental data in panel (a) of Figure 6.11. The calculations are able to correctly predict the excitation energies of both Band 1 (shown in blue) and Band 4 (shown in red) across the whole spin range, although the agreement is moderate. The calculations have a shortcoming as they do not predict correctly the ordering of the $9/2^-$ and $11/2^-$ states in the yrast sequence, which results in an underprediction of the calculated excitation energy for Band 1. The QTR model achieves very good agreement with the experimental data for the signature splitting $S(I)$ of Band 1 (see panel (b) of Figure 6.11). The experimental staggering for Band 4 is not reproduced very well, however the calculations do predict correctly that the $S(I)$ has a smaller magnitude and undergoes a phase change.

The calculated first excited band, Band 4, has the same intrinsic configuration as Band 1 with a band head at $I = 13/2^-$. This state is generated when the total angular momentum vector tilts away from the intermediate axis, due to additional rotation of $2\hbar$ along the long axis. It is also possible to develop a second excited band, being built on a state with $\approx 2\hbar$ greater rotational angular momentum along the long axis than the band head of the first excited band. This second excited band would correspond to a further tilt of the total angular momentum vector away from the intermediate axis [42, 44]. For the current configuration, we have $I_{bandhead} = 9/2\hbar$ for the yrast band, thus the first excited band (Band 4) would have a spin of $I = 13/2\hbar$. Indeed this is the measured spin of the band head of Band 4. Figure 3.3 illustrates the energy spectra and the angular momenta couplings of the yrast band and an excited band built on the $h_{11/2}$ orbital with a projection of $9/2$ on the long axis.

Wave functions for Band 1

The QTR model wave functions of the yrast band have been projected onto the long nuclear axis and the three dominant components for each of the states in the band are listed in Table 6.7 and the total wave functions for the states of Band 1 are plotted in Figure 6.12 (to be understood in a similar way to Figure 6.3
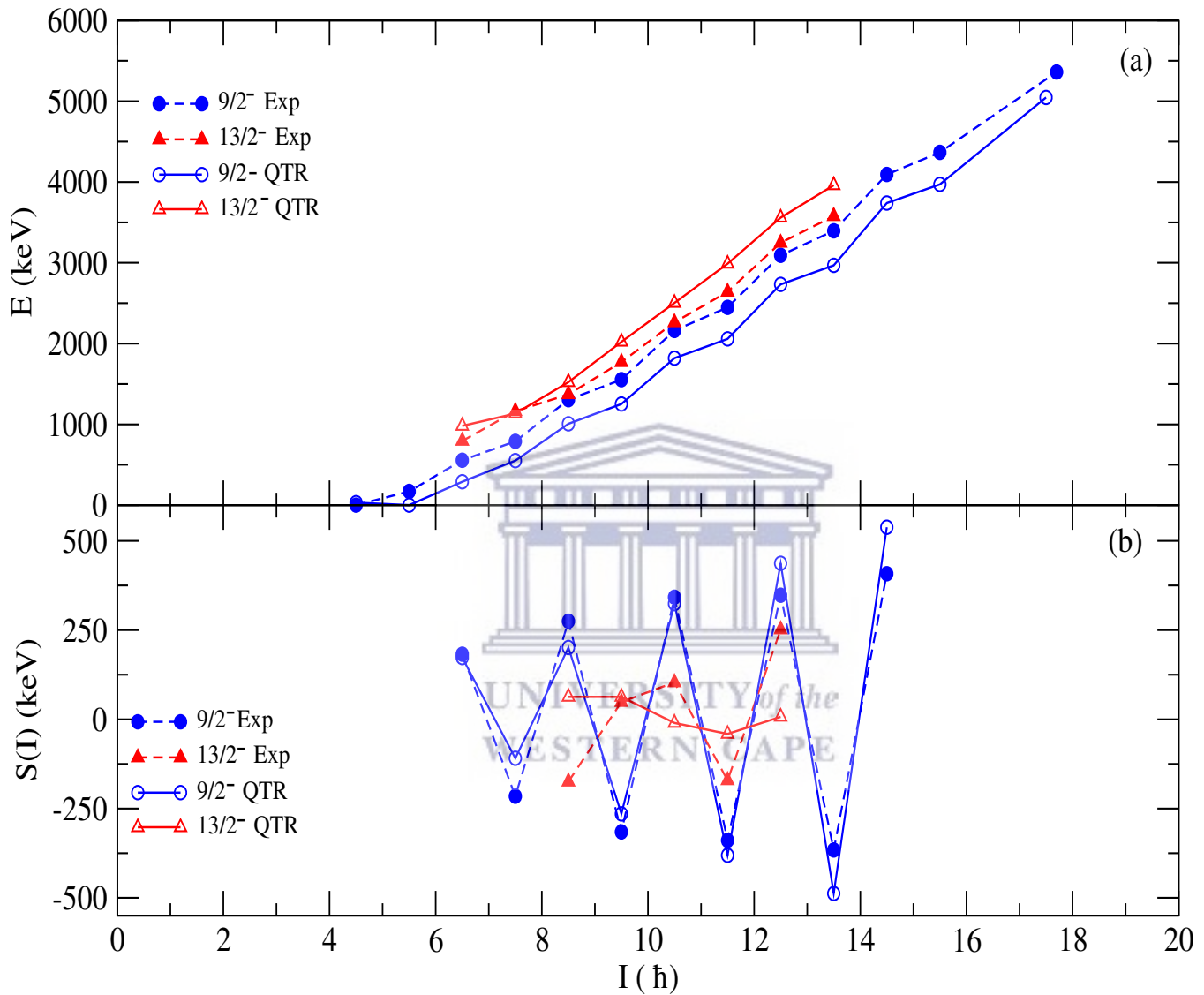
FIGURE 6.11: Panel (a) Excitation energy $E(I)$ plot for Band 1 (shown in blue) and Band 4 (shown in red) in ^{133}Ce. Panel (b) shows the corresponding signature splitting, S(I) for panel (a). The dashed lines denote the experimental data.

and Figure 6.8). The wave functions reveal that the band head state, $I^\pi = 9/2^-$ of Band 1, is composed predominantly of orbital $|18\rangle$ with a dominant $\Omega_l = 9/2$ nature, with a contribution of 71.5% to the state wave function. In addition to the dominant $(K_l, \Omega_l) = (9/2, 9/2)$ component, there is also a contribution of $\sim 20\%$ from the $(K_l, \Omega_l) = (7/2, 7/2)$ component. The presence of $(7/2, 7/2)$ component

suggests that already at the band head, the single-particle angular momentum is not fully aligned along the long axis.

The states with $I^\pi = 9/2^-$ to $I^\pi = 17/2^-$ in Band 1 have a dominant $\Omega_l = 9/2$ nature because the $(K_l, \Omega_l) = (9/2, 9/2)$ component has the largest contributions to the wavefunctions of the states. While the $(9/2, 9/2)$ component is dominant for these states, the magnitude of this contribution is decreasing with increasing spin (see the light-blue column in Figure 6.12). In fact, the $(7/2, 7/2)$, $(11/2, 11/2)$ and $(5/2, 5/2)$ components are also present at low spins and their contributions to the wave functions increase with increasing spin (see the yellow, green, and grey columns, respectively in Figure 6.12). This is due to the Coriolis interaction which causes the misalignment of the single-particle angular momentum of the valence hole, $\vec{j}$, leading to components with $\Omega_l = 7/2$ and $\Omega_l = 5/2$.

I^π	contribution in terms of $|K_l\nu\rangle$
$\frac{9}{2}^-$	$-0.846\left|\frac{9}{2}18\right\rangle - 0.477\left|-\frac{7}{2}17\right\rangle + 0.205\left|\frac{5}{2}16\right\rangle$
$\frac{11}{2}^-$	$0.715\left|\frac{9}{2}18\right\rangle - 0.460\left|-\frac{7}{2}17\right\rangle + 0.412\left|-\frac{11}{2}19\right\rangle$
$\frac{13}{2}^-$	$-0.705\left|\frac{9}{2}18\right\rangle - 0.489\left|-\frac{7}{2}17\right\rangle + 0.391\left|-\frac{11}{2}19\right\rangle$
$\frac{15}{2}^-$	$-0.606\left|\frac{9}{2}18\right\rangle + 0.508\left|-\frac{7}{2}17\right\rangle + 0.325\left|\frac{5}{2}16\right\rangle$
$\frac{17}{2}^-$	$-0.618\left|\frac{9}{2}18\right\rangle - 0.503\left|-\frac{7}{2}17\right\rangle + 0.299\left|\frac{11}{2}19\right\rangle$
$\frac{19}{2}^-$	$-0.478\left|\frac{9}{2}18\right\rangle + 0.475\left|-\frac{7}{2}17\right\rangle + 0.356\left|\frac{5}{2}16\right\rangle$
$\frac{21}{2}^-$	$0.528\left|\frac{9}{2}18\right\rangle + 0.472\left|-\frac{7}{2}17\right\rangle - 0.360\left|\frac{13}{2}18\right\rangle$
$\frac{23}{2}^-$	$0.438\left|-\frac{7}{2}17\right\rangle - 0.395\left|\frac{9}{2}18\right\rangle + 0.366\left|\frac{5}{2}16\right\rangle$
$\frac{25}{2}^-$	$0.472\left|\frac{9}{2}18\right\rangle + 0.450\left|\frac{7}{2}17\right\rangle - 0.375\left|\frac{13}{2}18\right\rangle$
$\frac{27}{2}^-$	$0.408\left|-\frac{7}{2}17\right\rangle + 0.37\left|\frac{5}{2}16\right\rangle - 0.340\left|\frac{9}{2}18\right\rangle$
$\frac{29}{2}^-$	$-0.434\left|\frac{9}{2}18\right\rangle - 0.432\left|-\frac{7}{2}17\right\rangle + 0.368\left|\frac{13}{2}18\right\rangle$
$\frac{31}{2}^-$	$-0.385\left|-\frac{7}{2}17\right\rangle - 0.372\left|\frac{5}{2}16\right\rangle + 0.320\left|\frac{1}{2}16\right\rangle$
$\frac{35}{2}^-$	$-0.371\left|\frac{5}{2}16\right\rangle - 0.366\left|\frac{-7}{2}17\right\rangle + 0.329\left|\frac{1}{2}16\right\rangle$

TABLE 6.7: The amplitudes and main components of the QTR model wave functions for states in the yrast band of ^{133}Ce expanded in a strong coupling basis $|K_l\nu\rangle$. The contribution of each $|K_l\nu\rangle$ is the square of the amplitude.

At spins $I^\pi = 23/2^-$ to $I^\pi = 29/2^-$, the $(7/2, 7/2)$, $(11/2, 11/2)$, $(13/2, 9/2)$ and $(5/2, 5/2)$ components come so low in energy that for some states these components are favored and they become the dominant components in the wave functions.
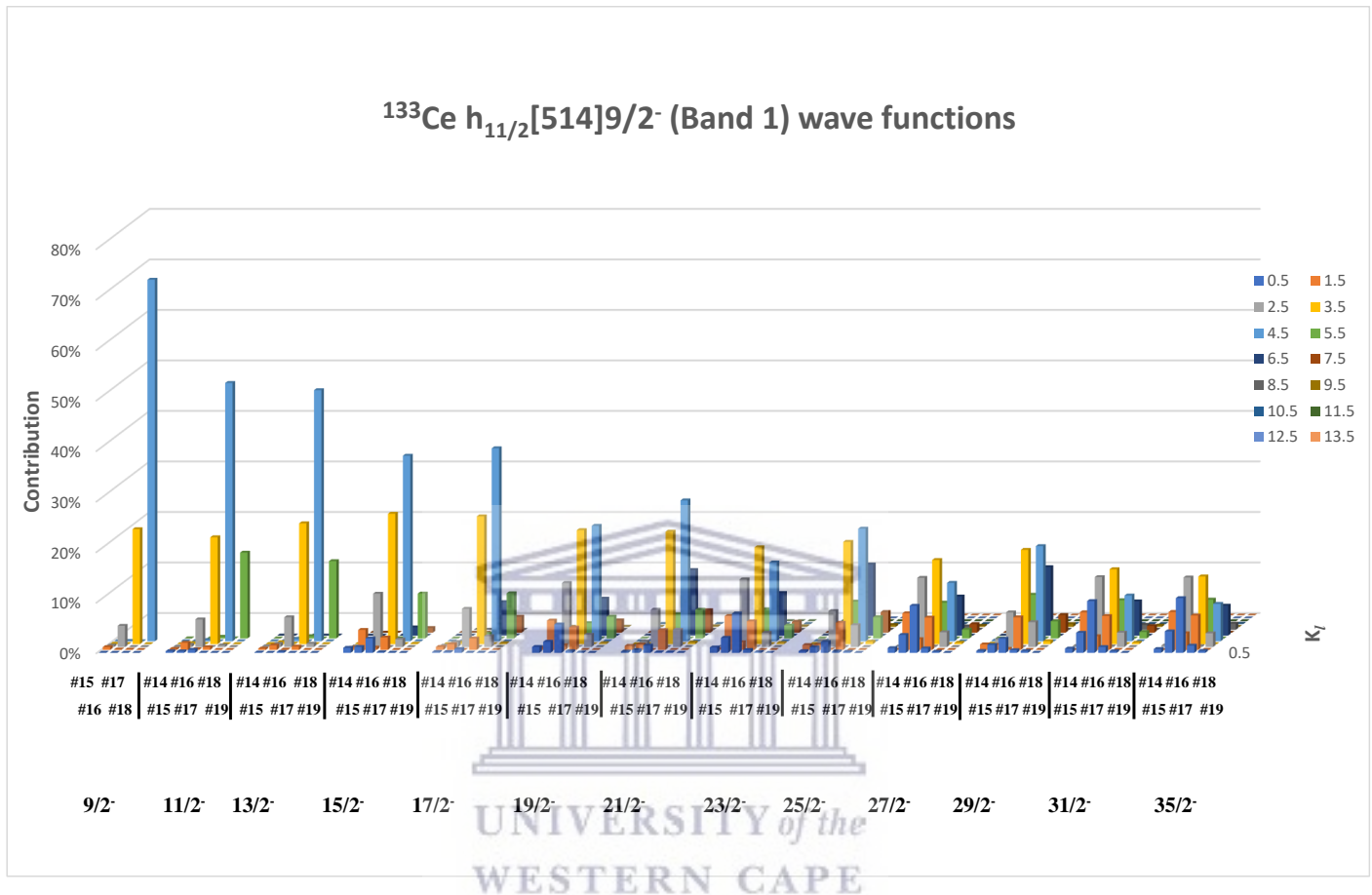
FIGURE 6.12: QTR model wave functions of the states in the yrast band projected onto the long nuclear axis.

At higher spins, for $I > 29/2$, the $(K_l, \Omega_l) = (9/2, 9/2)$ component, while still considerable in the wave functions of the states, becomes less important, while the $(13/2, 9/2)$, $(7/2, 7/2)$, and $(5/2, 5/2)$ components are more significant.

The wave functions of the states in Band 1 do exhibit a staggering pattern. For instance the contribution of the $(9/2, 9/2)$ component shown as a light-blue column in Figure 6.12 is consistently larger for the positive-signature $(\alpha = +1/2)$ states of Band 1. The staggering in the wave functions is probably the cause for the staggering in the excitation energies shown in Figure 6.11 (b).

Wave functions for Band 4

Band 4 is built on the same intrinsic configuration as the yrast band. It is generated by increasing the rotational angular momentum along the intermediate axis, and it also comprises $2\hbar$ of rotation around the long axis. All QTR model states that form Band 4 have $R_l \approx 2\hbar$, consequently, $K_l \approx \Omega_l + 2$; thus at the bandhead of this band, is expected to have dominant components of $(\Omega_l + 2, \Omega_l) = (13/2, 9/2)$; $(11/2, 7/2)$; $(9/2, 5/2)$; $(15/2, 11/2)$ and so forth. Table 6.12 lists the three dominant components of the wave functions for each state in this band.

I^π	contribution in terms of $\lvert \boldsymbol{K_l \nu} \rangle$
$\frac{13}{2}^-$	$0.788 \left\lvert \frac{13}{2} 18 \right\rangle - 0.437 \left\lvert -\frac{11}{2} 17 \right\rangle + 0.262 \left\lvert -\frac{11}{2} 19 \right\rangle$
$\frac{15}{2}^-$	$0.692 \left\lvert \frac{13}{2} 18 \right\rangle - 0.473 \left\lvert -\frac{11}{2} 17 \right\rangle + 0.350 \left\lvert -\frac{15}{2} 19 \right\rangle$
$\frac{17}{2}^-$	$0.632 \left\lvert \frac{13}{2} 18 \right\rangle + 0.505 \left\lvert -\frac{11}{2} 17 \right\rangle - 0.297 \left\lvert -\frac{15}{2} 19 \right\rangle$
$\frac{19}{2}^-$	$0.514 \left\lvert -\frac{11}{2} 17 \right\rangle - 0.509 \left\lvert \frac{13}{2} 18 \right\rangle + 0.326 \left\lvert \frac{9}{2} 16 \right\rangle$
$\frac{21}{2}^-$	$-0.498 \left\lvert -\frac{11}{2} 17 \right\rangle - 0.442 \left\lvert \frac{13}{2} 18 \right\rangle - 0.352 \left\lvert \frac{9}{2} 16 \right\rangle$
$\frac{23}{2}^-$	$0.461 \left\lvert \frac{9}{2} 18 \right\rangle + 0.336 \left\lvert -\frac{11}{2} 19 \right\rangle - 0.331 \left\lvert -\frac{3}{2} 15 \right\rangle$
$\frac{25}{2}^-$	$0.450 \left\lvert -\frac{11}{2} 17 \right\rangle + 0.378 \left\lvert \frac{9}{2} 16 \right\rangle + 0.281 \left\lvert \frac{5}{2} 18 \right\rangle$
$\frac{27}{2}^-$	$-0.439 \left\lvert \frac{9}{2} 18 \right\rangle + 0.339 \left\lvert -\frac{3}{2} 15 \right\rangle - 0.246 \left\lvert \frac{1}{2} 15 \right\rangle$

TABLE 6.8: Main components of the QTR model wave functions for states in Band 4 of ^{133}Ce expanded in a strong coupling basis $\lvert K_l \nu \rangle$.

In a similar fashion to Figure 6.12, Figure 6.13 shows the plot of the wave functions of the states in Band 4. The band head state, $I^\pi = 13/2^-$, consists primarily ($\sim 62\%$) of $(K_l, \Omega_l) = (13/2, 9/2)$ component, (see the tall dark-blue column in Figure 6.13). There is also a presence of the $(11/2, 7/2)$ component which corresponds to the $h_{11/2}$ orbital with single-particle angular momentum projection of $7/2$ on the long axis. This means that this state has the same $\lvert \nu \rangle = \lvert 18 \rangle$ orbital as the band head state of the yrast band ($h_{11/2}$ orbital with single-particle angular momentum projection of $9/2$ on the long axis) and an additional $\sim 2\hbar$ of rotational angular momentum ($K_l = \Omega_l + R_l$). At the band head the dominant component corresponds to $(13/2, 9/2)$, thus $I = K_l$, suggesting that the total angular momentum is aligned along the long axis.
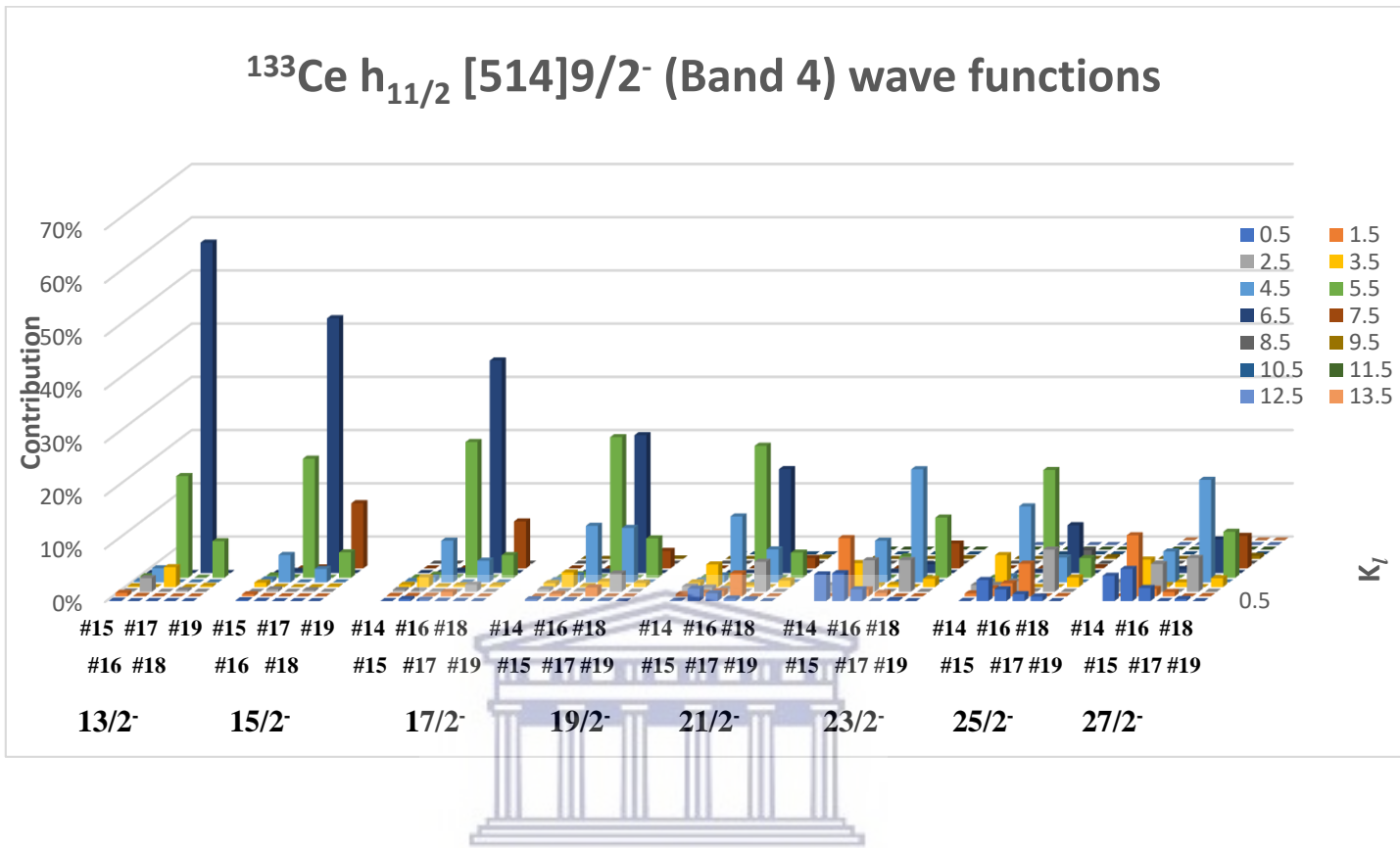
FIGURE 6.13: QTR model wave functions of the states in Band 4 projected onto the long nuclear axis.

The states in Band 4 with $I^\pi = 13/2^-$ to $17/2^-$, have dominant $(13/2, 9/2)$ components in the wave functions, contributing more than 40% to the wave function of each state. However, for these states there is also a significant presence of $(9/2, 9/2)$ and $(11/2, 7/2)$, components. As the spin of the rotational states increases the contribution of $(13/2, 9/2)$ components to the wave function of the states decreases. This correlates with an increase in contribution from components with $(9/2, 9/2)$ and $(11/2, 7/2)$ nature in the wave functions, see Table 6.8. It is also illustrated in Figure 6.13 as an increase in the height of the light-blue, and green columns.

The states with $I^\pi = 19/2^-$ and $21/2^-$ have a greater mixture of $(13/2, 9/2)$, $(9/2, 9/2)$ and $(11/2, 7/2)$ components in the wave functions as the Coriolis interaction causes the single-particle angular momentum, $\vec{j}$, to align with the intermediate axis, and generates components with $\Omega_l = 7/2$. The wave functions of the

higher spin states of $23/2^-$ to $27/2^-$ have greater contributions from $(9/2, 9/2)$ and $(11/2, 7/2)$ components than the lower-spin states. The contribution of $(13/2, 9/2)$ components in the wave functions for the states with $I > 21/2$ is small.

6.3.3 The frozen alignment (FA) approximation for $h_{11/2}$ Bands in ^{133}Ce

In Ref. [23], Frauendorf and Dönau proposed transverse wobbling motion in ^{135}Pr. They approximated the three-dimensional rotational Hamiltonian (simultaneous rotation around the three principle nuclear axes) by $1D$ rotation about the orthogonal (long/short) axis coupled with small-amplitude oscillations of this axis (or coupled with excitations of wobbling phonons). In order for the approximation to be valid it is necessary, (i) that the single-particle angular momentum, $\vec{j}$, is firmly aligned ('frozen') along the orthogonal (long/short) axis. This is needed to exclude the tilting of $\vec{I}$ due to mis-alignment of $\vec{j}$ caused by the Coriolis interaction. Wobbling is a collective mode of excitation, therefore, the single-particle degrees of freedom have to be excluded. However, this is not sufficient to approximate $3D$ rotation with wobbling motion, thus in addition, (ii) the rotation along the wobbling axis should be much larger than the rotation orthogonal to it, i.e. the projection of the rotational angular momentum $\vec{R}$ on the long axis, R_l, should be much larger than the projection of the rotational angular momentum $\vec{R}$ on the intermediate axis, R_i, that is $R_l >> R_i$. This is needed because only if this is true one can approximate the rotation that is orthogonal to the long axis with excitations of wobbling phonons.

The FA approximation is a valid approximation for wobbling motion if the two conditions outlined above are fulfilled. The last condition is not fulfilled in ^{133}Ce, where the rotation along the intermediate axis is dominant. It had already been shown that this condition is in general not fulfilled for one-quasiparticle bands and transverse coupling of the angular momenta [42].

Calculations were performed using the QTR model with the FA approximation as in Ref. [23], where it is assumed that the angular momentum of the odd neutron is firmly aligned with the long axis. This is equivalent to the calculations presented in Section 6.3.2, but with a restricted configurations space, that consists of only one orbital, (orbital $|18\rangle$, listed in Table 6.6). The deformation parameters used in the calculations are presented in Table 6.1. The assumed MoIs are the same as those presented in Section 6.3.2, that is with $\mathcal{J}_0 = 10\ \hbar^2\mathrm{MeV}^{-1}$ and $\mathcal{J}_1 = 25\ \hbar^4\mathrm{MeV}^{-3}$.

The results from the calculations are presented in Figure 6.14. Panel (a) of Figure 6.14 shows the excitation energies as a function of spin. For both, the yrast band (shown in blue), and Band 4 (shown in red) the calculations overestimates the experimental data. This indicates that if one restricts the configuration space, states that would naturally appear at lower energy are excluded from the calculations. Furthermore, contrary to the large energy staggering observed in the experimental data for both bands, the FA approximation produces bands with absent staggering, see panel (b) of Figure 6.14. As we have discussed previously in Section 6.2.1 and Section 6.2.2, bands based on a high-Ω configuration can exhibit signature splitting caused by nuclear triaxiality. Of course if $\vec{j}$ is frozen along the long axis, it cannot re-align. This effectively means that the Coriolis interaction is excluded from the calculations, therefore components other than the $(K_l, \Omega_l) = (9/2, 9/2)$, for the yrast band and $(K_l, \Omega_l) = (13/2, 9/2)$, for Band 4 are left out. Therefore the lack of energy staggering in the calculated bands is a direct consequence of the FA approximation.

In the preceding discussion we have seen the importance of including the single-particle degrees of freedom and allowing $\vec{j}$ to re-align due to the Coriolis interaction, as well as in general allowing contributions from the orbitals near the Fermi surface. It was shown that, while the $(9/2, 9/2)$ component plays a major role for the states of Band 1, other components, such as $(7/2, 7/2)$, $()13/2, 9/2$, $(11/2, 11/2)$ and $(5/2, 5/2)$ also contribute significantly, particularly at high spins where the $(9/2, 9/2)$ component is not dominant, see Figure 6.12.

In Band 4 components other than the $(13/2, 9/2)$ component are favored for some states in the band, in particular the $(9/2, 9/2)$, $(11/2, 7/2)$, and $(15/2, 11/2)$ components are largest for the $I^\pi = 25/2^-$ and $27/2^-$ states as shown in Figure 6.13. These components are important in the construction of the rotational states as they come down in energy and become more favored than the $(13/2, 9/2)$ component.

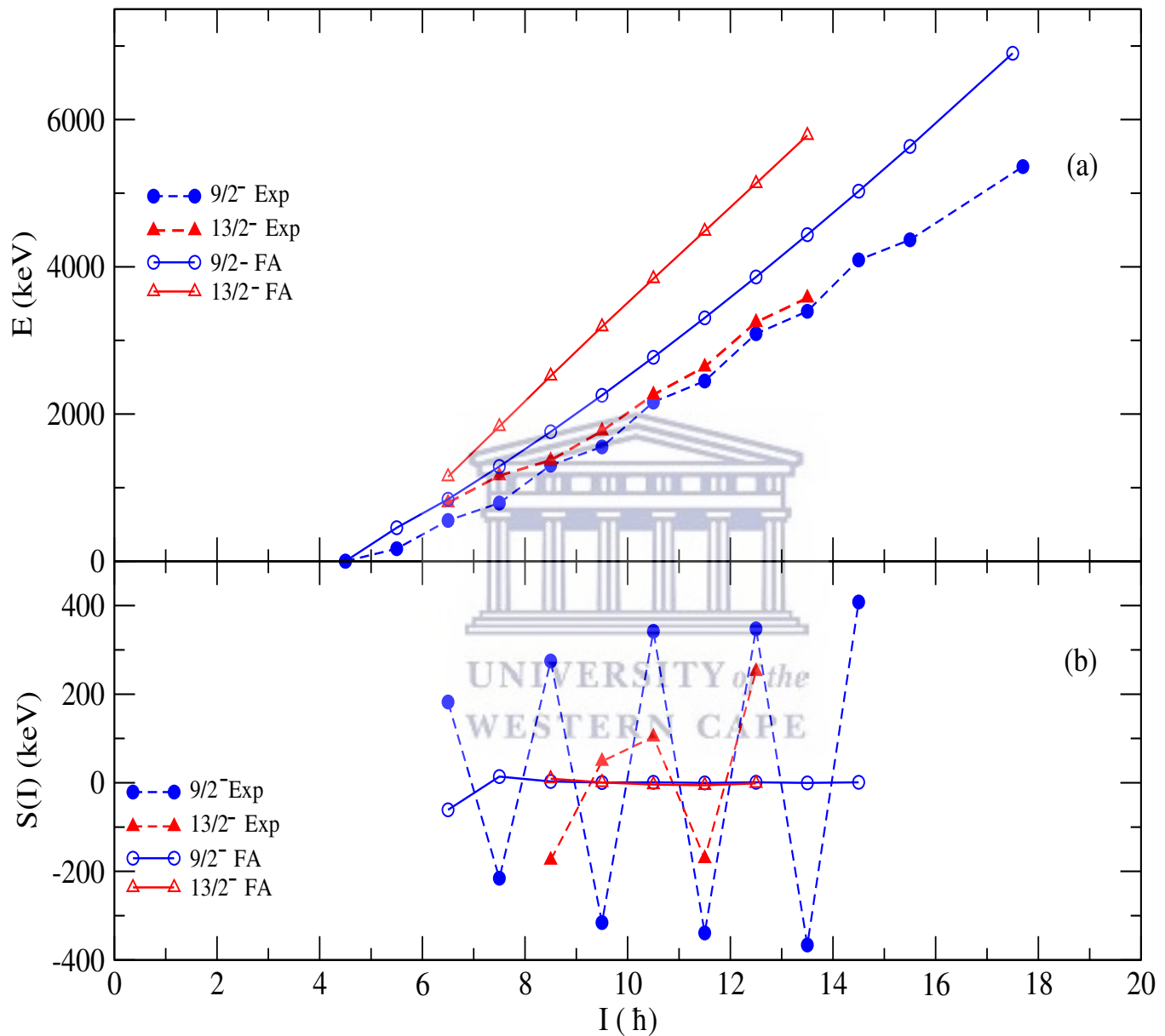FIGURE 6.14: Panel (a) shows a comparison of the excitation energies, ($E(I)$) extracted from the QTR model calculations assuming a frozen alignment (solid lines) with the experimental excitation energies (dashed lines) for Band 1 (shown in blue) and Band 4 (shown in red). The deformation parameters are those listed in Table 6.1. Panel (b) shows the corresponding signature splitting, ($S(I)$ for panel (a).

6.3.4 Electromagnetic Properties

The interpretation of the low-lying rotational structures found in the ^{135}Pr as zero-, one-, and two-phonon transverse wobbling motion as described in Ref. [23], was questioned in Refs. [71, 72].

In Ref. [42] the transverse wobbling motion interpretation for low-lying yrare bands in odd-mass nuclei was examined. It was pointed out that the transverse wobbling Hamiltonian as given in Ref. [23] is not equivalent to the $3D$ quasiparticle-plus-triaxial rotor (QTR) model Hamiltonian. It was shown that the conditions necessary for harmonic frozen alignment (HFA) approximation at low and medium spins are not satisfied for transverse coupling. When the HFA approximation is not valid, the QTR calculations describe three-dimensional rotation tilted precession, TiP bands and not wobbling. This motion looks like precession similar to the precession of a rotating top with respect to the vertical axis.

As we have seen in Section 6.3.3, the frozen alignment (FA) approximation can not reproduce the experimentally observed large magnitude signature splitting in the yrast band of ^{133}Ce. In the following the predicted electromagnetic transition probabilities from the QTR model with FA and QTR model with a large configuration space are compared with the experimentally measured values.

An important feature of all wobbling bands is that two successive bands based on the same one-quasiparticle configuration and differing by one wobbling phonon ($\Delta n = 1$), should be linked with $\Delta I = 1$, M1 + E2 transitions with dominant E2 nature, that is with mixing ratio $|\delta_{E2/M1}| > 1$. Mixing ratios with magnitudes larger than one are associated with collective modes of excitation such as wobbling, TiP, and vibration motion. However, it is possible to measure mixing ratios less than one for TiP, because of the presence of single-particle degrees of freedom, while wobbling requires $|\delta| > 1$ for such M1+E2 transitions. Therefore, measuring mixing ratios with magnitudes larger than one for M1+E2 transitions interconnecting two successive wobbling bands are necessary evidence to support the transverse wobbling interpretation [23].

Recently, the wobbling interpretation of the one- and two-phonon wobbling bands in ^{135}Pr was ruled out by new experimental data [45].

Electromagnetic properties were measured for the 625-, 582-, and 465- keV transitions linking Band 4 to Band 1 in ^{133}Ce. The results from the experiment are

presented in Table 6.11. The measured mixing ratio for the 625 keV transition linking the $13/2^-$ state from Band 4 to the $11/2^-$ state from the yrast band was $|\delta_{E2/M1}| \sim 1.5^{+0.97}_{-5.7}$. The 582 keV transition linking the $17/2^-$ state to the $15/2^-$ state was well resolved in the data and a magnitude of the mixing ratio of $|\delta_{E2/M1}| \sim 0.55^{+0.12}_{-0.25}$ was extracted. A magnitude of the mixing ratio of $|\delta_{E2/M1}| \sim 0.17^{+0.09}_{-0.2}$ was extracted for the 465 keV transition linking the $19/2^-$ state to the $17/2^-$ state. The 582- and the 465- keV transitions have a dominant magnetic character as they have only $\sim 30\%$ and $\sim 3\%$ E2 fraction, respectively, while the mixing ratios for the 625- keV transition was measured with large uncertainty, which does not allow to determine which component (M1 or E2) is larger. Based on the measured mixing ratios the excited band (Band 4) in ^{133}Ce cannot be associated with wobbling.

The calculations carried out with a large configuration space and with FA approximation were both able to reproduce the experimentally measured mixing ratios for both intraband transitions in the yrast band, see Figure 6.15.

I_i^π	I_f^π	δ	$\frac{B(E2)_{out}(I \to I-1)}{B(E2)_{in}(I \to I-2)}$,	$\frac{B(M1)_{out}(I \to I-1)}{B(E2)_{in}(I \to I-2)}$
$13/2^-$	$11/2^-$	0.89	—	—
$17/2^-$	$15/2^-$	-2.24	0.75	0.01
$19/2^-$	$17/2^-$	-2.72	0.32	0.03

TABLE 6.9: QTR model electromagnetic transition properties for Band 4 of ^{133}Ce.

I_i^π	I_f^π	δ	$\frac{B(E2)_{out}(I \to I-1)}{B(E2)_{in}(I \to I-2)}$,	$\frac{B(M1)_{out}(I \to I-1)}{B(E2)_{in}(I \to I-2)}$
$13/2^-$	$11/2^-$	-0.58	—	—
$17/2^-$	$15/2^-$	-0.49	0.44	0.19
$19/2^-$	$17/2^-$	-0.49	0.11	0.062

TABLE 6.10: QTR model electromagnetic transition properties for Band 4 of ^{133}Ce assuming a frozen alignment approximation. The parameter employed are the same as those used for panel (a) of Figure 6.14.

I_i^π	I_f^π	E_γ	δ	$\dfrac{B(E2)_{out}(I\to I-1)}{B(E2)_{out}(I\to I-2)}$,	$\dfrac{B(M1)_{out}(I\to I-1)}{B(E2)_{out}(I\to I-2)}$,	$\dfrac{B(E2)_{out}(I\to I-2)}{B(E2)_{in}(I\to I-2)}$,	$\dfrac{B(M1)_{out}(I\to I-1)}{B(E2)_{in}(I\to I-2)}$
$13/2^-$	$11/2^-$	625	$-1.5^{+0.97}_{-5.7}$	$1.15^{+0.48}_{-0.79}$	$0.14^{+0.21}_{-0.13}$	—	—
$17/2^-$	$15/2^-$	582	$-0.55^{+0.12}_{-0.25}$	$5.06^{+3.45}_{-1.66}$	$3.95^{+0.39}_{-0.81}$	$0.33^{+0.28}_{-0.13}$	$0.25^{+0.03}_{-0.05}$
$19/2^-$	$17/2^-$	465	$-0.17^{+0.09}_{-0.2}$	$1.06^{+3.49}_{-0.82}$	$5.54^{+0.12}_{-0.53}$	$0.09^{+0.34}_{-0.07}$	$0.47^{+0.01}_{-0.04}$

TABLE 6.11: Experimental data on the mixing ratios δ, and the measured reduced transition probabilities for Band 4 of ^{133}Ce.
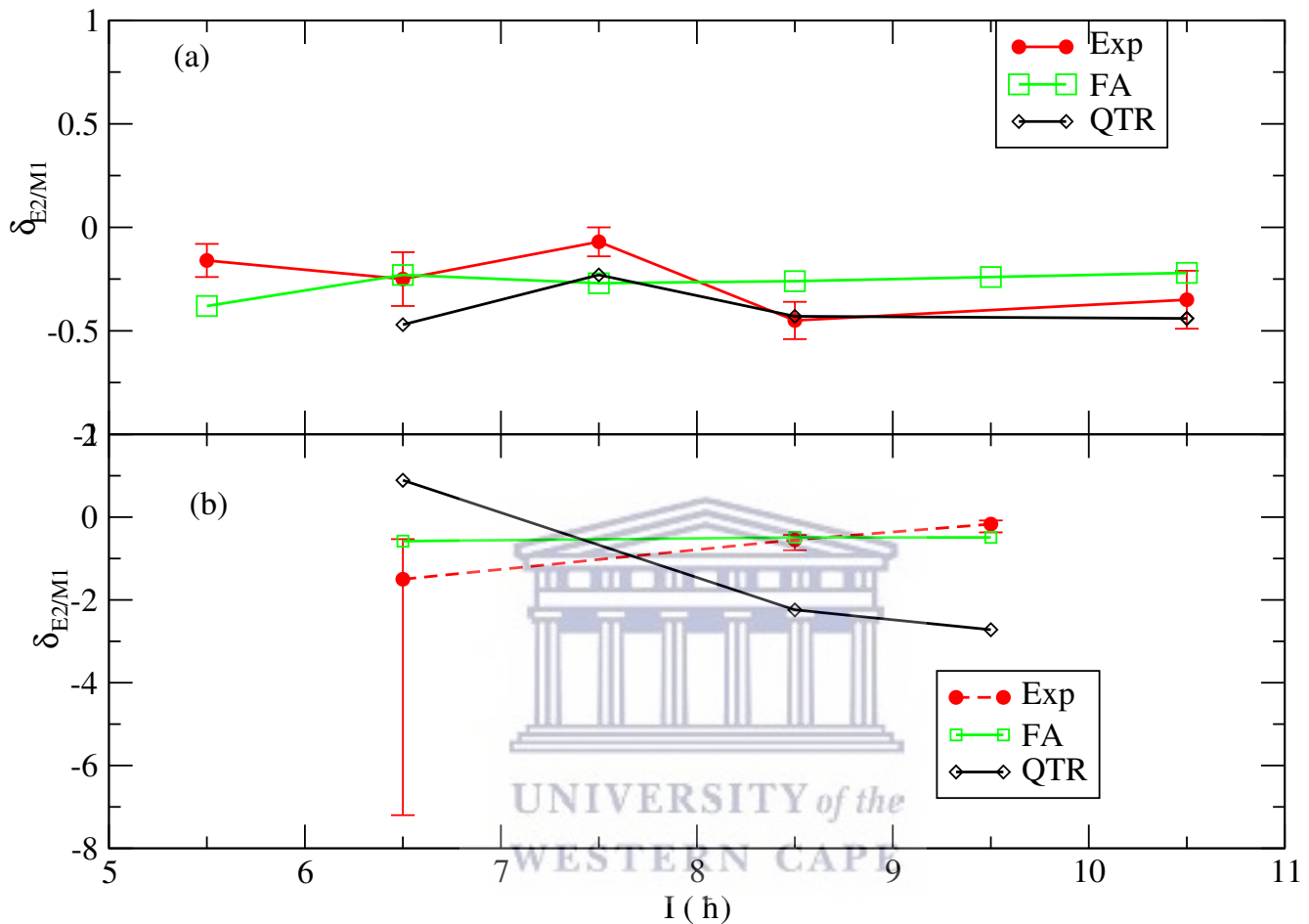
FIGURE 6.15: (a) Mixing ratios $\delta_{E2/M1}$ for intraband transitions for the yrast band. The experimental values are shown in red, green denotes the harmonic frozen approximation, while standard QTR model calculation with full single-particle degrees of freedom are shown in black. Experimental data for the intraband transitions in the yrast band from [56]. (b) Mixing ratios $\delta_{E2/M1}$ for the connecting transitions from Band 4 to the yrast band. Experimental data deduced in this experiment.

The mixing ratios for the connecting transitions from Band 4 to Band 1 are shown in panel (b) of Figure 6.15. It can clearly be seen that the FA approximation (shown in green in panel (b) of Figure 6.15) shows better agreement with the experimentally measured mixing ratios.
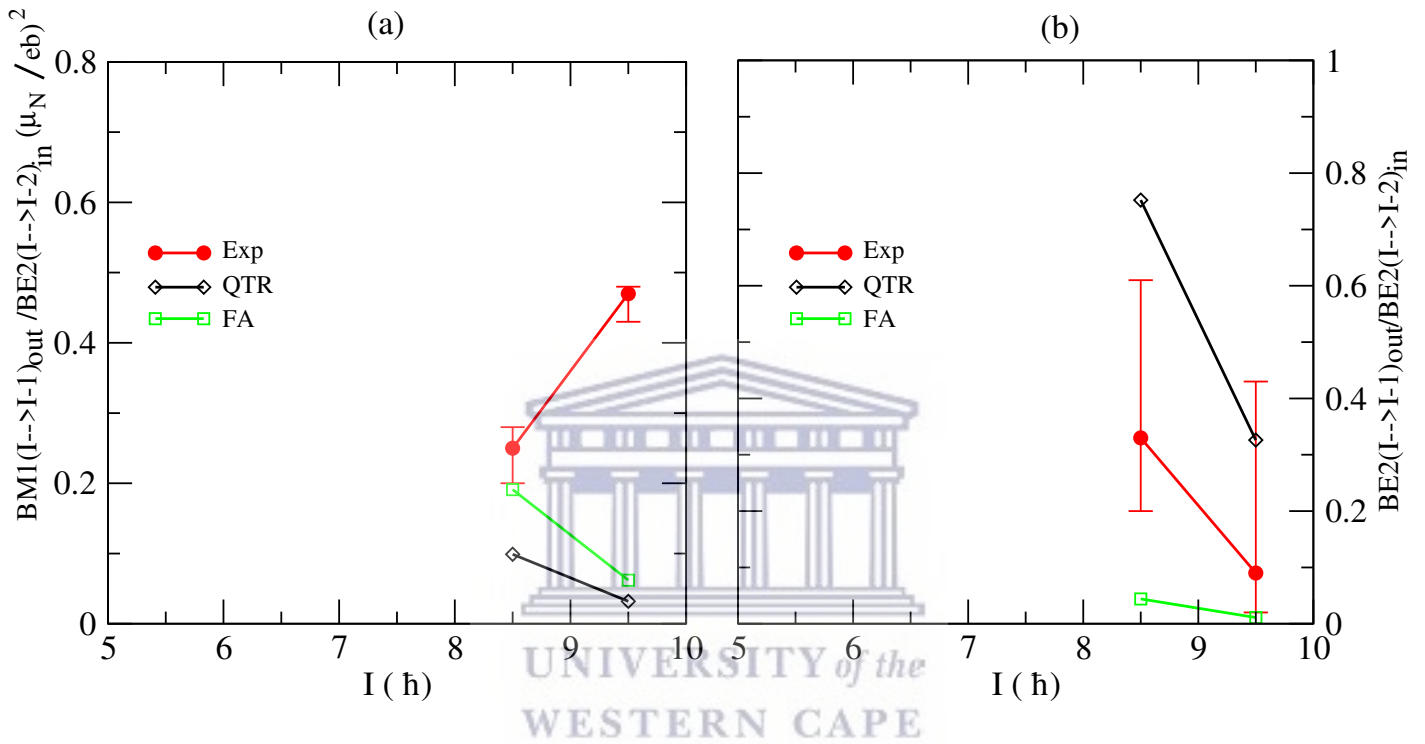
FIGURE 6.16: Electromagnetic ratios for connecting transitions from Band 4 to Band 1. The experimental values are shown in red. Green denotes the frozen approximation. The standard QTR model calculations with full single-particle degrees of freedom are shown in black. Panel (a) shows the $\frac{B(M1)_{out}(I\rightarrow I-1)}{B(E2)_{in}(I\rightarrow I-2)}$ ratios, panel (b) shows the $\frac{B(E2)_{in}(I\rightarrow I-1)}{B(E2)_{out}(I\rightarrow I-2)}$ ratios.

Figure 6.16 (a) shows the $\frac{B(M1)_{out}(I\rightarrow I-1)}{B(E2)_{in}(I\rightarrow I-2)}$ ratios, for the observed connecting transitions listed in Table 6.11. The values obtained from the QTR model with FA approximation and with full consideration of the single-particle degrees of freedom are about the same and show a decreasing trend with increasing spin, while the experimental data indicate an increasing trend with increasing spin. For the $\frac{B(E2)_{out}(I\rightarrow I-1)}{B(E2)_{in}(I\rightarrow I-2)}$ ratios, shown in Figure 6.16 (b) the QTR model calculations with

full single-particle degrees of freedom reproduce the experimental $\frac{B(E2)_{out}(I \to I-1)}{B(E2)_{in}(I \to I-2)}$ ratios better than the FA approximation.

6.3.5   Summary of Part II

The properties of the low lying negative-parity $h_{11/2}$ bands in ^{133}Ce are investigated using the QTR model. In section 6.3.2, the calculations were performed with nine negative-parity orbitals to incorporate the single-particle degrees of freedom. The calculations describe a regular $3D$ precession of the angular momentum vector as described in Refs. [42, 44]. The calculations were able to reproduce the experimentally observed excitation energy and the signature splitting, as measured by the energy staggering index $S(I)$ for Band 1. The $\frac{B(E2)_{out}(I \to I-1)}{B(E2)_{in}(I \to I-2)}$ ratios for the connecting transitions between Band 4 and Band 1 are also well reproduced in the model. The calculations were also able to reproduce the mixing ratios, $\delta_{E2/M1}$, for intraband transitions in Band 1, while the calculated magnitudes of $\delta_{E2/M1}$ for the connecting transitions between Band 4 and Band 1 are a bit high.

QTR model calculations were also performed assuming the angular momentum of the valence neutron is firmly aligned with the long axis (frozen alignment). The model with this assumption was able to reproduce the mixing ratios for both the intraband transitions in Band 1 and the connecting transitions between Band 4 and Band 1. However, the calculations over-estimated the experimental excitation energies and predict an absent signature splitting in both Band 1 and Band 4, contrary to the experimentally observed considerable signature splitting. The predicted $\frac{B(E2)_{out}(I \to I-1)}{B(E2)_{in}(I \to I-2)}$ ratios from the FA approximation are small when compared to experimental data.

Chapter 7

Conclusion

Detailed data sets were collected and analyzed in the $N = 75$ isotones of ^{133}Ce and ^{131}Ba within a collaboration consisting of researchers from South Africa, China and France. The ^{133}Ce experiment was conducted at the separated sector cyclotron of iThemba LABS near Cape Town, South Africa, while the ^{131}Ba experiment was carried out at the XTU Tandem accelerator of Laborotori Nazionali di Legnaro, Italy.

The γ-decay spectroscopy on these experiments revealed a number of new results. One positive-parity band built on the $I^\pi = 7/2^+$ state was discovered in both ^{133}Ce and ^{131}Ba nuclei. As part of this work the γ-γ coincidence from the ^{133}Ce data was studied. The performed γ-coincidence analysis revealed a new strongly coupled positive-parity band in ^{133}Ce, consisting of nine new transitions and four new levels. The analysis of the ^{131}Ba data was carried out by the collaborators. It revealed thirteen new transitions and eight new levels, in a similar strongly coupled positive-parity band built on the $I^\pi = 7/2^+$ state. Both bands show a considerable signature splitting.

The collaborators provided potential energy surface (PES) calculations, which suggested a quadruple deformation of $\varepsilon_2 = 0.185$ and a γ deformation of $\gamma \sim 10°$ for ^{133}Ce and a quadruple deformation of $\varepsilon_2 = 0.170$ and a γ deformation of $\gamma \sim 9°$ for ^{131}Ba. The interpretation of the two bands was carried out as part of this work. It is based on quasiparticle-plus-triaxial rotor (QTR) calculations.

A detailed QTR study of these positive-parity bands was carried out as part of this work. A space of ten QTR model orbitals close to the Fermi level was used

in the calculations. The bands are mainly based on QTR orbital $|\nu\rangle = |20\rangle$, with a projection of 7/2 on the long axis, which corresponds approximately to the $\nu g_{7/2}[404]7/2^+$ Nilsson orbital. The calculations for ^{133}Ce were consistent with a triaxiality of $0° \leq \gamma \leq 15°$, while for ^{131}Ba, a triaxiality of $\gamma \sim 15°$ was required to reproduce the observed excitation energies and energy staggering of the bands. In addition, it was found that the bands in both nuclei are strongly influenced by the Coriolis interaction which causes re-alignment of the angular momentum of the $\nu g_{7/2}$ neutron away from the long axis. Furthermore, the nearby $\nu s_{1/2}$ and $\nu d_{3/2}$ orbitals which have a significant $K = 1/2$ component in their wave functions strongly mix with the dominant $\nu g_{7/2}$ configuration of the band. The theoretical results presented in this work were included in a paper that was just published in Physical Review C [22].

As part of this work, the analysis of the coincidence relationships in the ^{133}Ce data was carried out. It revealed many new transitions that were placed in a new negative-parity band built above the $I^\pi = 13/2^-$ state. Thirteen new intraband and fifteen interband transitions, and eight new levels were discovered. The spin and parity assignments of the new levels and the mixing ratios of the transitions were performed by our Chinese collaborators. The new band decays to a known negative-parity band with $\nu(h_{11/2})^{-1}[514]9/2^-$ configuration. The interpretation of the known yrast band and the new excited negative-parity bands was performed as part of this work. The measured mixing ratios for the transitions of these bands precludes an interpretation of these bands as possible wobbling bands.

Detailed QTR model calculations were carried for these negative-parity bands in ^{133}Ce. Nine QTR orbitals close to the Fermi level with negative-parity were used in the calculations. Six of the orbitals used were from the $h_{11/2}$ sub-shell with projections on the long axis of 1/2 to 11/2. The yrast band is mainly built on the $h_{11/2}$ orbital with a single-particle projection of 9/2 on the long axis. The excited band is built on a state with an extra $2\hbar$ of rotational angular momentum along the long axis than the yrast band. The calculations revealed that in addition to the $h_{11/2}$ orbital with projection of 9/2 on the long axis, the $h_{11/2}$ orbitals with projections of 5/2, 7/2 and 11/2 also play a significant role in the states of both bands. The mixing of these components generates the observed large energy staggering in these bands.

The calculations were also performed with a frozen alignment (FA) approximation, where the angular momentum of the valence nucleon was firmly aligned with

the long axis. This set of calculations failed to describe the the experimentally observed signature splitting and the excitation energies of the states in both the yrast band and the excited band. It was found that when the angular momentum of the valence neutron is firmly aligned along the long axis, components of the wave functions that would otherwise be favorable to construct the rotational states are left out. This resulted in the rotational states predicted from the FA approximation to lie higher in energy than the rotational states calculated with a large configuration space. Furthermore, it was found that the energy staggering is generated by mixing with other orbitals therefore running QTR calculations with FA cannot in principle produce energy staggering.

A manuscript on the new results on the $h_{11/2}$ bands in ^{133}Ce and their interpretation based on the present QTR model calculations is in preparation for submission to Physical Review C.

Bibliography

[1] "APPENDIX NUCLEAR STRUCTURE," http://dbserv.pnpi.spb.ru/elbib/tablisot/toi98/www/struct/struct.pdf, accessed: 2021-09-30.

[2] J. Allmond and J. Wood, "Empirical moments of inertia of axially asymmetric nuclei," *Physics Letters B*, vol. 767, pp. 226–231, 2017. [Online]. Available: https://www.sciencedirect.com/science/article/pii/S0370269317300916

[3] M. Alwaleedi, "Band structures of ^{131}Ce ," Ph.D. dissertation, University of Liverpool, 2013. [Online]. Available: https://livrepository.liverpool.ac.uk/15073/

[4] H. Amro, W. Ma, G. Hagemann, R. Diamond, J. Domscheit, P. Fallon, A. Görgen, B. Herskind, H. Hübel, D. Jensen, Y. Li, A. Macchiavelli, D. Roux, G. Sletten, J. Thompson, D. Ward, I. Wiedenhöver, J. Wilson, and J. Winger, "The wobbling mode in ^{167}Lu," *Physics Letters B*, vol. 553, no. 3, pp. 197–203, 2003. [Online]. Available: https://www.sciencedirect.com/science/article/pii/S0370269302031994

[5] G. Andersson, S. Larsson, G. Leander, P. Möller, S. Nilsson, I. Ragnarsson, S. Åberg, R. Bengtsson, J. Dudek, B. Nerlo-Pomorska, K. Pomorski, and Z. Szymański, "Nuclear shell structure at very high angular momentum," *Nuclear Physics A*, vol. 268, no. 2, pp. 205–256, 1976. [Online]. Available: https://www.sciencedirect.com/science/article/pii/0375947476904619

[6] A. D. Ayangeakaa, U. Garg, M. D. Anthony, S. Frauendorf, J. T. Matta, B. K. Nayak, D. Patel, Q. B. Chen, S. Q. Zhang, P. W. Zhao, B. Qi, J. Meng, R. V. F. Janssens, M. P. Carpenter, C. J. Chiara, F. G. Kondev, T. Lauritsen, D. Seweryniak, S. Zhu, S. S. Ghugre, and R. Palit, "Evidence for Multiple Chiral Doublet Bands in ^{133}Ce," *Physical Review Letters*, vol. 110, p. 172504, Apr 2013. [Online]. Available: https://link.aps.org/doi/10.1103/PhysRevLett.110.172504

[7] A. D. Ayangeakaa, U. Garg, C. M. Petrache, S. Guo, P. W. Zhao, J. T. Matta, B. K. Nayak, D. Patel, R. V. F. Janssens, M. P. Carpenter, C. J. Chiara, F. G. Kondev, T. Lauritsen, D. Seweryniak, S. Zhu, S. S. Ghugre, and R. Palit, "In-beam spectroscopy of medium- and high-spin states in ^{133}Ce," *Physical Review C*, vol. 93, p. 054317, May 2016. [Online]. Available: https://link.aps.org/doi/10.1103/PhysRevC.93.054317

[8] R. Bark, G. Hagemann, B. Herskind, H. Jensen, W. Korten, J. Wrzesinski, H. Carlsson, M. Bergström, A. Brockstedt, A. Nordlund, H. Ryde, P. Bosetti, S. Leoni, F. Ingebretsen, and P. Tjøm, "More than thirty bands in ^{177}Re," *Nuclear Physics A*, vol. 591, no. 2, pp. 265–322, 1995. [Online]. Available: https://www.sciencedirect.com/science/article/pii/0375947495001876

[9] D. Bazzacco, F. Brandolini, G. Falconi, S. Lunardi, N. H. Medina, P. Pavan, C. Rossi Alvarez, G. de Angelis, D. De Acuna, M. De Poli, D. R. Napoli, J. Rico, D. Bucurescu, M. Ionescu-Bujor, and C. A. Ur, "Rotational bands in ^{133}Nd," *Physical Review C*, vol. 58, pp. 2002–2021, Oct 1998. [Online]. Available: https://link.aps.org/doi/10.1103/PhysRevC.58.2002

[10] R. Bengtsson, H. Frisk, F. R. May, and J. A. Pinston, "Signature inversion — a fingerprint of triaxiality," *Nuclear Physics A*, vol. 415, pp. 189–214, 1984. [Online]. Available: https://doi.org/10.1016/0375-9474(84)90620-1

[11] T. Bengtsson and I. Ragnarsson, "Rotational bands and particle-hole excitations at very high spin," *Nuclear Physics A*, vol. 436, no. 1, pp. 14–82, 1985. [Online]. Available: https://www.sciencedirect.com/science/article/pii/037594748590541X

[12] N. Bernier, "Decay spectroscopy of neutron-rich cadmium around the N = 82 shell closure," Ph.D. dissertation, University of British Columbia, 2018. [Online]. Available: https://open.library.ubc.ca/collections/ubctheses/24/items/1.0376019

[13] L. Berti, M. Biasotto, S. Fantinel, A. A. Gozzelino, M. Gulmini, and N. Toniolo, "Lnl infn annual report," *LNL INFN Annual Report*, p. 93, 2014.

[14] S. Biswas, R. Palit, S. Frauendorf, U. Garg, W. Li, G. H. Bhat, J. A. Sheikh, J. Sethi, S. Saha, P. Singh, D. Choudhury, J. Matta, D. Ayangeakaa, W. Dar, V. Singh, and S. Sihotra, "Longitudinal wobbling in ^{133}La," *The European Physical Journal A*, vol. 55, no. 9,

2019. [Online]. Available: https://epja.epj.org/articles/epja/abs/2019/09/10050_2019_Article_12856/10050_2019_Article_12856.html

[15] A. Bohr and B. R. Mottelson, *Nuclear Structure*. World Scientific Publishing Company, 1998. [Online]. Available: https://www.worldscientific.com/doi/abs/10.1142/3530

[16] P. Bringel, G. B. Hagemann, H. Hübel, A. Al-Khatib, P. Bednarczyk, A. Bürger, D. Curien, G. Gangopadhyay, B. Herskind, D. R. Jensen, D. T. Joss, T. Kröll, G. Lo Bianco, S. Lunardi, W. C. Ma, N. Nenoff, A. Neußer-Neffgen, C. M. Petrache, G. Schönwasser, J. Simpson, A. K. Singh, N. Singh, and G. Sletten, "Evidence for wobbling excitation in ^{161}Lu," *The European Physical Journal A*, vol. 24, no. 2, p. 167–172, 2005. [Online]. Available: https://doi.org/10.1140/epja/i2005-10005-7

[17] S. Chakraborty, H. Sharma, S. Tiwary, C. Majumder, A. Gupta, P. Banerjee, S. Ganguly, S. Rai, Pragati, Mayank, S. Kumar, A. Kumar, R. Palit, S. Bhattacharjee, R. Singh, and S. Muralithar, "Multiphonon longitudinal wobbling in ^{127}Xe," *Physics Letters B*, vol. 811, p. 135854, 2020. [Online]. Available: https://www.sciencedirect.com/science/article/pii/S0370269320306572

[18] Q. B. Chen, S. Frauendorf, and C. M. Petrache, "Transverse wobbling in an even-even nucleus," *Physical Review C*, vol. 100, p. 061301, Dec 2019. [Online]. Available: https://link.aps.org/doi/10.1103/PhysRevC.100.061301

[19] R. M. Clark and A. O. Macchiavelli, "The Shears Mechanism in Nuclei," *Annual Review of Nuclear and Particle Science*, vol. 50, no. 1, pp. 1–36, 2000. [Online]. Available: https://doi.org/10.1146/annurev.nucl.50.1.1

[20] A. Davydov and G. Filippov, "Rotational states in even atomic nuclei," *Nuclear Physics*, vol. 8, pp. 237–249, 1958. [Online]. Available: https://www.sciencedirect.com/science/article/pii/0029558258901536

[21] A. Davydov and V. Rostovsky, "Relative transition probabilities between rotational levels of non-axial nuclei," *Nuclear Physics*, vol. 12, no. 1, pp. 58–68, 1959. [Online]. Available: https://www.sciencedirect.com/science/article/pii/0029558259901270

[22] B. Ding, C. M. Petrache, S. Guo, E. A. Lawrie, I. Wakudyanaye, Z. H. Zhang, H. L. Wang, H. Y. Meng, D. Mengoni, Y. H. Qiang, J. G. Wang,

C. Andreoiu, A. Astier, A. Avaa, T. Bäck, R. A. Bark, D. Bazzacco, A. Boso, T. D. Bucher, B. Cederwall, M. V. Chisapi, H. L. Fan, F. Galtarossa, F. H. Garcia, A. Goasduff, G. Jaworski, P. Jones, I. Kuti, J. J. Lawrie, G. S. Li, R. Li, M. L. Liu, Z. Liu, B. Lomberg, B. F. Lv, T. Marchlewski, L. Mdletshe, L. Msebi, S. H. Mthembu, D. R. Napoli, A. Netshiya, M. F. Nkalanga, J. N. Orce, K. Ortner, F. Recchia, S. Riccetto, A. Rohilla, T. W. Seakamela, M. Siciliano, M. A. Sithole, D. Sohler, J. Srebrny, D. Testov, A. Tucholski, J. J. Valiente-Dobón, F. Wentzel, K. Whitmore, Y. H. Zhang, K. K. Zheng, X. H. Zhou, and B. R. Zikhali, "Signature splitting of the $g_{7/2}[404]7/2^+$ bands in ^{131}Ba and ^{133}Ce," *Physical Review C*, vol. 104, p. 064304, Dec 2021. [Online]. Available: https://link.aps.org/doi/10.1103/PhysRevC.104.064304

[23] S. Frauendorf and F. Dönau, "Transverse wobbling: A collective mode in odd-A triaxial nuclei," *Physical Review C*, vol. 89, p. 014322, Jan 2014. [Online]. Available: https://link.aps.org/doi/10.1103/PhysRevC.89.014322

[24] P. E. Garrett and J. L. Wood, "On the robustness of surface vibrational modes: case studies in the Cd region," *Journal of Physics G: Nuclear and Particle Physics*, vol. 37, no. 6, p. 064028, apr 2010. [Online]. Available: https://doi.org/10.1088/0954-3899/37/6/064028

[25] J. Gizon, A. Gizon, and J. Meyer-Ter-Vehn, "Triaxial shape and onset of high-spin bands in ^{129}Ba," *Nuclear Physics A*, vol. 277, no. 3, pp. 464–476, 1977. [Online]. Available: https://www.sciencedirect.com/science/article/pii/037594747790714X

[26] A. Granderath, P. Mantica, R. Bengtsson, R. Wyss, P. von Brentano, A. Gelberg, and F. Seiffert, "Shapes and rotational structures of neutron $h_{11/2}$ configurations in the Xe-Ba-Ce region," *Nuclear Physics A*, vol. 597, no. 3, pp. 427–471, 1996. [Online]. Available: https://www.sciencedirect.com/science/article/pii/037594749500484X

[27] S. Guo, "Comment on "Transverse Wobbling in ^{135}Pr [Phys. Rev. Lett. 114, 082501 (2015)]"," 2021. [Online]. Available: https://arxiv.org/abs/2011.14364

[28] S. Guo, C. Petrache, D. Mengoni, Y. Qiang, Y. Wang, Y. Wang, J. Meng, Y. Wang, S. Zhang, P. Zhao, A. Astier, J. Wang, H. Fan, E. Dupont, B. Lv, D. Bazzacco, A. Boso, A. Goasduff, F. Recchia,

D. Testov, F. Galtarossa, G. Jaworski, D. Napoli, S. Riccetto, M. Siciliano, J. Valiente-Dobon, M. Liu, G. Li, X. Zhou, Y. Zhang, C. Andreoiu, F. Garcia, K. Ortner, K. Whitmore, A. Ataç-Nyberg, T. Bäck, B. Cederwall, E. Lawrie, I. Kuti, D. Sohler, T. Marchlewski, J. Srebrny, and A. Tucholski, "Evidence for pseudospin-chiral quartet bands in the presence of octupole correlations," *Physics Letters B*, vol. 807, p. 135572, 2020. [Online]. Available: https://www.sciencedirect.com/science/article/pii/S0370269320303762

[29] S. Guo, X. H. Zhou, C. M. Petrache, E. A. Lawrie, S. Mthembu, Y. D. Fang, H. Y. Wu, H. L. Wang, H. Y. Meng, G. S. Li, Y. H. Qiang, J. G. Wang, M. L. Liu, Y. Zheng, B. Ding, W. Q. Zhang, A. Rohilla, K. R. Mukhi, Y. Y. Yang, H. J. Ong, J. B. Ma, S. W. Xu, Z. Bai, H. L. Fan, J. F. Huang, J. H. Li, J. H. Xu, B. F. Lv, W. Hua, Z. G. Gan, and Y. H. Zhang, "Probing the nature of the conjectured low-spin wobbling bands in atomic nuclei," 2021. [Online]. Available: https://arxiv.org/abs/2011.14354

[30] S. M. Harris, "Higher Order Corrections to the Cranking Model," *Physical Review*, vol. 138, pp. B509–B513, May 1965. [Online]. Available: https://link.aps.org/doi/10.1103/PhysRev.138.B509

[31] D. J. Hartley, R. V. F. Janssens, L. L. Riedinger, M. A. Riley, A. Aguilar, M. P. Carpenter, C. J. Chiara, P. Chowdhury, I. G. Darby, U. Garg, Q. A. Ijaz, F. G. Kondev, S. Lakshmi, T. Lauritsen, A. Ludington, W. C. Ma, E. A. McCutchan, S. Mukhopadhyay, R. Pifer, E. P. Seyfried, I. Stefanescu, S. K. Tandel, U. Tandel, J. R. Vanhoy, X. Wang, S. Zhu, I. Hamamoto, and S. Frauendorf, "Wobbling mode in ^{167}Ta," *Physical Review C*, vol. 80, p. 041304, Oct 2009. [Online]. Available: https://link.aps.org/doi/10.1103/PhysRevC.80.041304

[32] O. Haxel, J. H. D. Jensen, and H. E. Suess, "On the "Magic Numbers" in Nuclear Structure," *Physical Review*, vol. 75, pp. 1766–1766, Jun 1949. [Online]. Available: https://link.aps.org/doi/10.1103/PhysRev.75.1766.2

[33] S. Ingelman, C. Ekstrom, M. Olsmats, and B. Wannberg, "Nuclear Spins of Neutron-Deficient Lanthanum and Cerium Isotopes," *Physica Scripta*, vol. 7, p. 24, 1973. [Online]. Available: https://iopscience.iop.org/article/10.1088/0031-8949/7/1-2/002

[34] D. R. Jensen, G. B. Hagemann, I. Hamamoto, S. W. Ødegård, B. Herskind, G. Sletten, J. N. Wilson, K. Spohr, H. Hübel, P. Bringel, A. Neußer,

G. Schönwaßer, A. K. Singh, W. C. Ma, H. Amro, A. Bracco, S. Leoni, G. Benzoni, A. Maj, C. M. Petrache, G. L. Bianco, P. Bednarczyk, and D. Curien, "Evidence for Second-Phonon Nuclear Wobbling," *Physical Review Letters*, vol. 89, p. 142503, Sep 2002. [Online]. Available: https://link.aps.org/doi/10.1103/PhysRevLett.89.142503

[35] K. S. Krane, "E2,M1 multipole mixing ratios in even-even nuclei, A $\geq$ 152," *Atomic Data and Nuclear Data Tables*, vol. 16, no. 4, pp. 383–408, 1975. [Online]. Available: https://www.sciencedirect.com/science/article/pii/0092640X75900182

[36] K. S. Krane, *Introductory Nuclear Physics.* New York, NY: Wiley, 1988. [Online]. Available: https://cds.cern.ch/record/359790

[37] A. Krämer-Flecken, T. Morek, R. Lieder, W. Gast, G. Hebbinghaus, H. Jäger, and W. Urban, "Use of DCO ratios for spin determination in γ-γ coincidence measurements," *Nuclear Instruments and Methods in Physics Research Section A: Accelerators, Spectrometers, Detectors and Associated Equipment*, vol. 275, no. 2, pp. 333–339, 1989. [Online]. Available: https://www.sciencedirect.com/science/article/pii/0168900289907067

[38] L. D. Landau and E. M. Lifshitz, *Mechanics, Third Edition: Volume 1 (Course of Theoretical Physics)*, 3rd ed. Butterworth-Heinemann, Jan. 1976. [Online]. Available: http://www.worldcat.org/isbn/0750628960

[39] S. E. Larsson, "The Nuclear Potential-energy Surface with Inclusion of Axial Asymmetry," *Physica Scripta*, vol. 8, no. 1-2, pp. 17–31, jul 1973. [Online]. Available: https://doi.org/10.1088/0031-8949/8/1-2/003

[40] S. Larsson, G. Leander, and I. Ragnarsson, "Nuclear core-quasiparticle coupling," *Nuclear Physics A*, vol. 307, no. 2, pp. 189–223, 1978. [Online]. Available: https://www.sciencedirect.com/science/article/pii/0375947478906139

[41] E. A. Lawrie, J. Lawrie, P. Mutshena, S. Mukherjee, S. Mullins, R. Newman, J. Sharpey-Schafer, and F. Smit, "New Nanosecond Isomers Identified With The AFRODITE Array," private communication.

[42] E. A. Lawrie, O. Shirinda, and C. M. Petrache, "Tilted precession and wobbling in triaxial nuclei," *Physical Review C*, vol. 101, p. 034306, Mar 2020. [Online]. Available: https://link.aps.org/doi/10.1103/PhysRevC.101.034306

[43] J. Ljungvall, M. Palacz, and J. Nyberg, "Monte Carlo simulations of the Neutron Wall detector system," *Nuclear Instruments and Methods in Physics Research Section A: Accelerators, Spectrometers, Detectors and Associated Equipment*, vol. 528, no. 3, pp. 741–762, 2004. [Online]. Available: https://www.sciencedirect.com/science/article/pii/S016890020400988X

[44] B. F. Lv, C. M. Petrache, E. A. Lawrie, A. Astier, E. Dupont, K. K. Zheng, P. Greenlees, H. Badran, T. Calverley, D. M. Cox, T. Grahn, J. Hilton, R. Julin, S. Juutinen, J. Konki, J. Pakarinen, P. Papadakis, J. Partanen, P. Rahkila, P. Ruotsalainen, M. Sandzelius, J. Saren, C. Scholey, J. Sorri, S. Stolze, J. Uusitalo, B. Cederwall, A. Ertoprak, H. Liu, S. Guo, J. G. Wang, H. J. Ong, X. H. Zhou, Z. Y. Sun, I. Kuti, J. Timár, A. Tucholski, J. Srebrny, and C. Andreoiu, "Tilted precession bands in ^{135}Nd," *Physical Review C*, vol. 103, p. 044308, Apr 2021. [Online]. Available: https://link.aps.org/doi/10.1103/PhysRevC.103.044308

[45] B. Lv, C. Petrache, E. Lawrie, S. Guo, A. Astier, K. Zheng, H. Ong, J. Wang, X. Zhou, Z. Sun, P. Greenlees, H. Badran, T. Calverley, D. Cox, T. Grahn, J. Hilton, R. Julin, S. Juutinen, J. Konki, J. Pakarinen, P. Papadakis, J. Partanen, P. Rahkila, P. Ruotsalainen, M. Sandzelius, J. Sarén, C. Scholey, J. Sorri, S. Stolze, J. Uusitalo, B. Cederwall, A. Ertoprak, H. Liu, I. Kuti, J. Timár, A. Tucholski, J. Srebrny, and C. Andreoiu, "Evidence against the wobbling nature of low-spin bands in ^{135}Pr," *Physics Letters B*, vol. 824, p. 136840, 2022. [Online]. Available: https://www.sciencedirect.com/science/article/pii/S0370269321007802

[46] R. Ma, Y. Liang, E. S. Paul, N. Xu, D. B. Fossan, L. Hildingsson, and R. A. Wyss, "Competing proton and neutron rotational alignments: Band structures in ^{131}Ba," *Physical Review C*, vol. 41, pp. 717–729, Feb 1990. [Online]. Available: https://link.aps.org/doi/10.1103/PhysRevC.41.717

[47] R. Ma, E. S. Paul, C. W. Beausang, S. Shi, N. Xu, and D. B. Fossan, "Rotational bands in ^{133}Ce," *Physical Review C*, vol. 36, pp. 2322–2329, Dec 1987. [Online]. Available: https://link.aps.org/doi/10.1103/PhysRevC.36.2322

[48] M. A. J. Mariscotti, G. Scharff-Goldhaber, and B. Buck, "Phenomenological Analysis of Ground-State Bands in Even-Even Nuclei," *Physical Review*, vol.

178, pp. 1864–1886, Feb 1969. [Online]. Available: https://link.aps.org/doi/10.1103/PhysRev.178.1864

[49] J. T. Matta, U. Garg, W. Li, S. Frauendorf, A. D. Ayangeakaa, D. Patel, K. W. Schlax, R. Palit, S. Saha, J. Sethi, T. Trivedi, S. S. Ghugre, R. Raut, A. K. Sinha, R. V. F. Janssens, S. Zhu, M. P. Carpenter, T. Lauritsen, D. Seweryniak, C. J. Chiara, F. G. Kondev, D. J. Hartley, C. M. Petrache, S. Mukhopadhyay, D. V. Lakshmi, M. K. Raju, P. V. Madhusudhana Rao, S. K. Tandel, S. Ray, and F. Dönau, "Transverse Wobbling in ^{135}Pr," *Physical Review Letters*, vol. 114, p. 082501, Feb 2015. [Online]. Available: https://link.aps.org/doi/10.1103/PhysRevLett.114.082501

[50] M. G. Mayer, "On Closed Shells in Nuclei. II," *Physical Review*, vol. 75, pp. 1969–1970, Jun 1949. [Online]. Available: https://link.aps.org/doi/10.1103/PhysRev.75.1969

[51] J. Meyer-Ter-Vehn, "Collective model description of transitional odd-A nuclei: (I). The triaxial-rotor-plus-particle model," *Nuclear Physics A*, vol. 249, no. 1, pp. 111–140, 1975. [Online]. Available: https://www.sciencedirect.com/science/article/pii/0375947475900950

[52] J. Meyer-Ter-Vehn, "Collective model description of transitional odd-A nuclei: (II). Comparison with unique parity states of nuclei in the A = 135 and A = 190 mass regions," *Nuclear Physics A*, vol. 249, no. 1, pp. 141–165, 1975. [Online]. Available: https://www.sciencedirect.com/science/article/pii/0375947475900962

[53] S. Nandi, G. Mukherjee, Q. B. Chen, S. Frauendorf, R. Banik, S. Bhattacharya, S. Dar, S. Bhattacharyya, C. Bhattacharya, S. Chatterjee, S. Das, S. Samanta, R. Raut, S. S. Ghugre, S. Rajbanshi, S. Ali, H. Pai, M. A. Asgar, S. Das Gupta, P. Chowdhury, and A. Goswami, "First Observation of Multiple Transverse Wobbling Bands of Different Kinds in ^{183}Au," *Physical Review Letters*, vol. 125, p. 132501, Sep 2020. [Online]. Available: https://link.aps.org/doi/10.1103/PhysRevLett.125.132501

[54] R. Newman, J. Lawrie, B. Babu, M. Fetea, S. Förstch, S. Naguleswaran, J. Pilcher, D. Raave, C. Rigollet, J. Sharpey-Schafer *et al.*, "Balkan phys. lett.," *Special Issue*, vol. 182, 1998.

[55] S. W. Ødegård, G. B. Hagemann, D. R. Jensen, M. Bergström, B. Herskind, G. Sletten, S. Törmänen, J. N. Wilson, P. O. Tjøm, I. Hamamoto, K. Spohr, H. Hübel, A. Görgen, G. Schönwasser, A. Bracco, S. Leoni, A. Maj, C. M. Petrache, P. Bednarczyk, and D. Curien, "Evidence for the Wobbling Mode in Nuclei," *Physical Review Letters*, vol. 86, pp. 5866–5869, Jun 2001. [Online]. Available: https://link.aps.org/doi/10.1103/PhysRevLett.86.5866

[56] E. S. Paul, R. Ma, C. W. Beausang, S. A. Forbes, D. B. Fossan, J. Gizon, J. R. Hughes, Y. Liang, S. M. Mullins, P. J. Nolan, W. F. Piel, R. J. Poynter, P. H. Regan, R. Wadsworth, and N. Xu, "Electromagnetic properties of N=75 isotones: evidence for triaxiality at low spin," *Journal of Physics G: Nuclear and Particle Physics*, vol. 17, no. 5, pp. 605–617, may 1991. [Online]. Available: https://doi.org/10.1088/0954-3899/17/5/009

[57] C. M. Petrache, Q. B. Chen, S. Guo, A. D. Ayangeakaa, U. Garg, J. T. Matta, B. K. Nayak, D. Patel, J. Meng, M. P. Carpenter, C. J. Chiara, R. V. F. Janssens, F. G. Kondev, T. Lauritsen, D. Seweryniak, S. Zhu, S. S. Ghugre, and R. Palit, "Triaxial-band structures, chirality, and magnetic rotation in ^{133}La," *Physical Review C*, vol. 94, p. 064309, Dec 2016. [Online]. Available: https://link.aps.org/doi/10.1103/PhysRevC.94.064309

[58] C. Petrache, P. Walker, S. Guo, Q. Chen, S. Frauendorf, Y. Liu, R. Wyss, D. Mengoni, Y. Qiang, A. Astier, E. Dupont, R. Li, B. Lv, K. Zheng, D. Bazzacco, A. Boso, A. Goasduff, F. Recchia, D. Testov, F. Galtarossa, G. Jaworski, D. Napoli, S. Riccetto, M. Siciliano, J. Valiente-Dobon, M. Liu, X. Zhou, J. Wang, C. Andreoiu, F. Garcia, K. Ortner, K. Whitmore, T. Bäck, B. Cederwall, E. Lawrie, I. Kuti, D. Sohler, J. Timár, T. Marchlewski, J. Srebrny, and A. Tucholski, "Diversity of shapes and rotations in the γ-soft ^{130}Ba nucleus: First observation of a t-band in the A = 130 mass region," *Physics Letters B*, vol. 795, pp. 241–247, 2019. [Online]. Available: https://www.sciencedirect.com/science/article/pii/S0370269319304228

[59] P. A. Pipidis, "Structural Behavior of ^{157,158,159}Dy in the I= 30- 50L Spin Regime and the High-Spin Domain of ^{158}Er Up to and Above Band Termination." Ph.D. dissertation, Florida State University, 2006. [Online]. Available: https://diginole.lib.fsu.edu/islandora/object/fsu%3A168848

[60] D. Radford, "ESCL8R and LEVIT8R: Software for interactive graphical analysis of HPGe coincidence data sets," *Nuclear Instruments and Methods*

in Physics Research Section A: Accelerators, Spectrometers, Detectors and Associated Equipment, vol. 361, no. 1, pp. 297–305, 1995. [Online]. Available: https://www.sciencedirect.com/science/article/pii/0168900295001832

[61] I. Ragnarsson and S. G. Nilsson, *Shapes and Shells in Nuclear Structure.* Cambridge University Press, 1995. [Online]. Available: https://www.cambridge.org/core/books/shapes-and-shells-in-nuclear-structure/shell-structure-and-magic-numbers/C8382249108DB5290FAE78147CA8F673

[62] I. Ragnarsson and P. B. Semmes, "Description of nuclear moments and nuclear spectra in the particle-rotor model," *Hyperfine Interactions*, vol. 43, no. 1-4, p. 423–440, 1988. [Online]. Available: https://doi.org/10.1007/BF02398323

[63] G. Schönwaßer, H. Hübel, G. Hagemann, P. Bednarczyk, G. Benzoni, A. Bracco, P. Bringel, R. Chapman, D. Curien, J. Domscheit, B. Herskind, D. Jensen, S. Leoni, G. Lo Bianco, W. Ma, A. Maj, A. Neußer, S. Ødegård, C. Petrache, D. Roßbach, H. Ryde, K. Spohr, and A. Singh, "One- and two-phonon wobbling excitations in triaxial ^{165}Lu," *Physics Letters B*, vol. 552, no. 1, pp. 9–16, 2003. [Online]. Available: https://www.sciencedirect.com/science/article/pii/S0370269302030952

[64] N. Sensharma, U. Garg, Q. B. Chen, S. Frauendorf, D. P. Burdette, J. L. Cozzi, K. B. Howard, S. Zhu, M. P. Carpenter, P. Copp, F. G. Kondev, T. Lauritsen, J. Li, D. Seweryniak, J. Wu, A. D. Ayangeakaa, D. J. Hartley, R. V. F. Janssens, A. M. Forney, W. B. Walters, S. S. Ghugre, and R. Palit, "Longitudinal Wobbling Motion in ^{187}Au," *Physical Review Letters*, vol. 124, p. 052501, Feb 2020. [Online]. Available: https://link.aps.org/doi/10.1103/PhysRevLett.124.052501

[65] N. Sensharma, U. Garg, S. Zhu, A. Ayangeakaa, S. Frauendorf, W. Li, G. Bhat, J. Sheikh, M. Carpenter, Q. Chen, J. Cozzi, S. Ghugre, Y. Gupta, D. Hartley, K. Howard, R. Janssens, F. Kondev, T. McMaken, R. Palit, J. Sethi, D. Seweryniak, and R. Singh, "Two-phonon wobbling in ^{135}Pr," *Physics Letters B*, vol. 792, pp. 170–174, 2019. [Online]. Available: https://www.sciencedirect.com/science/article/pii/S0370269319301959

[66] O. Shirinda, "Studying Chirality In $A \sim 100$, 130 And 190 Mass Regions," Ph.D. dissertation, University of the Western Cape, 2006. [Online]. Available: http://etd.uwc.ac.za/xmlui/handle/11394/1792

[67] J. Simpson, "The euroball spectrometer," *Zeitschrift für Physik A Hadrons and Nuclei*, vol. 358, no. 2, pp. 139–143, 1997.

[68] M. A. Sithole, J. F. S. Schafer, S. N. T. Majola, T. D. Bucher, T. R. S. Dinoko, S. S. Ntshangase, E. A. Lawrie, N. A. Khumalo, S. Jongile, L. Mdletshe, R. A. L. Mdletshe, Bark, N. Erasmus, P. Jones, B. V. Kheswa, J. J. Lawrie, L. Makhathini, B. Malatji, K. L.and Maqabuka, S. P. Noncolela, J. Ndayishimye, O. Shirinda, Z. B. R., and P. L. Masiteng, "New collective structures in the ^{163}Yb nucleus," *The European Physical Journal A*, vol. 55, no. 10, 2019. [Online]. Available: https://doi.org/10.1140/epja/i2019-12866-3

[69] G. Suliman, D. Bucurescu, R. Hertenberger, H. F. Wirth, T. Faestermann, R. Krücken, T. Behrens, V. Bildstein, K. Eppinger, C. Hinke, and et al., "Study of the ^{131}Ba nucleus with the (d,t) reaction," *The European Physical Journal A*, vol. 46, no. 2, p. 187–195, 2010. [Online]. Available: https://doi.org/10.1140/epja/i2010-11046-5

[70] Z. Szymanski, *Fast nuclear rotation.* Clarendon Press Oxford [Oxfordshire], 1983.

[71] K. Tanabe and K. Sugawara-Tanabe, "Stability of the wobbling motion in an odd-mass nucleus and the analysis of ^{135}Pr," *Physical Review C*, vol. 95, p. 064315, Jun 2017. [Online]. Available: https://link.aps.org/doi/10.1103/PhysRevC.95.064315

[72] K. Tanabe and K. Sugawara-Tanabe, "Reply to "Comment on 'Stability of the wobbling motion in an odd-mass nucleus and the analysis of ^{135}Pr' "," *Physical Review C*, vol. 97, p. 069802, Jun 2018. [Online]. Available: https://link.aps.org/doi/10.1103/PhysRevC.97.069802

[73] J. Timár, Q. B. Chen, B. Kruzsicz, D. Sohler, I. Kuti, S. Q. Zhang, J. Meng, P. Joshi, R. Wadsworth, K. Starosta, A. Algora, P. Bednarczyk, D. Curien, Z. Dombrádi, G. Duchêne, A. Gizon, J. Gizon, D. G. Jenkins, T. Koike, A. Krasznahorkay, J. Molnár, B. M. Nyakó, E. S. Paul, G. Rainovski, J. N. Scheurer, A. J. Simons, C. Vaman, and

L. Zolnai, "Experimental Evidence for Transverse Wobbling in ^{105}Pd," *Physical Review Letters*, vol. 122, p. 062501, Feb 2019. [Online]. Available: https://link.aps.org/doi/10.1103/PhysRevLett.122.062501

[74] J. L. Wood, A.-M. Oros-Peusquens, R. Zaballa, J. M. Allmond, and W. D. Kulp, "Triaxial rotor model for nuclei with independent inertia and electric quadrupole tensors," *Physical Review C*, vol. 70, p. 024308, Aug 2004. [Online]. Available: https://link.aps.org/doi/10.1103/PhysRevC.70.024308

UNIVERSITY *of the*

WESTERN CAPE